UNFOCUSED MULTIELEMENT AND TAPERED PHASED ARRAY ULTRASOUND TRANSDUCERS FOR HYPERTHERMIA TREATMENT

BY

PAUL JOSEPH BENKESER

B.S., Purdue University, 1981
M.S., University of Illinois, 1983

THESIS

Submitted in partial fulfillment of the requirements
for the degree of Doctor of Philosophy in Electrical Engineering
in the Graduate College of the
University of Illinois at Urbana-Champaign, 1985

Urbana, Illinois

ABSTRACT

Currently used ultrasound clinical hyperthermia systems lack adequate control of the energy deposition used to heat tumors. This thesis discusses the development and testing of two different ultrasound hyperthermia transducers which allow improved control of the energy deposition.

An unfocused multielement transducer was developed to treat superficial tumors. The acoustical power outputs of the elements can be adjusted independently to control the temperature in the tumor and normal tissues. Acoustical power output measurements and temperature data from exposures of tissues in vitro indicated that the transducer is capable of providing intensities seven times greater than those required to produce therapeutic temperatures.

Two ultrasonic tapered phased array transducers were developed to study the feasability of using such transducers to treat deep seated tumors. A tapered phased array transducer consists of a linear phased array employing elements with a tapered thickness. The cylindrical focal region is generated and steered in two dimensions by controlling the phases of the driving signals on each element, and moved in the third dimension by controlling the driving frequency. A theoretical model of the field intensity distribution of a tapered phased array was developed which agreed well with the experimentally obtained data. Acoustical power output measurements indicated that tapered phased arrays are capable of providing the intensities necessary for producing therapeutic temperatures in tumors. However, an

UNIVERSITY OF ILLINOIS AT URBANA-CHAMPAIGN

THE GRADUATE COLLEGE

AUGUST 1985

WE HEREBY RECOMMEND THAT THE THESIS BY

PAUL JOSEPH BENKESER

ENTITLED UNFOCUSED MULTIELEMENT AND TAPERED PHASED ARRAY ULTRASOUND TRANSDUCERS FOR HYPERTHERMIA TREATMENT

BE ACCEPTED IN PARTIAL FULFILLMENT OF THE REQUIREMENTS FOR THE DEGREE OF DOCTOR OF PHILOSOPHY

Leon A. Frizzell
Director of Thesis Research

Head of Department

Committee on Final Examination†

Leon A. Frizzell
Chairman

Richard L Magin

† Required for doctor's degree but not for master's.

O-517

analysis of the intensity gain produced by a tapered phased array indicated that it could severely limit the size of tumors that can be preferentially heated.

ACKNOWLEDGEMENTS

The author is indebted to his advisors, Professors Leon A. Frizzell and Charles A. Cain, for suggesting the research topic and providing encouragement and support during the research. Appreciation is extended to Kenneth Ocheltree for the development of much of the software used in this research and for many helpful suggestions and criticisms. Special thanks are due to Dr. Steven Foster for his assistance with the amplifiers, and to Dr. Steven Goss and Professor Kenneth Holmes for their assistance in making many of the tissue heating measurements. In addition, gratitude is extended to Robert Cicone for many of the illustrations appearing in this manuscript, Bill McNeil for fabricating the transducers, Joseph Cobb and Aaron Field for their help with the hardware design and construction, and Wanda Elliott for help in preparing this manuscript. The biggest thanks of all to my wife Peggy, for her assistance in typing this manuscript and putting up with me during its preparation.

This work was supported in part by URI Therm-X, Inc., and in part by the National Institute of Health under NIH Training Grant CA 09067.

TABLE OF CONTENTS

CHAPTER 1

INTRODUCTION

The practice of using hyperthermia in the treatment of cancer had its origins in the medical practices of Roman physicians, such as Hippocrates, as early as 2000 BC [1]. Interest in hyperthermia was renewed in the late 1800s due to research by W. Busch in 1866 on heat related tumor regressions [1]. But interest in hyperthermia research diminished with the discovery of x-rays and the use of radiotherapy in the treatment of cancer. Within the past decade, however, there has been a renewed interest in hyperthermia based on research indicating that cancer cells are more sensitive to increased temperatures (42 to 45^{o}C) than normal cells. Most data available to date indicate that reduced tumor pH, position in the cell growth cycle, and decreased nutrient supply are among the more important factors in determining the intrinsic sensitivity of tumor cells to hyperthermia [1]. Fortunately, cells that are heat resistant are often the most sensitive to radiation therapy [2]. In fact, the synergistic effect when hyperthermia is used in conjunction with radiation therapy has been well documented and is perhaps the most useful application of hyperthermia [3,4].

Two approaches to clinical hyperthermia have been used: whole-body and localized heating. Whole-body hyperthermia, where the patient's core body temperature is raised to 42^{o}C using water blankets, molten wax or radiated heat, has been used with some success [5,6,7]. Local or regional hyperthermia has the advantage that higher tumor temperatures can be produced without stress to

the patient. Many different modalities, such as microwaves, ultrasound, and radio frequency currents, have been used to produce local hyperthermia. Each of these techniques has different physical constraints that can limit its applicability in producing localized hyperthermia to particular tumor locations. Unfocused high frequency microwaves (100 to 2450 MHz) can treat only superficial tumors to depths of 2 or 3 cm due to high absorption coefficients in the tissue [8]. Focused microwaves at these frequencies can achieve depths of penetration up to 5 or 6 cm. Lower frequency microwaves (10 to 50 MHz) can achieve depths of penetration of approximately 12 cm, but because of the long wavelengths (37 cm to 185 cm), cannot be focused well [8].

Ultrasound, in the 0.3 to 3.0 MHz frequency range, has several properties that favor its use in localized hyperthermia. Due to its short wavelength and favorable absorption characteristics, ultrasonic energy can be focused into a smaller region, and achieve a greater depth of penetration than can electromagnetic energy [9]. As a result of this focusing advantage, it has been stated that ultrasound is currently the modality of choice for creating a uniform and controllable temperature rise in a tumor deep inside the body [10]. In addition, ultrasound has two properties that make its use in producing localized hyperthermia in superficial tumors desirable: (1) since the wavelength is small in the therapeutic frequency range, ultrasound beams from unfocused transducers can be well collimated, allowing localization of the energy deposition; and (2) since the absorption in tissue is approximately proportional to frequency, the depth of penetration can be controlled by

changing the frequency of the ultrasound [11].

The disadvantages of using ultrasound in hyperthermia are primarily related to impedance mismatches that are present at tissue-air or tissue-bone interfaces and the high absorption (approximately 15 times greater than that of soft tissues [12]) of ultrasound in bone. Ultrasound is almost totally reflected at tissue-air interfaces, and can cause local hot spots at tissue-bone interfaces due to both the high longitudinal attenuation and mode conversion from longitudinal to even more highly attenuated shear waves [12].

Single unfocused transducers have been used to heat superficial tumors [13,14,15], but often these transducers are too small to heat the entire tumor volume without moving the transducer. A single transducer with an aperture larger than the surface area of the tumor is often used when the perfusion rate within the tumor is assumed to be less than the surrounding normal tissues. In the normal tissue, the higher perfusion rate is relied upon to limit its temperature to levels below those necessary for damage. However, the perfusion gradient between normal and tumor tissues often is not great enough to heat the tumor selectively. Also, caution must be used with these transducers to avoid heating bone beneath the tumor volume. Since the beam is unfocused, attenuation is the only factor which decreases the intensity behind the tumor; thus, substantial energy may reach underlying bone. This is a common clinical problem that can result in an aborted treatment if the patient experiences excessive pain [13].

There are several ultrasound systems currently being used to

produce deep localized hyperthermia. Several of these employ multiple transducers arranged such that their fields overlap within the tumor volume. A recently developed system uses 30 focused transducers mounted in a hexagonal configuration [16]. The individual transducers, as well as the entire array of transducers, can be positioned mechanically to control the shape and position of the system focal region. Clinical data from the use of this system are limited, since it has only recently been developed, and critical evaluations of its performance are not yet available. Another multiple transducer system, employing six unfocused transducers, has been used in clinical trials [17]. The configuration of the transducers can be manipulated prior to the treatment to adjust the system focal region, but the unit remains fixed in space for the duration of the treatment. The major problem with this system has been the inability to control or modify, during treatment, the deposition of the ultrasonic energy used for heating. This usually results in hot spots developing in the normal tissues surrounding the tumor, producing intolerable pain to the patient and causing the treatment to be terminated prematurely [18]. Both of these multiple transducer systems require large acoustic access windows to treat tumors at appreciable depths, due to the large size of the applicator assembly. A mechanically scanned focused transducer has also been used to produce deep localized ultrasound hyperthermia [10,19]. The focal region is swept in a predetermined scan path, usually around the periphery of the tumor, by moving the transducer. To achieve preferential heating at the tumor with this system, the radiating area of the transducer must be large compared to its

focal region [20]. It should be noted that none of the systems currently used for treating deep-seated tumors is capable of three-dimensional focal region placement without some type of mechanical movement of the transducer. Clearly, it is desirable to have new types of ultrasonic transducers which can more accurately and efficiently heat superficial and deep-seated tumors, while minimizing the heating of surrounding normal tissues.

The goal of this thesis research was to develop two new ultrasound hyperthermia transducers. The first, an unfocused multielement transducer, was designed to treat superficial tumors to a depth of approximately 4 cm. This thesis covers only the design and initial testing of this transducer that were conducted at the Bioacoustics Research Laboratory at the University of Illinois. Additional testing of the field intensity distributions and initial clinical studies were conducted by personnel at URI Therm-X, Inc. The second transducer, an ultrasonic tapered linear phased array, was designed and tested to determine if such a transducer could be used to treat deep-seated tumors.

The organization of the material in this thesis is as follows: In Chapter 2, the design features of the multielement unfocused transducer are discussed; and in Chapter 3, the design of the tapered linear phased array is presented. Chapter 4 covers the experimental techniques used to test each of the transducers. Results and discussion of the testing of the multielement and tapered phased array transducers are presented in Chapters 5 and 6, respectively. Finally, recommendations for future studies are proposed in Chapter 7.

CHAPTER 2

DESIGN OF THE MULTIELEMENT TRANSDUCERS

2.1 Principles of Operation

A multielement transducer consisting of many unfocused elements, whose acoustical power outputs can be controlled independently, allows for an adaptive approach to the heating of superficial tumors. If the extent of the effective aperture of the transducer is made large enough to cover the surface area of the largest superficial tumor to be treated, then movement of the transducer would not be required to heat the entire tumor volume. Tumors of lesser areas would be heated, without excess heating of the surrounding normal tissue, by controlling the acoustical power output of the individual elements of the transducer to confine the ultrasonic field to the tumor volume. The complete hyperthermia system would involve measurement of the temperature in normal and in tumor tissue, with thermocouples, and control of the average power emitted by each element in order to maintain the desired temperature. Should the temperature of a particular region in the treatment field become excessive, the acoustic power of the element(s) supplying energy to that region would be reduced. This would make it possible to maintain the normal and the tumor tissue temperatures in the treatment field at the desired levels.

2.2 Design Considerations

One of the most important design considerations for the multielement transducer was the choice of the operating frequency. Since the attenuation coefficient of ultrasound increases approximately linearly with frequency, a compromise must be

reached between depth of penetration of the ultrasound and the rate of heat generation. The intensity of an ultrasonic plane wave propagating in the positive z direction is given by

$$I(z) = I_o e^{-2Az} \tag{2.1}$$

where I(z) is the intensity at a distance z in the tissue, I_o is the intensity at the surface of the tissue, and A is the wave amplitude attenuation coefficient of the tissue. The attenuation coefficient A includes the effects on the wave of absorption, scattering, diffraction, refraction, and reflection. For the purposes of this discussion, the absorption coefficient, α, and A will be considered equivalent.

The absorbed power per unit volume at a depth z in the tissue may be expressed as

$$P = \frac{\partial I}{\partial z} = 2\alpha I_o e^{-2\alpha z} \tag{2.2}$$

It is evident from Eq. (2.2) that α affects the power deposition in two ways. Increasing α will increase the absorbed power at shallow depths, but will decrease the amount of power available at the site to be heated [9]. Figure 2.1 shows the intensity versus depth for an attenuation coefficient typical of soft tissues (A = 0.1 Np/cm/MHz) at several frequencies [21]. It is clear that as frequency increases, the depth of penetration decreases since the attenuation is approximately linearly dependent on frequency. Figure 2.2 illustrates the behavior of the power loss versus depth in soft tissue for the frequencies of Fig. 2.1. It is clear that the choice of operating frequency determines the depth at which the tumor can be treated. The most commonly used frequencies for

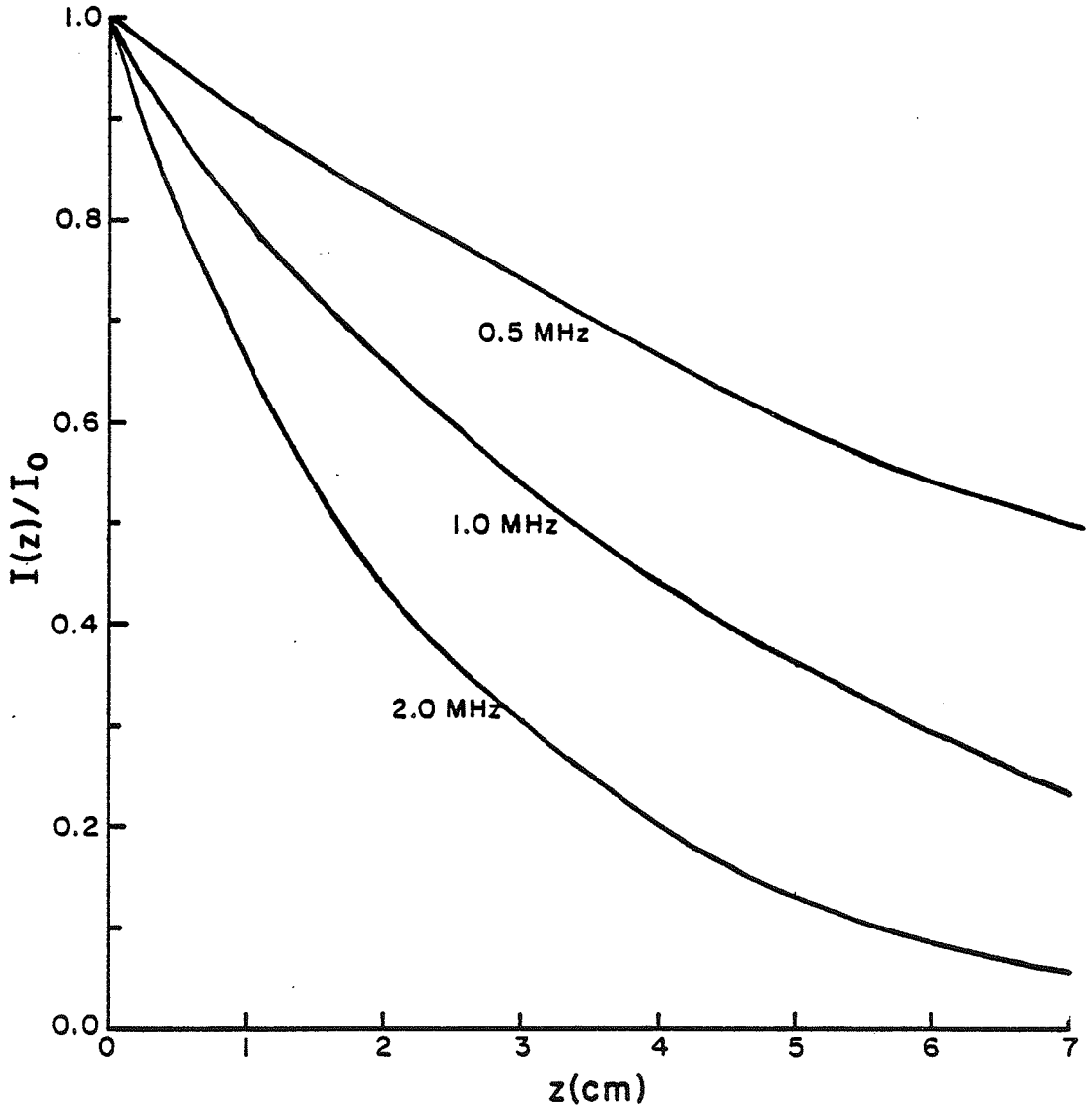

Figure 2.1. Attenuation of ultrasound in soft tissue (A = 0.1 Np/cm/MHz).

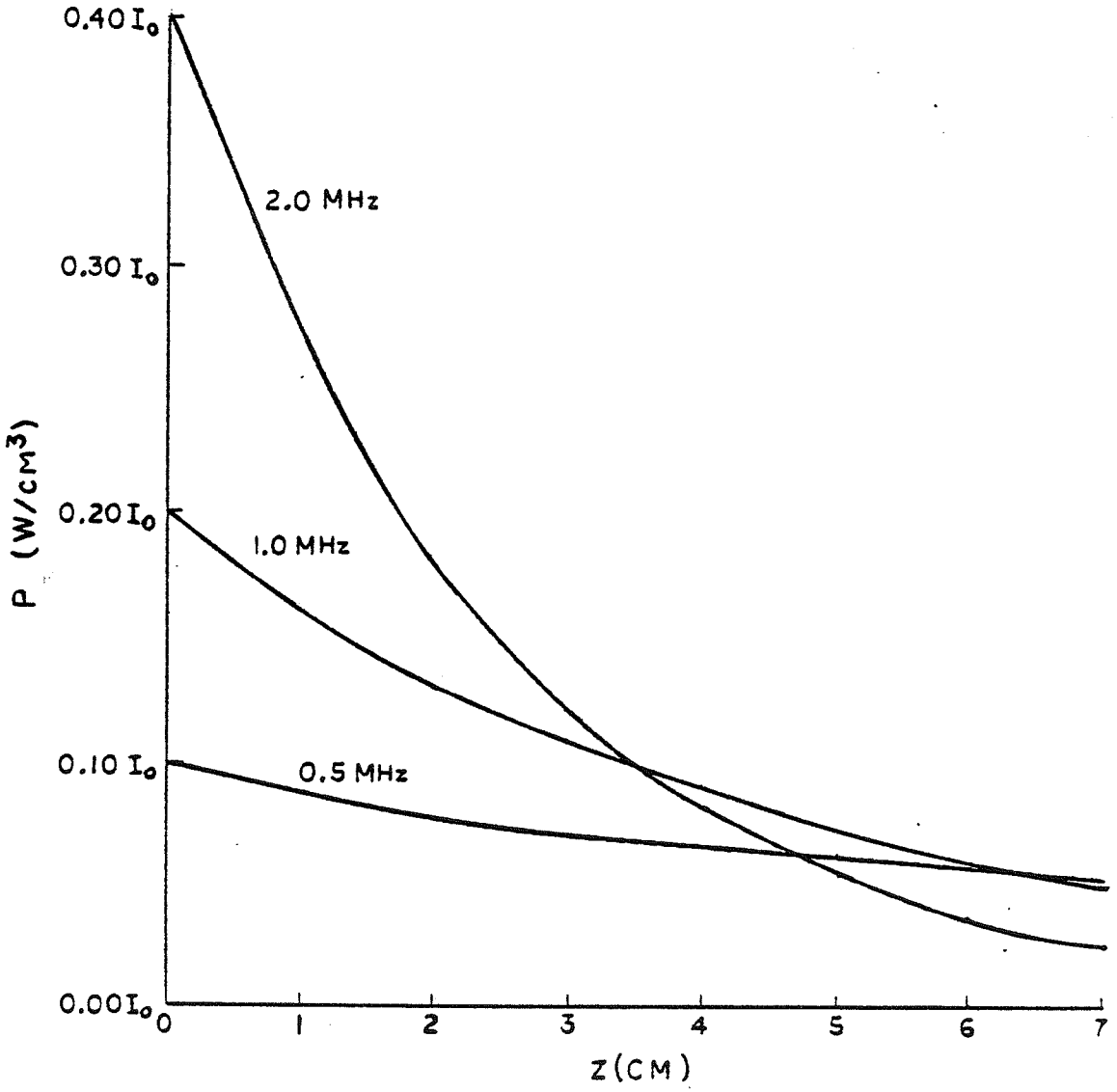

Figure 2.2. Absorbed power per unit volume in soft tissue (α = 0.1 Np/cm/MHz).

treating superficial tumors are between 1 and 3 MHz [13]. At 1 MHz, approximately 50% of the initial power will remain in the ultrasound wave at a depth of 3.5 cm in soft tissue (A = 0.1 Np/cm). Studies of unfocused ultrasound indicated that tumors at depths of approximately 4 cm can be heated to 43°C with frequencies of 0.9 to 1 MHz [13,19]. The use of surface cooling would allow greater power levels to be used to heat tumors at the 4 cm depth without excessive heating of the skin. Therefore, to treat tumors to a depth of at least 4 cm, an operating frequency of 1 MHz was chosen.

For this initial design, the overall aperture of the transducer was chosen to be 15.2 cm by 15.2 cm. Because the wavelength at 1 MHz is small, approximately 1.5 mm in tissue, ultrasound waves from unfocused transducers are well collimated in the near-field, such that tumors approximately 15 cm in diameter could be treated with this transducer. However, this was an initial study of the concept, so the particular size of the transducer was not as important as the approaches taken to design and construct the prototype.

The multielement transducer design consisted of a square array of sixteen 3.8 cm x 3.8 cm square elements. The square array configuration was chosen to provide uniform heating control in both the x and y dimensions. The size of the individual elements had to be large enough so that their fields would be collimated at the maximum distance from the element to the back of the tumor. This required that the near-fields of the elements be used. Considering a coupling bolus filled with degassed water (see Section 4.4) approximately 6 cm in depth, and a maximum tumor

depth of 4 cm, the minimum length of the near-field must be 10 cm. The minimum width of the elements is approximately expressed as

$$d \geq (4\lambda L_{nf})^{1/2} \tag{2.3}$$

where L_{nf} is the required length of the near-field and λ is the wavelength. Therefore, using Eq. (2.3), the minimum width is approximately 2.5 cm. Thus, for the square array configuration, the maximum number of elements over a 231 cm^2 aperture would be 25 (5 by 5 matrix). The 16 element configuration was chosen since it could be easily fabricated using four 7.6 cm x 7.6 cm ceramic plates.

2.3 Fabrication

Three different transducers were fabricated using different techniques. The first multielement transducer constructed, MET1, consisted of four adjacently mounted Channel 5800 piezoelectric ceramics, each 7.6 cm x 7.6 cm with a 1 MHz resonant thickness 0.2 cm. These units were chosen for their excellent high drive characteristics (low dielectric and elastic losses) [22]. Four elements were defined on each of the four plates by scribing the fired-on silver electrode plating on the electrically positive (back) surface of the plate to form four equal, square electrodes. Since the surface area of each element was large compared to its thickness, the excited region of the ceramic was expected to be approximately equal to the area of the element [23]. The four ceramic plates were mounted in a 17 cm x 17 cm x 12 cm watertight anodized aluminum housing on a Plexiglas rear support frame which

maintained the air backing for the transducer elements (see Fig. 2.3). The plates were seated in the frame such that a 3.2 mm strip of Plexiglas separated the four plates. The anodized aluminum front face frame was used to secure and provide ground contacts for the ceramic plates.

Initially, the positive electrode leads were attached to the elements with a conducting epoxy. However, each of these connections failed when passing currents of approximately 3.5 amps. When the resistance of the conducting epoxy connections was measured, it was found to be approximately 0.5 ohms. The power dissipated in the connection when 3.5 amps passed through it was over 6 W. Thus, the failures were most likely caused by the excess heating of the epoxy due to the 6 W power dissipation. Berillium-copper spring contact leads, with only a 0.11 ohm contact resistance, were fabricated and used in place of the epoxy. The new contacts were tested with currents exceeding 4.5 amps without failure, and have maintained good electrical contact over a period of several months of use. These contacts have been used on all the multielement transducers including the other designs discussed below.

This design, MET1, produced a field intensity distribution which was severely affected by the plate separation and the front face frame (see Section 5.1). In a second design, MET2, the Plexiglas rear support frame was replaced with a brass frame that reduced the spacing between the plates to 0.79 mm. The front face frame was removed and the plates were secured in the rear support frame with conducting epoxy around the front edges of the plates which also served as the ground connection. This modified design,

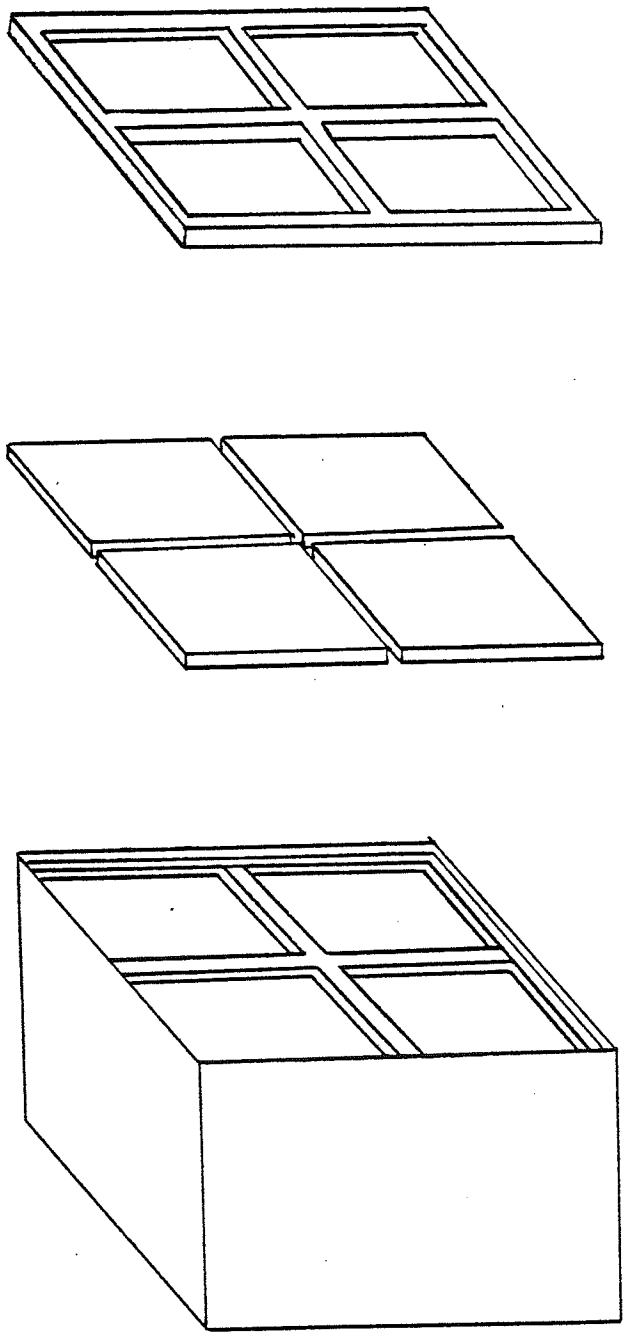

Figure 2.3. Exploded view of METl.

though much improved, still suffered from effects associated with the rear support frame along the edges of adjoining plates (see Section 5.1).

A third and final design, MET3, used only a single 15.2 cm x 15.2 cm x 0.2 cm Channel 5800 ceramic plate, as shown in Fig. 2.4, instead of four 7.6 cm x 7.6 cm plates. To eliminate any damping effects, the crossbars of the rear support frame were removed. The ground connection on the front side of the ceramic plate was made to the frame with conducting epoxy around its perimeter. Since the ground connection was made around the entire periphery of the plate, the resulting current density was low enough to avoid the problem experienced with the epoxy on the positive lead connection. Also, the size of the housing for MET3 was reduced to 17 cm x 17 cm x 10 cm to make it less bulky, yet still large enough to hold 16 electrical impedance matching networks (see Section 2.5).

2.4 Power Dissipation in the Transducer

A major concern in the design of a high-power ultrasound transducer is its power handling capability. The manufacturer's specifications of Channel 5800 ceramic, larger than several wavelengths in width, indicate that it has a typical electroacoustic efficiency of 90% at 20°C. This means that 10% of the applied power will be dissipated in the ceramic so long as it remains at 20°C. The power dissipation is due primarily to internal dielectric and mechanical losses which convert electrical and mechanical energy to heat. The temperature rise resulting from these losses can cause a reduction in the efficiency of the

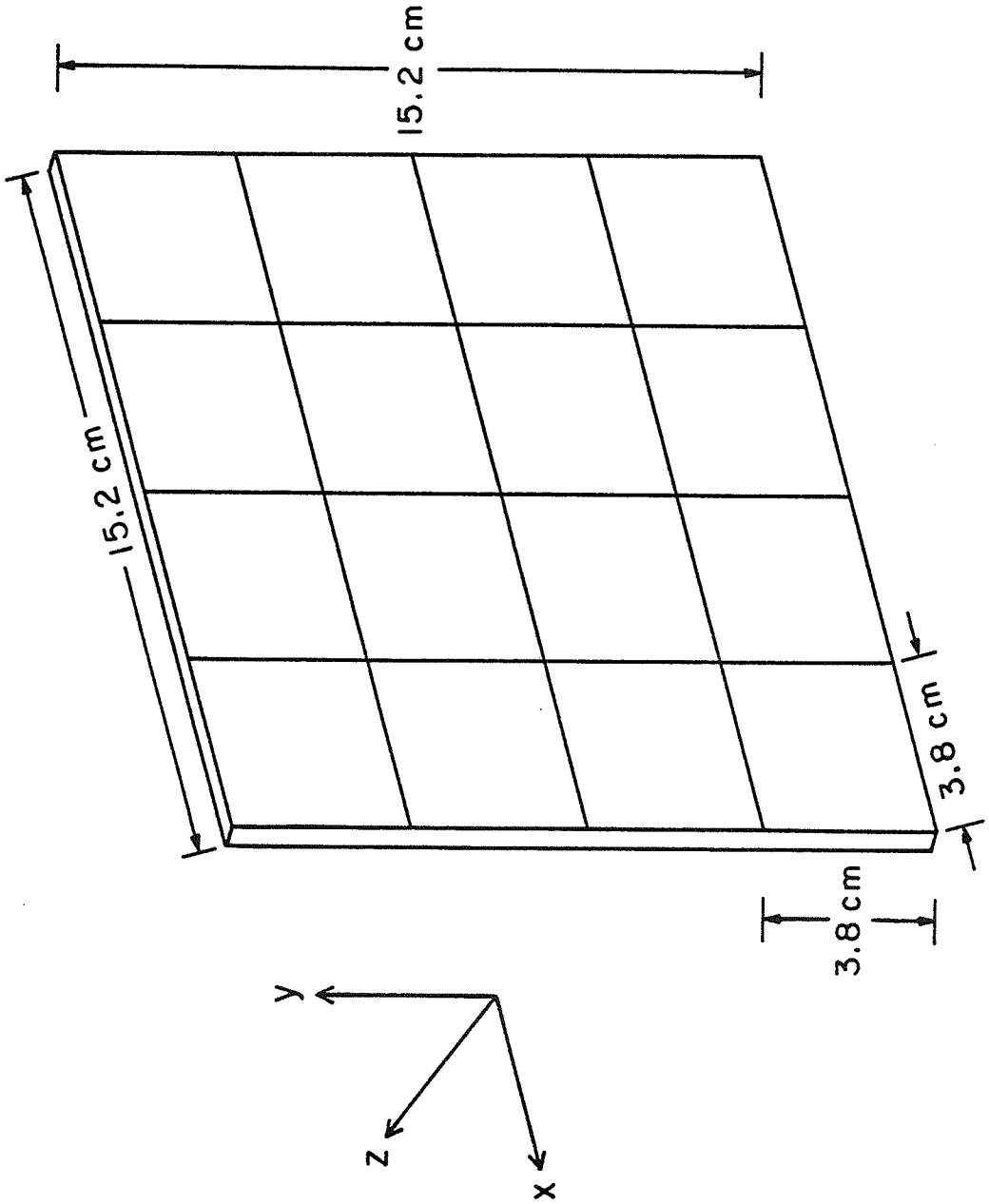

Figure 2.4. Element configuration on the back surface of the piezoelectric ceramic of MET3.

ceramic. Both dielectric and mechanical losses are proportional to frequency and, therefore, high frequency cw transducers are likely to have their outputs limited by temperature rise [24]. Should the temperature reach the Curie temperature of the ceramic (approximately 300°C for Channel 5800), the ceramic will be depolarized. However, lower temperatures will have an effect on the efficiency of the ceramic through a change in the mechanical quality factor, Q_m. The typical change in Q_m, with temperature for PZT-8 ceramic material (similar to Channel 5800), is shown in Fig. 2.5. It is clear that Q_m is very temperature dependent. In general, dielectric losses are the limiting factor in low Q transducers, while mechanical losses are the limiting factor in high Q transducers [22].

To predict theoretically the steady state temperature in the ceramic, the large slab model used in heat transfer studies was employed [25]. In this model, the slab (ceramic) is bounded by water on one side and air on the other side (see Fig. 2.6). Compared to the water boundary, the air boundary can be considered to be a perfect insulator since it will conduct only approximately 1% of the amount of heat conducted by the water. The heat conduction equation for this case is

$$\frac{d^2T(x)}{dx^2} = -\frac{W}{k} \quad \text{for } 0 \leq x \leq L \tag{2.4}$$

where T(x) is the temperature in the ceramic, W is the power dissipated in the ceramic per unit time per unit volume, and k is the thermal conductivity of the ceramic plate (approximately 2.1 W/m°C). The boundary conditions for the ceramic plate are

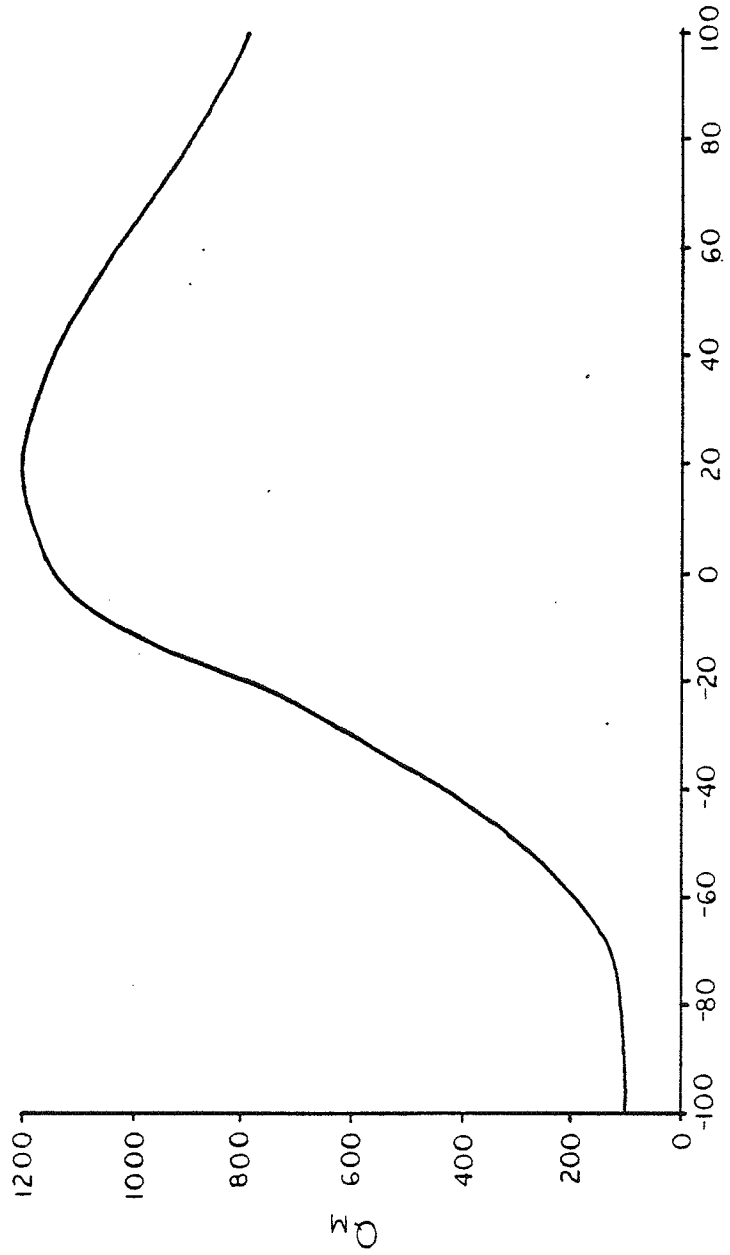

Figure 2.5. The effect of temperature on the mechanical quality factor, Q_m for PZT-8 [22].

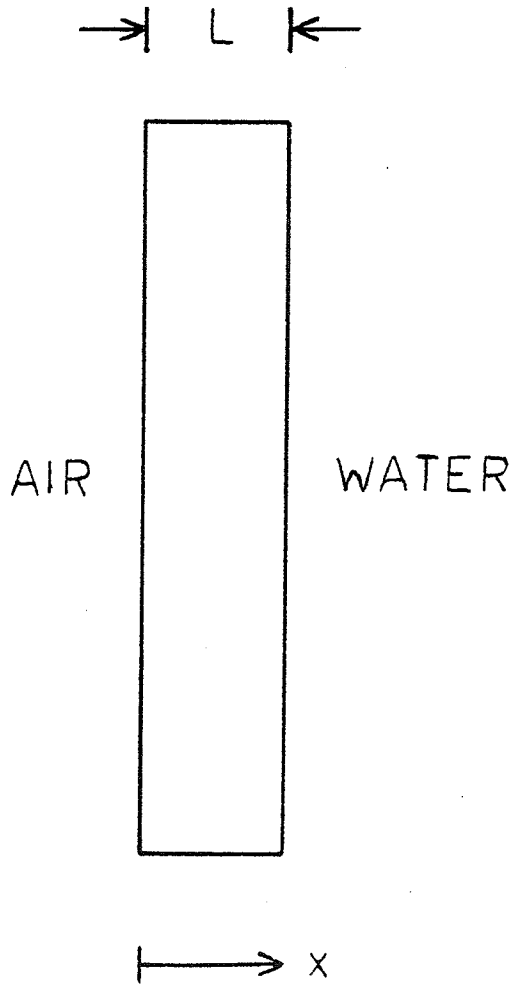

Figure 2.6. Large slab model used to calculate the temperature distribution in the ceramic.

$$\left.\frac{dT(x)}{dx}\right|_{x=0} = 0 \tag{2.5}$$

and

$$\left.-k\,\frac{dT(x)}{dx}\right|_{x=L} = \left.h(T(x) - T_{\infty})^{1.25}\right|_{x=L} \tag{2.6}$$

where $h(T(x) - T_{\infty})^{1.25}$ is the rate of heat loss to the water due to natural convection, h is the coefficient of heat loss, and T_{∞} is the temperature of the water far from the ceramic. Natural convection occurs when a hot surface is in contact with a fluid, and the warmer fluid next to the surface tends to rise, setting up convection currents. The value for h can be determined only experimentally. For water in contact with surfaces a few centimeters or more in width, h has been determined experimentally to be approximately 0.005 cal/cm^2/s [26]. Solving Eq. (2.4) using the boundary conditions, the temperature in the ceramic, T(x), is

$$T(x) = \frac{W}{2k}(L^2 - x^2) + \left(\frac{WL}{h}\right)^{0.8} \tag{2.7}$$

It is important to note that this is only an approximate equation and an accurate value of h needs to be determined experimentally.

2.5 Electrical Impedance Matching

In order to maximize the conversion of electrical to acoustic energy, the amplifiers (see Section 4.1) were matched to the 50 ohm coaxial cables used to conduct the energy to the transducer. Additionally, an electrical matching network was mounted inside

the transducer housing to match the coaxial cable and element impedances. Because of the limited space in the housing, the matching network shown in Fig. 2.7 was chosen, as it required the minimum number of components. The value of the inductor was chosen to make the equivalent parallel resistance, R_{pe}, of the impedance Z_s equal to 50 ohms. The required value of the inductor, L, can be determined from the relation

$$R_{pe} = X + \frac{(2\pi fL + Y)^2}{X} \tag{2.8}$$

where X+jY is the element impedance and f is the frequency (in this case 1 MHz). The equivalent parallel inductance, from the addition of L, is balanced by the parallel capacitor, C. The value of C can be determined from

$$C = \frac{1}{2\pi f(\mathrm{Im}\{Z_s^{-1}\})} \tag{2.9}$$

Since the elements had slightly different impedances, each matching network was individually designed for its respective element. At 1 MHz, the average unmatched and matched impedances seen by the amplifier were approximately $11.3\angle -2.8^{\circ}$ ohms and $51.6\angle -2.5^{\circ}$ ohms, respectively.

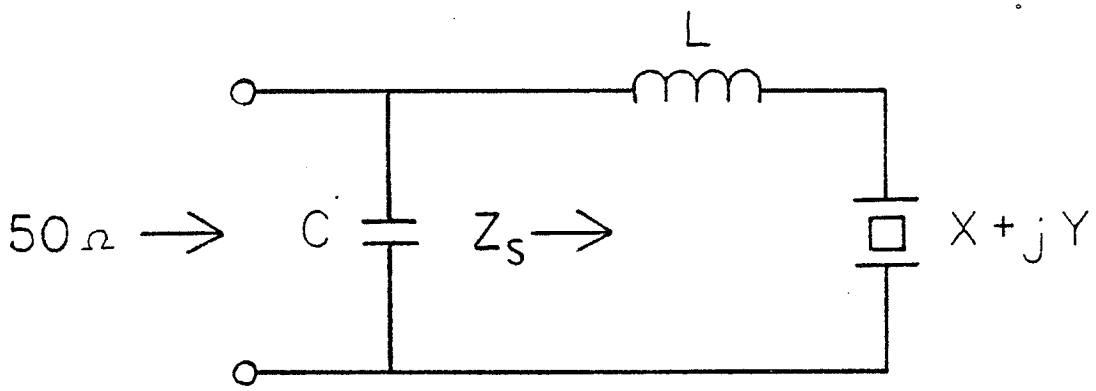

Figure 2.7. Electrical matching network for an element of the multielement transducer.

CHAPTER 3

DESIGN OF THE TAPERED PHASED ARRAY TRANSDUCERS

3.1 Principles of Operation

An alternate approach to mechanical alignment of multiple transducers or mechanical scanning of transducers for treatment of deep-seated tumors is to use an ultrasonic phased array. A phased array, such as that shown in Fig. 3.1, offers the alternative of electronic scanning of a focused beam without movement of the transducer assembly. The focus can be generated and positioned in three dimensions by controlling the phases of the signals driving each array element so that constructive interference of the waves is achieved at the desired field point. By readjusting the phased periodically, the focus can be scanned over any three-dimensional path at a rate much faster than that of a mechanically scanned system [27]. This will produce a temperature at any location which has less variation because of the short time between scans. It also enables the phased array to provide more accurate control of heating in the treatment field since its scan path can be changed quickly to maintain the desired normal and tumor tissue temperatures.

Phased arrays in general, and a two-dimensional array of elements in particular, introduce the complexities of phase control, many amplifiers, and complex fabrication techniques. These complications can be reduced if, instead of a complete two-dimensional array of elements, a one-dimensional phased array composed of elements that have tapered thickness is employed, as illustrated in Fig. 3.2. The region along the length of the

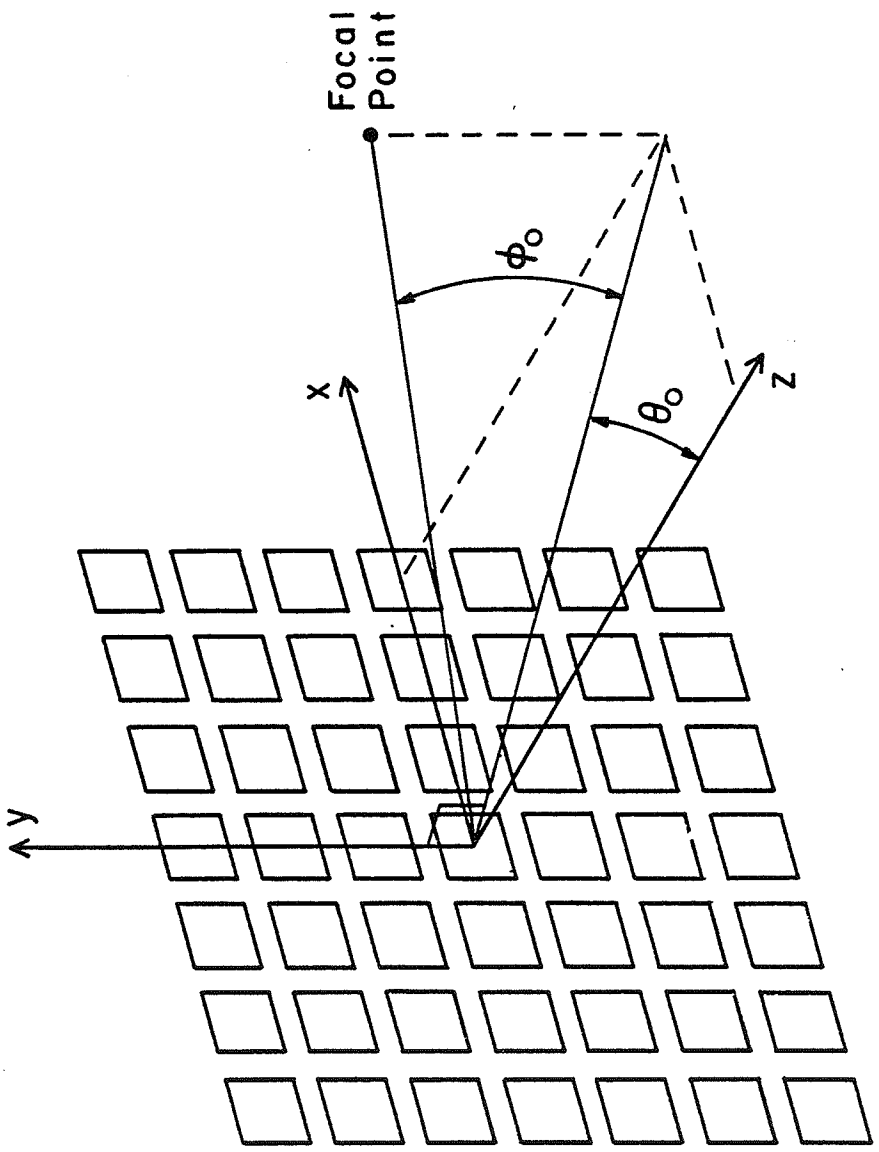

Figure 3.1. Two-dimensional phased array.

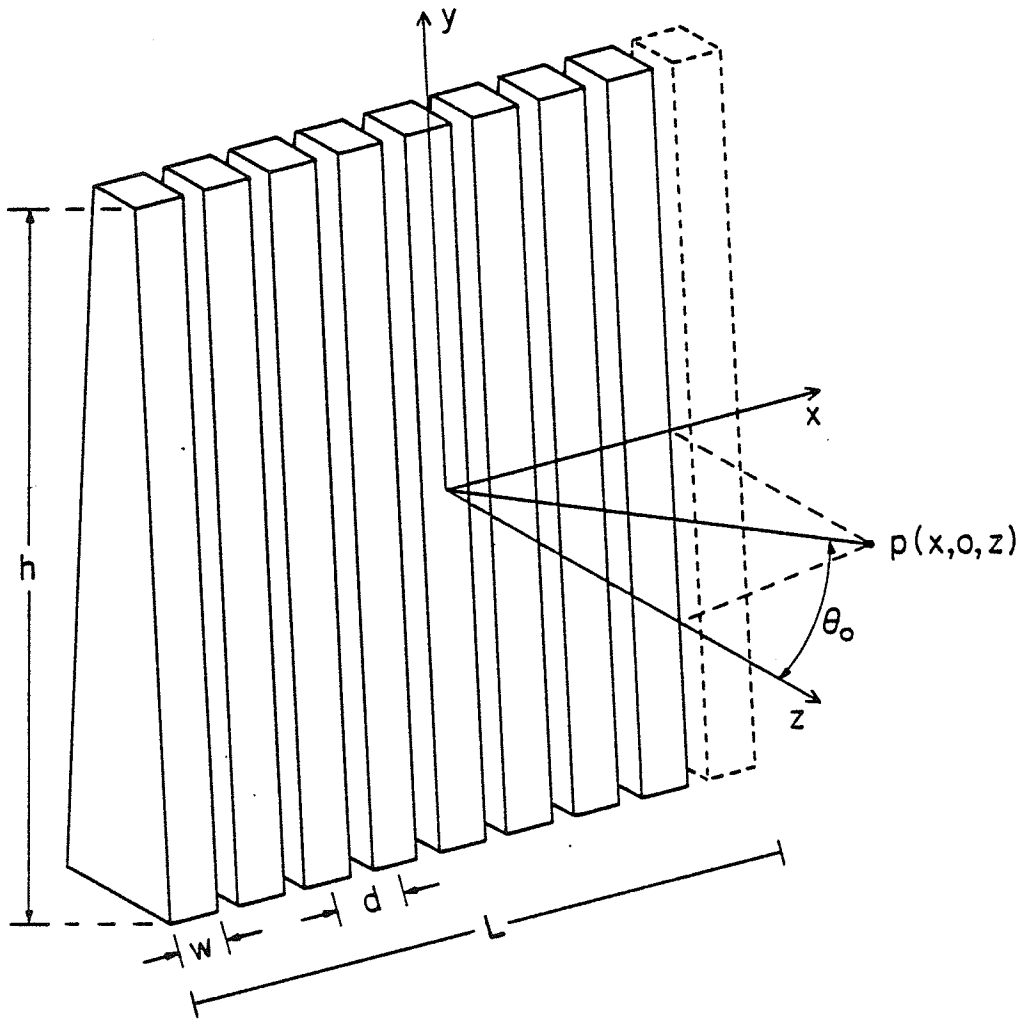

Figure 3.2. Tapered phased array.

element that has a thickness resonant at the frequency of the driving signal will produce the greatest acoustical power output. Thus, different regions along the length of the element can be excited by changing the frequency of the cw signal driving the element. A tapered phased array allows the focal region to be swept in two dimensions by controlling the phases of the cw signals, and in the third dimension by controlling the frequency of those signals. This tapered array would have the square root of N elements compared with N elements for a two-dimensional array with the same center-to-center spacing of elements.

The dimensions associated with tapered phased array elements are shown in Fig. 3.2. The height of an element, h, corresponds to its dimension in the y direction, and the overall length of the array in the x direction is L. The element width is w and the center-to-center spacing of the elements is d. The steering angle θ_o is the angular position of the focus with respect to the axis of the array projected onto the y = 0 plane. For an ideal linear array, the far-field radiation pattern in the y = 0 plane can be expressed in terms of relative magnitude as a function of the observation angle θ by

$$A(\theta) = \text{sinc}\left(\frac{\pi w}{\lambda}\sin\theta\right)\frac{\sin\left[\frac{\pi N d}{\lambda}(\sin\theta - \sin\theta_o)\right]}{\sin\left[\frac{\pi d}{\lambda}(\sin\theta - \sin\theta_o)\right]} = A_e(\theta) \times A_a(\theta) \qquad (3.1)$$

where N is the number of array elements [28]. The term $A_e(\theta)$ is the field pattern of a single element and $A_a(\theta)$ is the diffraction pattern which results from applying the appropriate phase shifts to the individual elements of the array. The overall pattern is

the product of these two functions. Thus, it is clear from Eq. (3.1) that decreasing the element width will result in a more uniform beam amplitude with steering angles.

The element center-to-center spacing, d, is of particular interest since it affects the location of the grating lobes which, in general, can appear in the real or visible region in addition to the side lobes and the main lobe. The grating lobes also result from constructive interference from each element, and their presence decreases the energy in the focal region [29]. The angular locations of the grating lobes, ϕ, are given by

$$\phi = \sin^{-1}\left(\frac{\lambda n}{d}\right) \tag{3.2}$$

where ϕ is in the $y = 0$ plane, λ is the wavelength, and $n = \pm 1, \pm 2, \pm 3$, etc., specifies the order of the grating lobe. When a beam steering angle of θ_o is introduced, the angular locations of the grating lobes are given by

$$\phi = \sin^{-1}\left(\frac{\lambda n}{d} - u_o\right) \tag{3.2}$$

where

$$u_o = \sin \theta_o$$

From this relation the spacing for grating lobes along x for constant $z = z_o$ are approximately

$$x = z_o \tan\left(\sin^{-1}\left(\frac{\lambda n}{d} - u_o\right)\right) \tag{3.3}$$

If d is equal to λ, the grating lobes will be absent for a steering angle of 0 degrees. However, the grating lobes will be present for a non-zero value of θ_o and will increase in

amplitude with increasing magnitude of θ_o [29]. On the other hand, if $d \leq \lambda/2$ then no grating lobes will be in the visible region ($-90^o < \theta < 90^o$) for any steering angle. Since grating lobes are a result of the periodic spacing of the array elements, they may also be avoided by unequal spacing of the elements [30]. However, the sidelobe amplitudes in these aperiodic arrays are significantly increased.

In order to minimize the number of elements and associated phasing and amplifier hardware, it would be desirable to make the elements as wide as possible without significantly decreasing the energy in the focus. To accomplish this, the spacing between the main lobe and the first grating lobe, λ/d, should be made greater than the value of u_o for the maximum beam steering angle. For example, if the largest tumor to be treated is 5 cm in diameter, and at a minimum possible depth of 10 cm, the largest steering angle required is 14 degrees. From Eq. (3.2) with $d = 0.8\lambda$, the focus can be steered off axis by 14 degrees without the center of the first grating lobe appearing in the visible field. Therefore, using a center-to-center spacing of 0.8λ instead of $\lambda/2$ would decrease the total number of elements in the array without significantly decreasing the energy in the focused main lobe.

3.2 Region of Excitation

The region of excitation for the tapered array will be centered on that portion of the element having a thickness resonant at the applied frequency. The extent of the region of excitation in the y direction is determined by the rate of taper and by the mechanical quality factor, Q_m, of the ceramic. A crude

approximation of Q_m for an air-backed transducer, which does not consider losses in the ceramic or associated with the transducer mounting, is given by

$$Q_m = \frac{\pi \rho_m c_m}{2 \rho_o c_o} \tag{3.5}$$

where $\rho_m c_m$ is the product of density and sound velocity in the transducer material, and $\rho_o c_o$ is the product of density and sound velocity in the loading medium [31]. Due to mounting losses, losses within the material and the narrow width of the elements, the actual Q_m will be significantly lower than the value computed using Eq. (3.4). These additional losses reduce the energy radiated from the elements.

The 3 dB length of the excitation region of the tapered element, h', can be estimated from the following equation

$$h' = \frac{hf}{Q_m (f_u - f_l)} \tag{3.6}$$

where h is the height of the element, f_u and f_l are the upper and lower resonant frequencies, and f is the operating frequency. This equation shows that the region of maximum excitation along the height of the tapered element, as well as the resulting beam width in the y direction (unfocused), will change with frequency. In order to determine theoretically the intensity field patterns of the array, the output along the height of the tapered elements must be estimated.

The electrical analog of a lossless mechanical piezoelectric transducer near resonance is shown in Fig. 3.3 [32]. The acoustic power radiated by the transducer is analogous to the average power dissipated in R_n. In terms of the properties of the

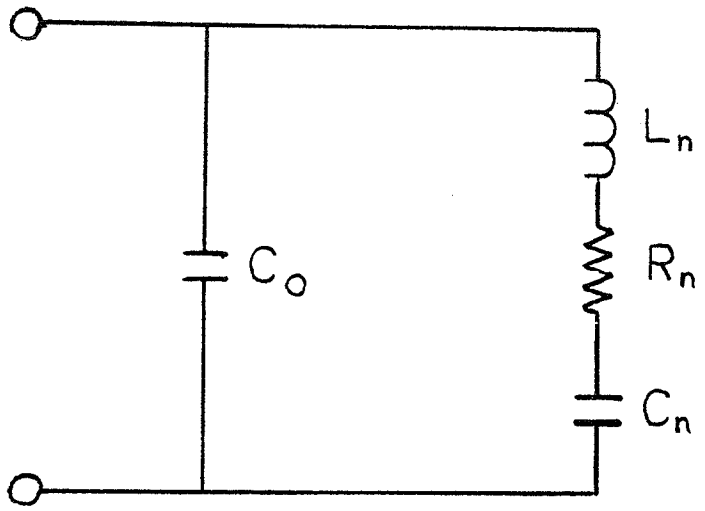

Figure 3.3. Electrical analog of a mechanical piezoelectric transducer near resonance [32].

ceramic and radiation medium, R_n can be expressed as

$$R_n = \frac{\rho_2 c_2 d_n^2}{2e_{11} S} \tag{3.7}$$

where ρ_2 and c_2 are, respectively, the density and speed of sound in the radiation medium, d_n is the ceramic thickness, e_{11} is the piezoelectric constant, and S is the equivalent radiating surface area of the ceramic. The inductance, L_n, and capacitance, C_n, can be expressed as

$$L_n = \frac{\rho d_n^3}{8e_{11}^2 S} \tag{3.8}$$

and

$$C_n = \frac{4e_{11}^2 S}{d_n \pi \rho} \tag{3.9}$$

where ρ is the density of the ceramic. The capacitance, C_o can be expressed as

$$C_o = \frac{k_{11} S}{d_n} \tag{3.10}$$

where k_{11} is the permittivity of the ceramic. At resonance, the equivalent electrical circuit of the transducer will look like a resistance, R_n, in parallel with a capacitance, C_o. The tapered element can be modeled using a distributed network of these equivalent circuits, as shown in Fig. 3.4. The capacitance, C_o', is the equivalent parallel capacitance of all of the branches of the network. The impedance of one RLC branch of this model can be expressed as

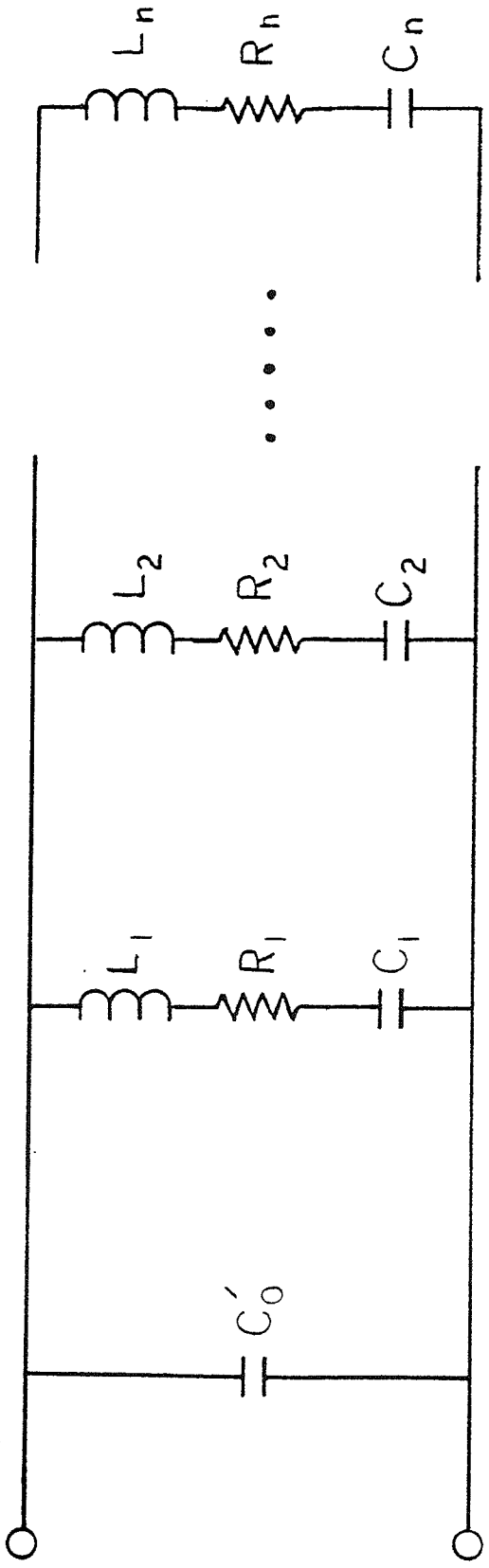

Figure 3.4. Distributed network model of a tapered piezoelectric ceramic.

$$Z_s(j\omega) = R_n[1 + jQ_m(\frac{\omega}{\omega_n} - \frac{\omega_n}{\omega})] \tag{3.11}$$

where

$$\omega_n = \frac{1}{(L_nC_n)^{1/2}}$$

is the resonance frequency of the nth branch. When the network is driven by a signal of frequency $\omega = \omega_1$, the position along the height of the element corresponding to the branch with $\omega_n = \omega_1$ will generate the greatest acoustical power output. The relative radiated power, W_n, from R_n in any branch can be expressed as

$$W_n = V^2[\frac{R_n^2}{|Z_s|^2}] \tag{3.12}$$

where V is the voltage applied to the element. Except for the thickness, d_n, of the ceramic, the remaining parameters in Eq. (3.7) will be independent of the y position along the element. Equation (3.7) can be rewritten in terms of the corresponding resonance frequency, ω_n, of the branch containing R_n as

$$R_n = \frac{\rho_2 c_2}{2e_{11}S}(\frac{\pi^2 c^2}{\omega_n^2}) \tag{3.13}$$

where c is the speed of sound in the ceramic. Substituting Eqs. (3.13) and (3.11) into Eq. (3.12) yields

$$W_n = K[\frac{\omega_n^2}{|1 + jQm(\frac{\omega}{\omega_n} - \frac{\omega_n}{\omega})|^2} \tag{3.14}$$

where

$$K = \frac{2V^2 e_{11}S}{\pi^2 \rho_2 c_2 c^2}$$

From Eq. (3.11), it is clear that the impedance for all of the branches, except for the resonant branch, will be complex.

This will result in a phase shift of the current with respect to the applied voltage. Thus, the phase of the acoustic pressure will vary along the y direction of the element. This phase shift, ψ,derived from Eq. (3.11), can be expressed as

$$\psi = \tan^{-1}(Q_m(\frac{\omega}{\omega_n} - \frac{\omega_n}{\omega})) \qquad (3.15)$$

Using Eqs. (3.14) and (3.15), the relative magnitude and phase of the acoustic output along the height of an element can be approximated. Figure 3.5 consists of plots of the magnitude and phase of the acoustical output versus y position, as determined from Eqs. (3.14) and (3.15). This figure shows that there is approximately a 140 degree phase shift present in the acoustical output. It is clear that such a phase shift must be considered when determining theoretically the field intensity profiles.

3.3 Array Intensity Gain

An important design conideration for the tapered phased array concerns the intensity gain required for preferential heating of the tumor. Without preferential heating, normal as well as tumor tissues will be heated to therapeutic temperatures. The array must provide time-averaged intensity gain so that the intensity averaged over a complete scan of the focus is greater at the tumor location than at the body surface and all other locations within intervening normal tissues. This gain, G_{ta}, is defined as the ratio of the time-averaged intensity at the tumor center to the time-averaged intensity at the body surface. Assuming, for this analysis, that the time-averaged intensities at the body surface and at the tumor are uniform in the x direction, a G_{ta} greater

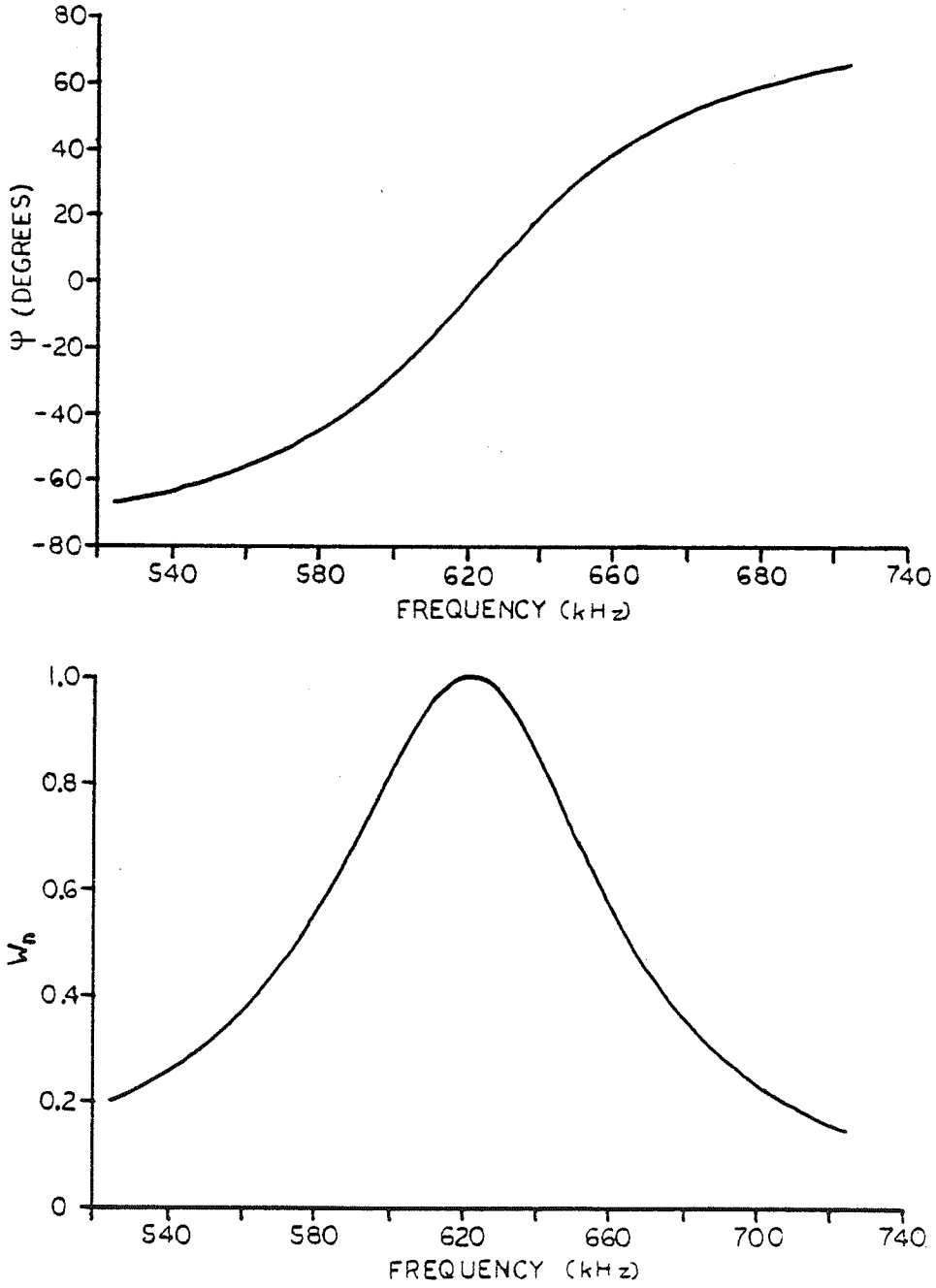

Figure 3.5. Plots of the relative magnitude and phase of the acoustical power output of a tapered element driven at 620 kHz, as determined from Eqs. (3.14) and (3.15).

than one is obtained by making the length of the array long compared to the tumor width [27].

Several studies of the theory of heating tumors using scanned focused ultrasound at 500 kHz have been carried out. One study indicated that a 2.4 cm diameter tumor located 4.3 cm in depth, could be heated to 43°C with minimal heating in normal tissues by a focused beam with a time-averaged intensity gain of approximately 2.4 dB [20]. Another study showed that a 4 cm diameter tumor at a depth of 13 cm could be heated to 43°C with a time-averaged intensity gain of 4.8 dB [33]. Based on these theoretical intensity gains, a G_{ta} of 3.0 dB was chosen for the tapered phased array. To determine more accurately the gain required for the tapered phased array, a computer simulation of the temperature distribution, based on the bio-heat transfer equation, would have to be developed.

To calculate the array length necessary to heat selectively a tumor of a given size, one must consider the following: (1) losses due to attenuation incurred along the path from the transducer to the tumor; (2) increased path length from elements at the ends of the array; (3) directionality of the elements; and (4) phase quantization errors. Phase quantization errors are introduced into the system when digital signal processing systems are used to produce the phase shifts necessary for focusing and steering. All of these factors are best considered by calculating the intensity field distribution produced by an array. A computer program was developed previously for this purpose [34]. The program divides the elements of the array into subelements that are small enough so that their fields can be represented, in the

region of interest, by the far-field approximation. The effect of the tapered elements was taken into account by weighting the magnitude and phase of the acoustic output of each subelement along the height of the element using the results from Eqs. 3.14 and 3.15, respectively. The total acoustic pressure at a specific point in the field is determined by summing the contributions at that point from each of the subelements. The program listing appears in the Appendix.

Using this model, the maximum treatable tumor diameter can be determined when the frequency, array length, and desired G_{ta} are specified. The gain in intensity at the focus relative to that near the surface of the array, G_f, can be determined from a plot of intensity versus distance from the array. This gain is large since such a plot does not consider the time-averaging resulting from scanning the beam in the x direction. This time-averaging effect is considered by multiplying G_f (expressed as a ratio) by the 3 dB beam width in the x direction. However, G_f must first be adjusted for the desired G_{ta}, defined previously, to yield the corrected gain, G_c, given by

$$G_c = G_f - G_{ta} \tag{3.16}$$

Thus, the maximum treatable tumor diameter D is approximately given by

$$D = B \cdot 10^{(0.1G_c)} \tag{3.17}$$

where B is the 3 dB beam width in the x direction [27].

For a tapered phased array with an array length of 12.63 cm, element center-to-center spacing of 1.97 cm, a frequency range of

580 to 650 kHz, and operating at 650 kHz (A = 0.1 Np/cm/MHz), the field intensity versus distance from the array along the z axis is plotted in Fig. 3.6. For points close to the array, the intensity is approximately 14 dB below the intensity at the focus resulting in a G_f of 14 dB. A corrected gain, G_c, of 11.0 dB is calculated from Eq. 3.16, based on a G_{ta} of 3 dB. The 3 dB beam width of the focus at 650 kHz, as measured from the plot of field intensity versus x in Fig. 3.7, is approximately 0.17 cm. Therefore, the maximum treatable tumor diameter is 2.1 cm at a depth of 8 cm, as calculated from Eq. 3.17.

In order to obtain the intensity gain necessary to treat tumors larger than 2.1 cm, the frequency range of the array would have to be less. With lower frequencies, the losses due to attenuation in the intervening normal tissue would be less, thereby increasing the intensity gain. However, the choice of the operating frequency range cannot be too low, because significant heating behind the tumor could occur. Many factors such as the normal and tumor absorption coefficients, perfusion levels in the tumor and surrounding tissue, and presence of bone behind the tumor will determine the minimum frequency that may be used. Based on the simulations of scanned focused ultrasound, it appears that frequencies in the neighborhood of 500 kHz could be used without excessive heating of the surrounding normal tissues [20,33]. For a tapered array operating at 500 kHz, with the same element spacings and array length as above, G_c and B can be determined from Figs. 3.8 and 3.9 to be approximately 16 dB and 0.2 cm, respectively. From Eq. 3.17, the maximum treatable tumor diameter is 4.0 cm, nearly double that of 650 kHz.

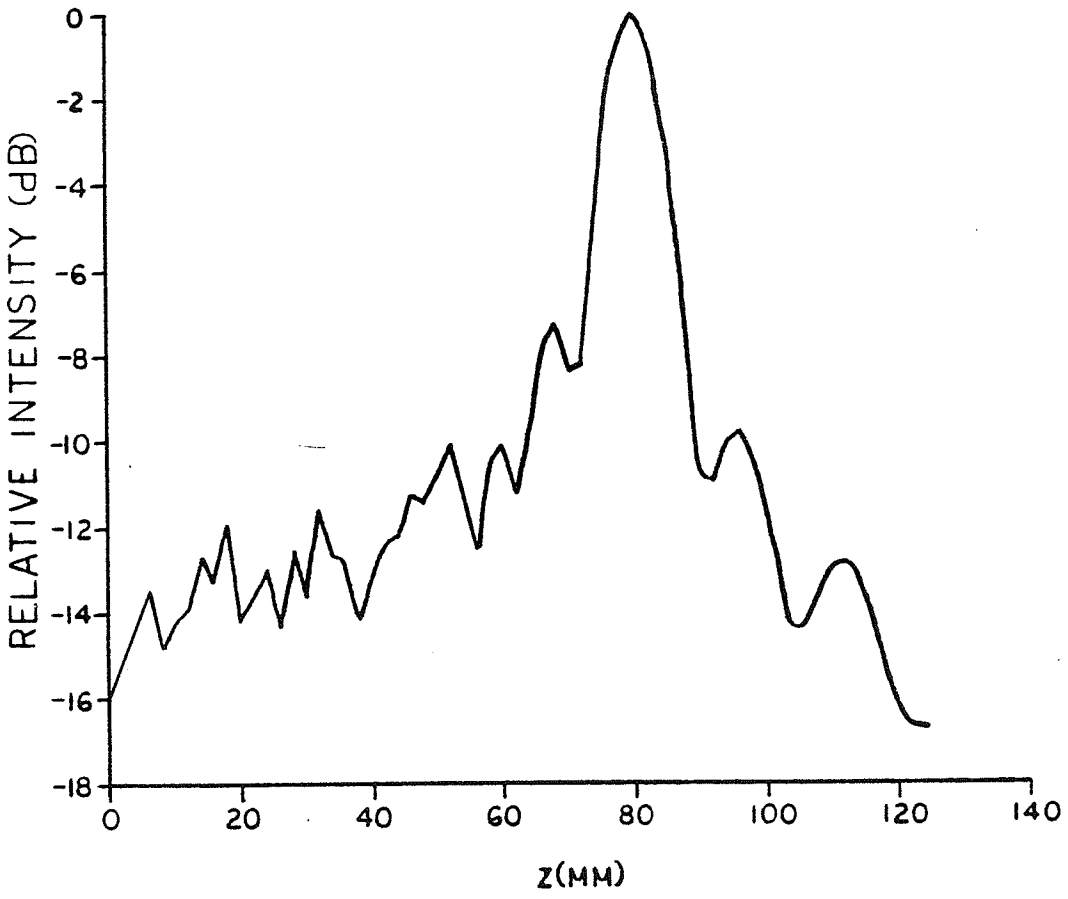

Figure 3.6. Relative field intensity versus z position, for the array focused at z = 80 mm (x = 0, f = 650 kHz, A = 0.1 Np/cm/MHz, d = 1.97 mm, w = 1.79 mm, 64 elements).

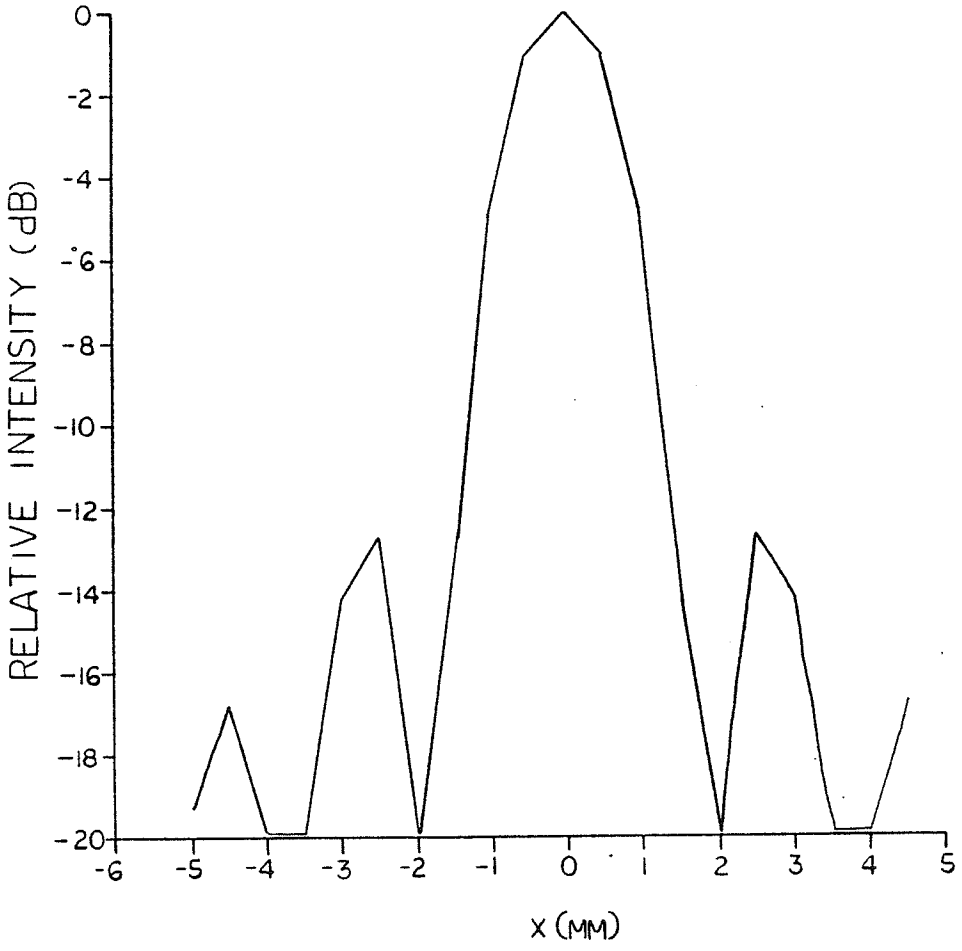

Figure 3.7. Relative field intensity versus x position, for the array focused at z = 80 mm (z = 80 mm, f = 650 kHz, A = 0.1 Np/cm/MHz, d = 1.97 mm, w = 1.79 mm, 64 elements).

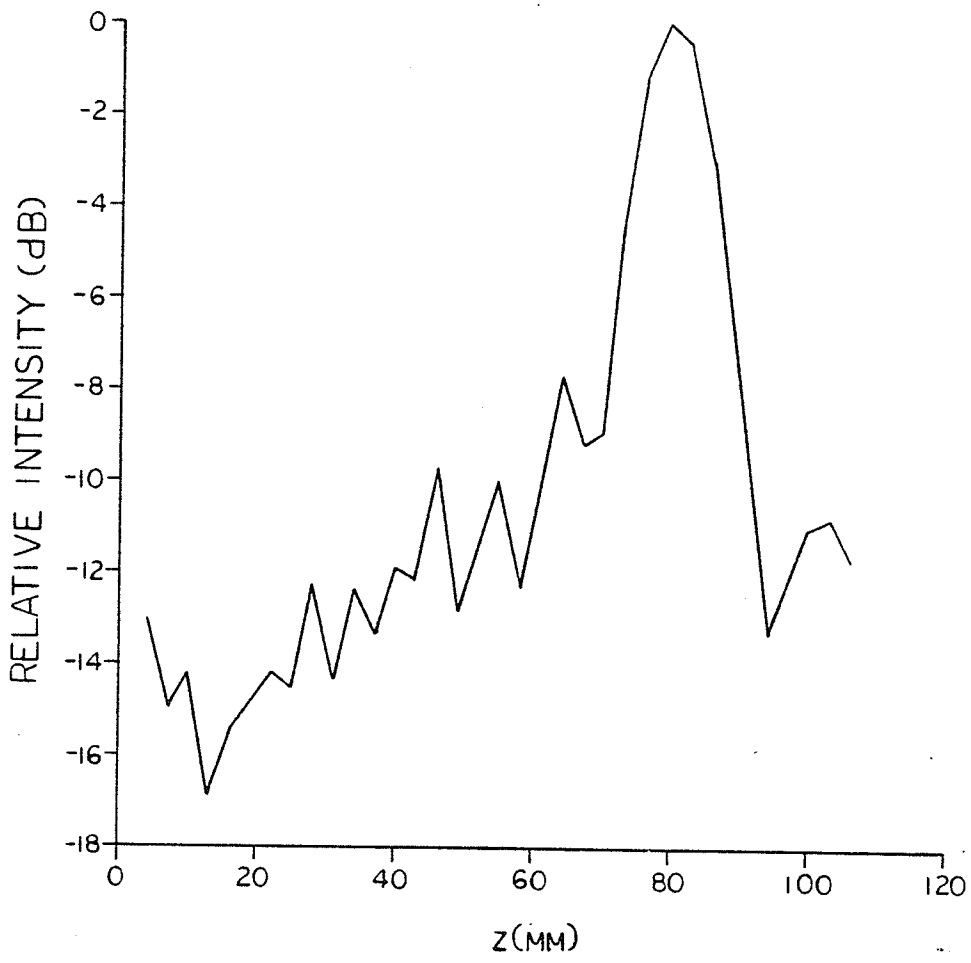

Figure 3.8. Relative field intensity versus z position, for the array focused at z = 80 mm (x = 0, f = 500 kHz, A = 0.1 Np/cm/MHz, d = 1.97 mm, w = 1.79 mm, 64 elements).

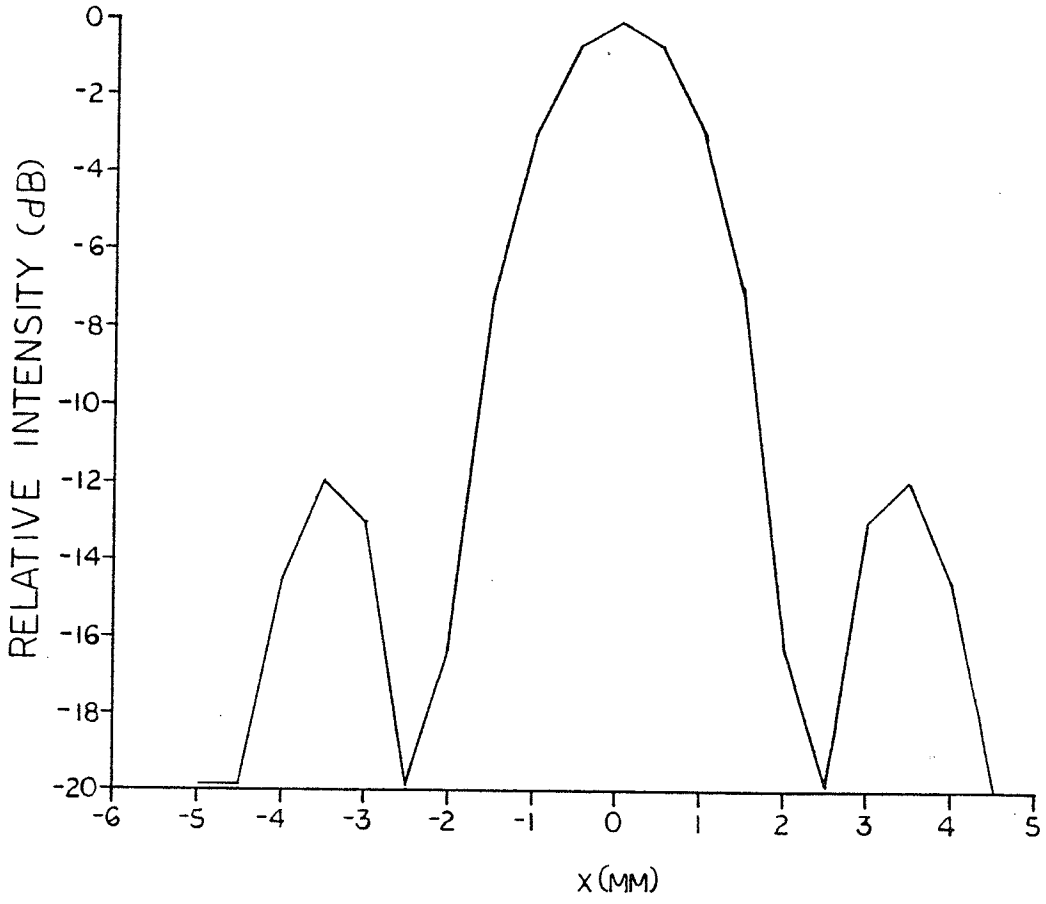

Figure 3.9. Relative field intensity versus x position, for the array focused at z = 80 mm (z = 80 mm, f = 500 kHz, A = 0.1 Np/cm/MHz, d = 1.97 mm, w = 1.79 mm, 64 elements).

3.4 Array Fabrication

The fabrication techniques employed for hyperthermia phased arrays are somewhat different from those of imaging linear phased arrays. Imaging arrays are typically constructed by mounting the uncut ceramic on a suitable backing material. The elements are formed by cutting completely through the ceramic plate and partially through the backing material. The backing material is partially cut in order to reduce the interelement coupling. A matching layer is then affixed to the radiating face of the array. The combination of the matching layer and the backing material makes the imaging array broadbanded, a desirable requirement for high resolution imaging systems. The phased arrays used for hyperthermia, on the other hand, operate with essentially cw signals so that the damping provided by a backing material is not only unnecessary, but undesirable because of the reduced efficiency that results from its use.

Several linear phased arrays were constructed using a technique that does not require the elements to be physically separated. In this simplified transducer design, each array was fabricated on a single piezoelectric ceramic plate, with grooves cut to a specified depth between the elements, rather than using individual ceramic elements. A single ceramic plate, with the uncut grounded face on the outside of the transducer housing, eliminated the need for backing support material and/or a faceplate, as required when separate elements are employed. This fabrication technique proved to be unsatisfactory. The uncut portion of the ceramic plate coupled excessive amounts of energy between the elements (see Section 6.1).

A second fabrication technique, which involved cutting the ceramics into completely separate elements, was examined. In this approach, the ceramic plate was affixed to a glass plate with wax and cut into narrow elements using a 0.25 mm wide diamond saw blade. Once cut, a metal foil was attached to the front face of the elements using a conducting epoxy to provide a grounded, water tight front surface for the elements. When the epoxy cured, the wax was heated and the elements, with their spacing maintained by the foil face, were removed from the glass plate. Several problems arose with this technique, the most serious of which was the fragility of the completed array. Small movements of the elements during the mounting of the array in its housing caused the foil face to tear.

A third fabrication technique, a modification of the second, proved to be successful. Instead of a foil face to maintain the element spacing, the elements were mounted on a frame with nonconducting epoxy before removal from the glass plate. The frame, with the array mounted in it, served as the front face of the transducer housing. In order to maintain a water tight front face, a mylar sheet with a 25.4 μm thickness, was affixed to the face of the array using a silicone rubber sealant around the edges. A thin film of vacuum grease was used to provide an acoustical coupling medium between the array and the mylar sheet. The transparent mylar sheet was used so that any damage to the elements or poor contact with the sheet would be visible. The only problem encountered using this technique was a small amount of chipping of the nickel electroding material on the face of the array that was affixed to the glass plate. It is believed that

this was due to small air pockets in the wax that allowed the saw blade to chip the electrode along the edges of the cuts.

Two tapered phased arrays were fabricated using the above technique. The elements for both arrays were cut from a 15.2 cm by 15.2 cm Channel 5800 ceramic plate with a tapered thickness of 4.3 mm to 5.8 mm, corresponding to a resonance frequency range of 650 to 850 kHz prior to cutting the elements. The first array, TPA1, consisted of 90 elements, 1.4 mm in width with a center-to-center spacing of 1.6 mm. The second array, TPA2, used 64 elements with a 1.79 mm width and a 1.97 mm center-to-center spacing. These arrays were constructed with different element widths to study the maximum acoustical power output versus element width. There were small variations, typically less than 0.18 mm, in the widths of the elements due to errors in the positioning of the diamond saw blade. The possible effects of these variations are discussed in Section 6.1.

When the tapered ceramic plate is cut into narrow elements, the resonance frequency range will no longer be determined by the common thickness mode resonance, as is the case when the width of the ceramic is substantially larger than its thickness. Instead, the thickness dilational mode, which occurs when the width of the ceramic is less than its thickness, will be the dominant resonance mode. In this mode, the resonance frequency of the elements, f_r, can be very approximately expressed as

$$f_r \doteq \frac{2.33c}{t} \tag{3.18}$$

where c is the velocity of sound in water, and t is the thickness of the ceramic [35]. From this equation, the resonance frequency

range of the elements is expected to be approximately 595 to 800 kHz.

To measure the resonance frequency range of the elements, a hydrophone probe was swept along the height of an element, close to its surface, to determine the location of the maximum acoustic pressure for a given frequency. The measured resonance frequency ranges of TPA1 and TPA2 were approximately 500 to 700 kHz. For this range of frequencies, the element center-to-center spacing varied from 0.52λ to 0.71λ for TPA1 and 0.60λ to 0.85λ for TPA2. These spacings were chosen for the two arrays so that the relationship between element width and grating lobe energy, discussed in Section 3.1, could be examined experimentally.

The nickel electrodes of the tapered ceramic allowed leads to be soldered directly to the elements with little difficulty. However, due to the low conductivity of the nickel electrodes, and the narrowness of the elements, an approximately 10 ohm dc resistance was measured between the ends of the element electrode. To minimize the effect of this resistance, two leads spaced 5 cm apart were soldered on each element.

3.5 Electrical Impedance Matching Network

The electrical input impedances of the elements of TPA1 and TPA2, including a 5 m length of RG174 coaxial cable, were measured at frequencies between 580 kHz and 650 kHz. This was the frequency range first chosen to operate the arrays for two reasons: (1) this range would allow the focus to be moved a significant distance in the y direction, approximately 6 cm, without significant degradation from damping effects that occur at

the ends of the elements; and (2) the electrical matching was simplified since the imaginary parts of the impedances were the least for this range. The average values of the impedances for three frequencies in this range, for the two arrays, are listed in Table 3.1.

Table 3.1 Average electrical impedances of TPA1 and TPA2 elements.

Frequency (kHz)	Impedance (ohms)	
	TPA1	TPA2
580	162 $\angle -44^{o}$	115 $\angle -32^{o}$
625	180 $\angle -43^{o}$	152 $\angle -20^{o}$
655	200 $\angle -32^{o}$	175 $\angle -1^{o}$

Since the elements were to be driven over a range of frequencies, elimination of the imaginary part of an element's impedance over that range would have required a complex matching network consisting of many components. For this study, a simpler matching network that minimized the reactance of the load over the operating frequency range was employed. Figure 3.10 shows the matching network chosen for TPA2. The network was located on each amplifier circuit board (see Section 4.1), instead of inside the transducer housing, to minimize the size of the housing. The bandpass LC filter, on the primary side of the matching transformer, filters the square wave output of the amplifier. The filter has a Q of approximately 4.0, which provides a 3 dB bandwidth of 135 kHz. The transformer is used to match the output impedance of the amplifier (approximately 6 ohms) to the element's

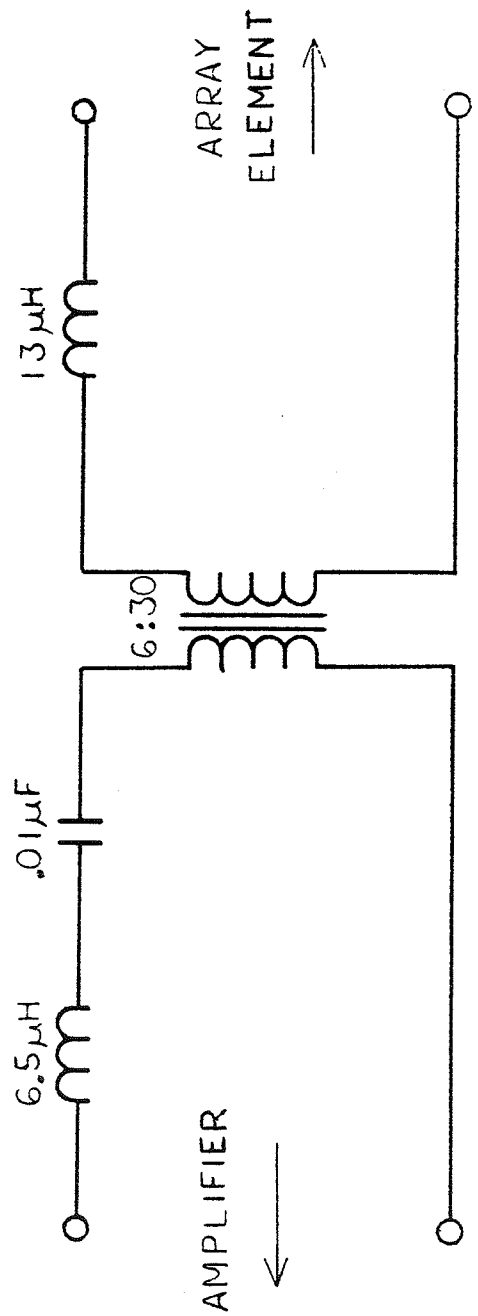

Figure 3.10. Electrical impedance matching network for a tapered phased array element.

impedance. The series inductor on the element side of the transformer is used to cancel approximately the parallel capacitance of the cable and element.

CHAPTER 4

EXPERIMENTAL TECHNIQUES

4.1 Transducer Controllers

Two different driving systems were used to control the multielement transducer. Initially a function generator (Wavetek 143) was used to provide the 1 MHz input signal to the 500 W Class E RF power amplifiers (URI Therm-X, Inc.) which amplified the signals applied to the elements of the transducer. The only control was the on/off control of the individual amplifiers. This simple system was used to make the acoustical power output and field intensity profile measurements, as well as the non-perfused tissue heating measurements. The second driving system was based on a multielement transducer controller recently developed [36]. This system provided individual duty cycle control of the input signals to the RF power amplifiers, and thus control over the time-averaged intensities produced by each transducer element. It was also used for the perfused tissue phantom studies.

A recently developed ultrasound phased array controller was used to position the focus of the tapered phased array at any of 4096 predetermined locations [37]. The controller generates the signals of appropriate phase, which are amplified by 50 W RF power amplifiers (prototype Class E power amplifiers, URI Therm-X, Inc.) and used to drive the elements of the array. The location of the focus can be scanned in time over any predetermined three-dimensional path, and the time averaged intensity at each individual focal location can be adjusted using duty cycle control. A CRT terminal (Televideo 910) was used to program the

controller through its RS 232 port. An LED display was used to indicate the instantaneous site of the focus. The controller was designed to have a frequency selectable clock, sixteen times the driving frequency, to move the focus in the y dimension. However, for the initial studies, frequency control was provided by a function generator (Wavetek 143) that served as the controller's clock source.

4.2 Acoustical Power Output Measurements

The acoustical power outputs of the multielement and tapered phased array transducers were determined by measuring the radiation force exerted on a reflecting target. The target was 7.6 cm x 5.1 cm x 0.3 cm and consisted of approximately 200 m thick brass plates bonded to each side of a rectangular Plexiglas frame. An air gap between the plates made the target virtually a perfect reflector. The target was suspended at an angle of 45 degrees to the incident field by a small diameter nylon thread, as illustrated in Fig. 4.1. The target was suspended within a Plexiglas frame with acoustic windows in the front and rear to prevent convection and acoustic streaming from affecting the response of the target.

The total acoustic power incident on the target, W, was determined from

$$W \doteq \frac{mgcd}{(L^2 - d^2)^{1/2}} \tag{4.1}$$

where m is the mass of the target, corrected for buoyancy, g is the gravitational constant, L is the length of the suspension, c is the speed of sound, and d is the horizontal deflection of the

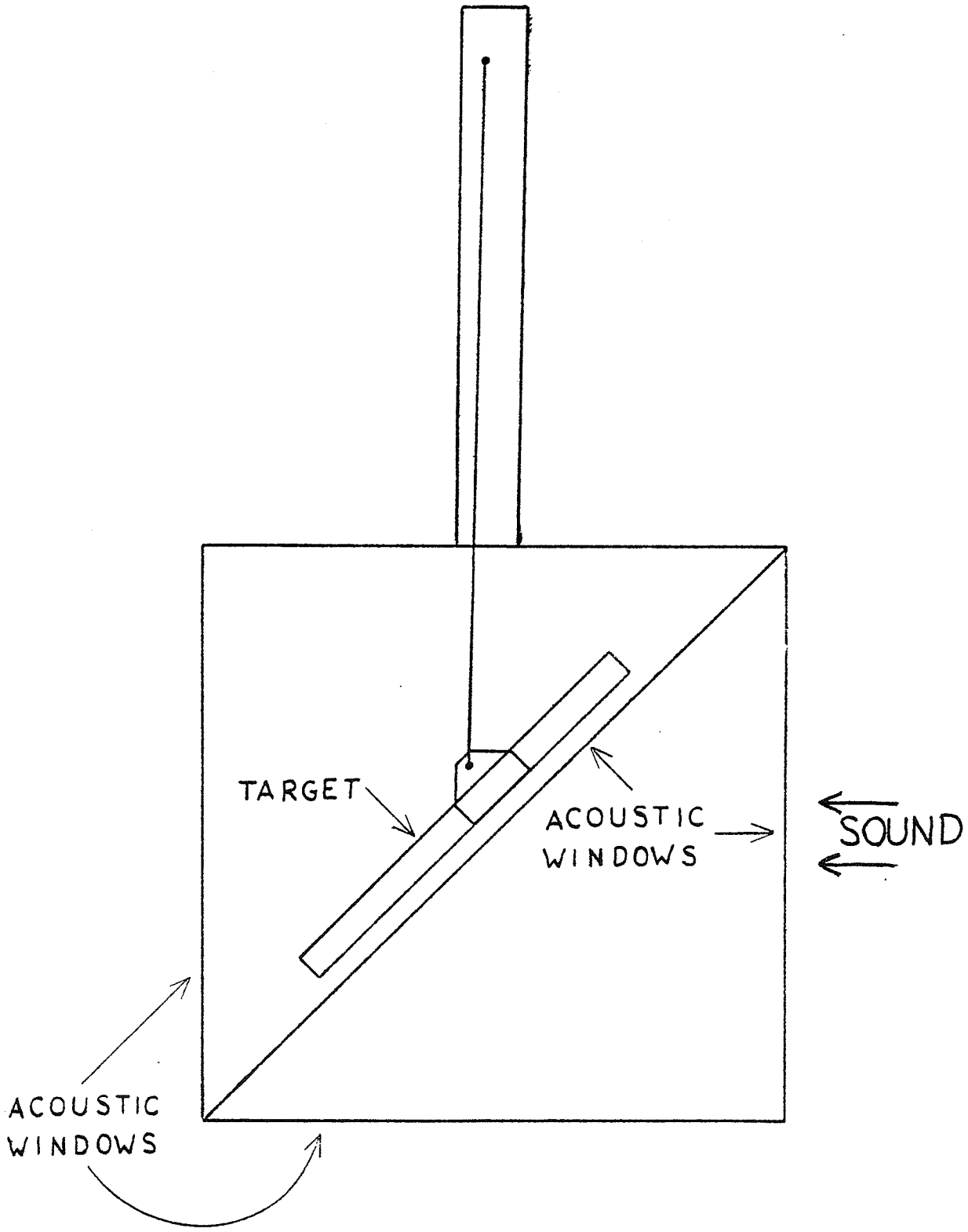

Figure 4.1. Radiation force target and assembly.

target which occurs when the sound is present. The deflection, d, was measured with a cathotometer which could accurately measure deflections to 0.2 mm. The deflection of the target was limited by contact with the rear acoustic window in the frame to approximately 2.5 cm. At the maximum deflection, the target was raised 1.94 mm from its resting position, along the deflection arc. This would result in the center of the ultrasound beam striking the target below its center line, and in the case of a narrow beam, could cause the target to deviate significantly from the prescribed 45^{o} angle. Such a deviation would reduce the deflection of the target and thus give an erroneous measurement of the field. However, the two transducers tested had beamwidths sufficiently large to maintain the desired 45 degree angle approximately.

Since the mass of the target (10.84 g in water) was not large enough to measure acoustical power greater than approximately 50 W, additional weights (18.73, 43.0 and 61.73 g in water) were added to the back of the target to reduce the sensitivity. With the 61.73 g weight added to the target, acoustical power to approximately 180 W could be measured. The resolution of the measurement system depended upon the sensitivity of the target and ranged from 0.38 W (no weights added) to 1.5 W (with a 61.73 g weight added).

The voltage applied to an element of the multielement transducer, as measured with a voltmeter (Hewlett Packard 410C), and the impedance of the element, measured with a vector impedance meter (Hewlett Packard 4193A) at $23^{o}C$, was used to calculate the electrical power delivered. Since 32 elements of the tapered

phased array were driven simultaneously, taking electrical power measurements for each element, as was done for the multielement transducer, was not feasible. Instead, the input electrical power from the dc power supply (Electronic Measurements, Inc. TRC150S18) was measured. The total electrical power delivered to the array, based on the average efficiency of the amplifiers, was approximately 80% of the input power from the supply.

During the acoustical power output measurements, the temperature rise at the back surface of an element was measured using a 75 μm thermocouple. A thin layer of insulation was applied to the thermocouple junction, and the insulation was epoxied directly to the back of the element to insure the closest possible proximity to the ceramic plate. Also, the junction was coated with heat sink compound to improve the thermal conductivity between the ceramic and the thermocouple. A three-channel digital thermocouple thermometry system (Bailey Instruments BAT-8) was used to measure the temperature. To prevent RF artifacts, the temperatures were recorded immediately after turning off the RF.

4.3 Field Intensity Profile Measurements

The field intensity profiles were determined by mounting the transducer to the inside surface of a wall of a 50-liter Plexiglas tank filled with degassed water and with the inside walls lined with sound absorbing material. The tank was mounted on a milling base whose movement in three rectangular coordinate directions could be either controlled manually or by a computer. A hydrophone probe, consisting of a 1 mm-diameter, 20 MHz PZT-5A ceramic disk mounted at the tip of a rigid coaxial rod, was used

to observe the acoustic field pressure produced by the transducer. The probe, held in place by a metal rod, remained stationary while the milling base moved the tank and the transducer. The output of the hydrophone probe was amplified by a video amplifier with a gain of 35 dB and measured using a digital voltmeter (Fluke 8920A) with an analog dc output. The analog output signal was routed to a 25 kHz analog-to-digital converter connected to a minicomputer (Perkin-Elmer 7/32). The minicomputer was programmed to move the tank continuously in the desired coordinate direction and to record the field pressure data from the hydrophone at 2 mm intervals. These data were squared and converted to decibels relative to the peak amplitude for storage on magnetic tape as relative intensity. The quantization error in this measurement system was approximately 0.1 dB. During periods when the minicomputer was not functioning, the data were collected by moving the milling base manually and manually recording the output of the digital voltmeter.

An oscilloscope (Tektronix 2445), with a resolution of approximately 14 degrees, was used to measure the phase of the output of the hydrophone probe relative to the applied electrical signal along the y dimension of the element.

4.4 Non-perfused Tissue Heating with the Multielement Transducer

The temperature rise produced by the multielement transducer was measured in *in vitro* samples of pig heart muscle mounted in a Plexiglas holder. Lap soldered, 75 μm copper-constantan thermocouples were inserted at 3, 10, and 30 mm depths in the tissue using a 20-gauge trocar to create an insertion path. The

holder, with the tissue, was placed with the transducer in a 50-liter tank filled with degassed water at 25°C as a coupling medium. The surface of the tissue was 7.6 cm from the face of the transducer, positioned such that the thermocouples were in the center of the transverse field of the active elements. The 7.6 cm distance was chosen as the approximate thickness of a coupling bolus containing degassed water that would be required to couple the energy from the transducer to the patient in a clinical system. The coupling water in the bolus would also provide cooling to the surface of the patient, to prevent excess skin heating, and cool the face of the transducer. A three-channel digital thermocouple thermometry system (Bailey Instruments Bat-8) was used to monitor the tissue temperature. The temperature data were recorded every 10 seconds from the three thermocouples imbedded in the tissue.

4.5 Non-perfused Phantom Heating with the Tapered Phased Array

A non-perfused tissue mimicking phantom (URI Therm-X, Inc.) was used to study the heating capabilities of the tapered phased array transducer. The phantom was approximately 20 cm by 20 cm across and 6 cm deep. The phantom material was an agar gel, impregnated with carbon to produce a thermal conductivity of 0.68 $W/m^2{}^oC$, an acoustic absorption coefficient of approximately 0.068 Np/cm/MHz, and a speed of sound of approximately 1544 m/s.

The phantom contained 28 thermocouples, laterally spaced 3.8 cm apart, imbedded at depths of 1, 2, 3 and 5 cm. Since the lateral spacing of the thermocouples was so large, only two lateral thermocouples at both the 2 and 5 cm depths were used to

monitor temperature. The four thermocouples were connected to a multichannel thermometry system (URI Therm-X, Inc. TX-100) for temperature measurement, which was configured with a microcomputer (Apple IIe). The Apple IIe was connected to the thermometry system by an RS-232 serial communications port. Temperature data was acquired from all channels every two seconds and stored on a floppy disk. The transducer was mounted on one wall of a 175-liter tank of degassed water which also contained the phantom. The phantom was attached to a three-dimensional stepper motor positioning system, and positioned such that the focal region of the transducer in the y direction was aligned with the four thermocouples.

4.6 Perfused Phantom Heating

The perfused tissue phantom employed in this study was a fixed pig kidney. The fixation technique required perfusion with a graded series of ethyl alcohol mixtures immediately after excision [38]. The kidney was stored in alcohol and rehydrated with degassed water perfusate for several hours before use to remove all traces of alcohol from the tissue. The fixed kidney possesses a system of perfusion channels whose structure closely resembles that of the living organ, and it can be perfused with degassed water at a variety of flow rates, including those found in organs *in vivo*.

It was found previously that the intrinsic thermal conductivity, k, of the fixed kidney cortex increased by approximately 10% while that of the medulla was essentially unchanged when compared to the respective values found in the

freshly excised organ [39]. The absorption coefficient at 1 MHz in the rehydrated fixed kidney was measured to be 0.014 Np/cm, which is approximately half that for a freshly excised kidney [21]. The weights of the kidneys used as phantoms ranged between 44 and 108 g.

Data from the literature suggest that a majority of solid tumors, especially carcinomas, have average perfusion rates that are lower than those found in well perfused normal tissues such as liver and kidney [40]. The blood flow rate in human tumors generally is between 0.1 and 2.0 ml/min/g, but can be as high as 34 ml/min/g, as in the case with some osteosarcomas [40]. Therefore, to simulate the perfusion conditions that are most commonly found in tumors, the kidney phantom was perfused with degassed water at flow rates of 0, 1.1, and 2.2 ml/min/g.

Pig liver, prepared in the same manner as the kidney, was also used as a perfused tissue phantom. There are several advantages in using the liver rather than the kidney. Since the liver is more homogeneous, it is more evenly perfused than the kidney, which has different levels of perfusion in the medulla compared with the cortex. In addition, the liver is much larger than the kidney, thereby allowing the study of heating with all of the transducer's elements excited simultaneously.

The phantom under test was mounted in a Plexiglas frame using two 0.5 mm diameter metal rods that pierced its extreme lateral ends and fastened to the frame. The frame, with the phantom mounted on it, was placed in a 50-liter tank filled with degassed water. A calibrated, variable flow rate roller pump (Masterflex 7520-35) was connected to the renal artery of the kidney, or the

portal vein of the liver, and circulated the degassed water perfusate, which also served as the coupling medium, in the tank. The renal vein and hepatic vein of the kidney and liver, respectively, were allowed to drain into the tank. Because of the relatively small dimensions of the kidney (average size was 8 cm x 4 cm x 3 cm), they were irradiated with only two of the multielement transducer's sixteen elements (total active surface of 3.8 cm x 7.6 cm). The liver (approximately 15 cm x 15 cm, 460 g), was irradiated with all 16 of the transducer's elements. Temperatures in the tissue were measured using copper-constantan (75 μm wire size) thermocouples, constructed by lap soldering the two ethyl alcohol cleaned wires with an oxide-free solder cream (Multicore Solder SN62 PRAB3). The thermocouples were inserted at various depths and lateral positions throughout the phantoms using a 1 mm-diameter trocar to create the insertion path. The temperatures were recorded by the multichannel thermometry system configured with the microcomputer, as described in Section 4.5.

CHAPTER 5

EXPERIMENTAL TESTS OF THE MULTIELEMENT TRANSDUCERS

5.1 Comparison of Theoretical and Experimental Field Intensity Distributions

Field intensity distributions were determined for MET1 and revealed significant decreases in intensity at locations corresponding to the joints between the four ceramic plates. These consisted of a region approximately 3 cm across with an average intensity approximately 6 dB below the field maxima associated with the two adjacent elements, as shown in the sample transverse field plot of Fig. 5.1. No large minima were observed in the transverse field between any two elements on the same plate, which were defined by scratching the positive electrode on the back surface. Initially the nonuniformity occurring between plates was thought to be due primarily to the 6.4 mm-wide frame that covered the joints on the front face of the transducer. Thus, MET2 was designed to eliminate the front bar over the joints and to decrease the space between the plates. Transverse field intensity distributions for MET2 were measured and the results (see a typical field plot in Fig. 5.2) showed that an unacceptable nonuniformity across the joints between plates persisted. This suggested that the decreased intensity at the joints was due to the damping effects of the underlying supporting frame and the epoxy used to hold the plates in place. MET3 was constructed using a single ceramic plate in place of the four plates, thereby eliminating any mechanical supporting structure between adjacent elements of the transducer. Transverse field

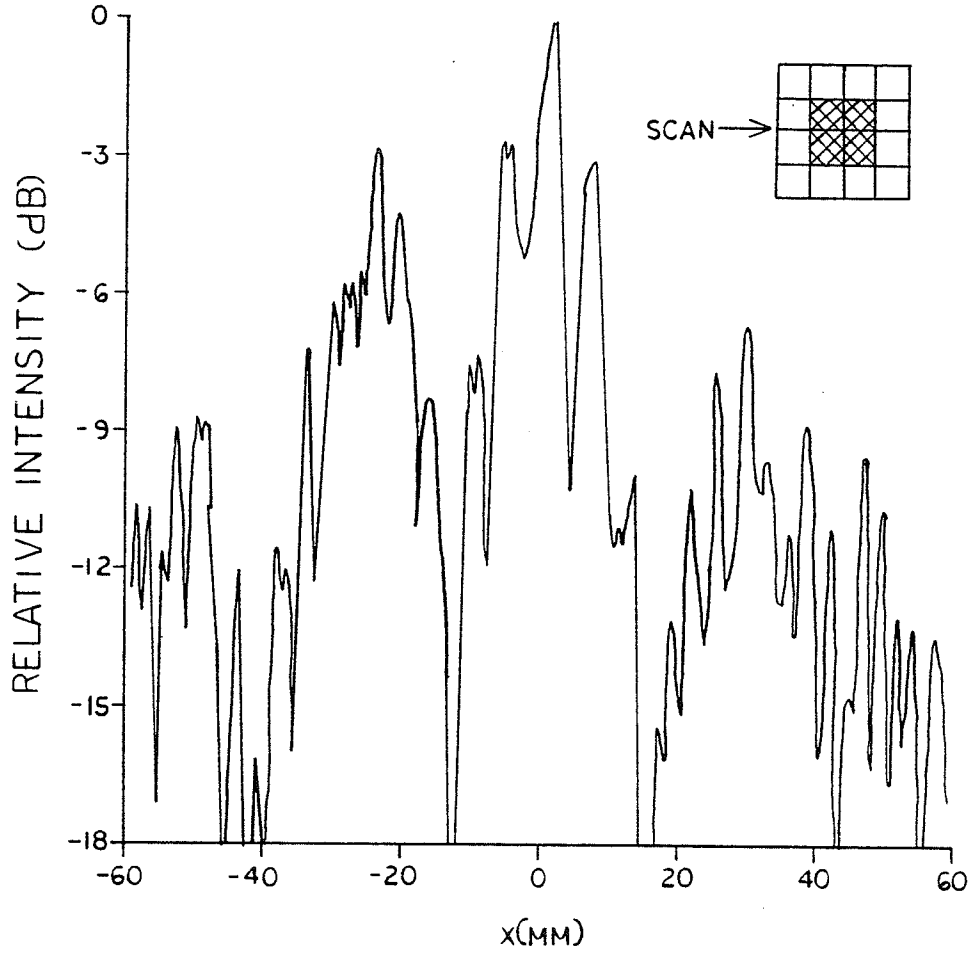

Figure 5.1. Relative field intensity of MET1 versus x position (z = 7.6 cm).

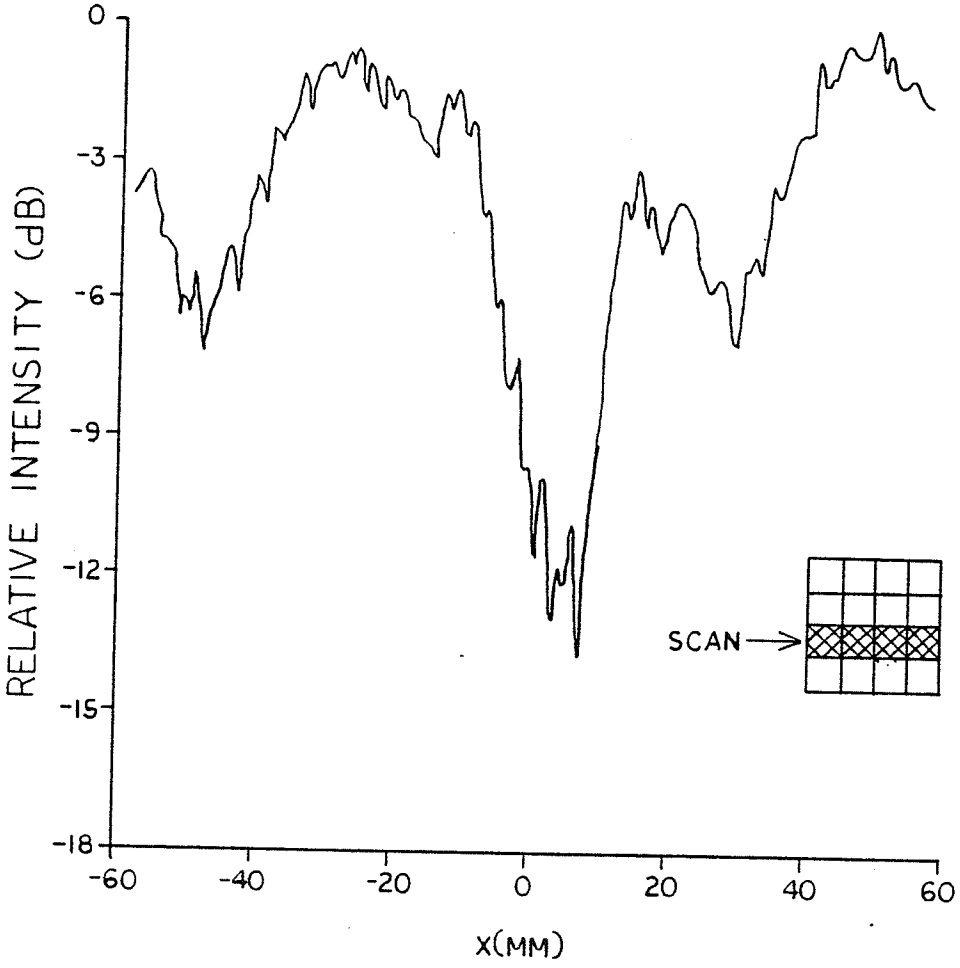

Figure 5.2. Relative field intensity of MET2 versus x position (z = 7.6 cm).

intensity distributions for MET3, as shown in the example of Fig. 5.3, confirmed that there were no large minima in the field between adjacent elements. This is the expected result based on the results from adjacent elements on a single plate for MET1 and MET2. The remainder of this chapter is devoted to the results obtained testing the applicability of MET3 to hyperthermia treatment.

The computer program used to predict theoretically the field distribution of the tapered array was modified for use with the multielement transducer by eliminating the weighting and phasing factors associated with the tapered elements. The program listing can be found in the Appendix. Figure 5.4 shows a comparison of typical experimental and theoretical transverse field intensity distributions, with four linearly adjacent elements excited, 7.6 cm from the face of the transducer. The 7.6 cm distance was chosen since that would be the approximate distance from the transducer to a superficial tumor with a degassed water coupling bolus in place. The theoretical plot shows variations in the field intensity similar to those observed experimentally. However, the experimental data consistently showed more uniform intensity profiles than predicted by theory. This is expected, since the theory does not include the effects of the damping of the elements that occur near their edges. The damping results from the clamping of the element's edges either by the epoxy holding the ceramic plate in the housing or by a non-driven adjacent element. This decreases the acoustical output of the elements near their edges which tends to smooth out the field intensity variations.

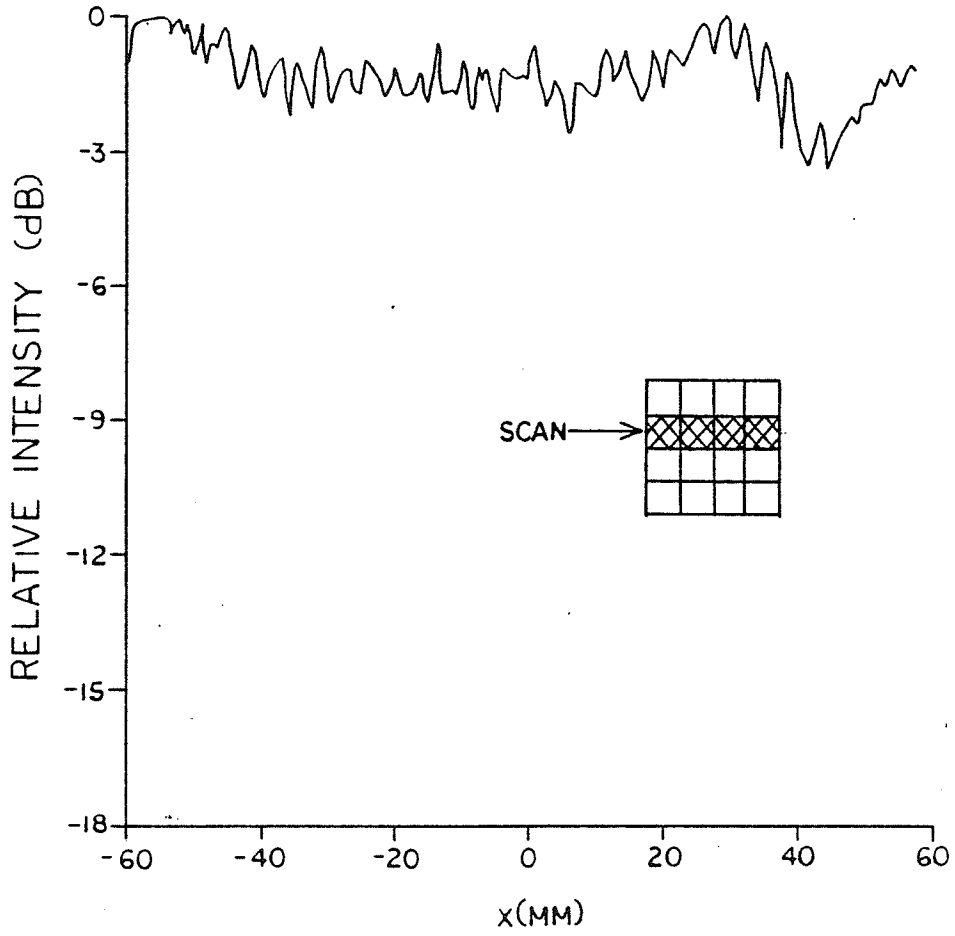

Figure 5.3. Relative field intensity of MET3 versus x position (z = 7.6 cm).

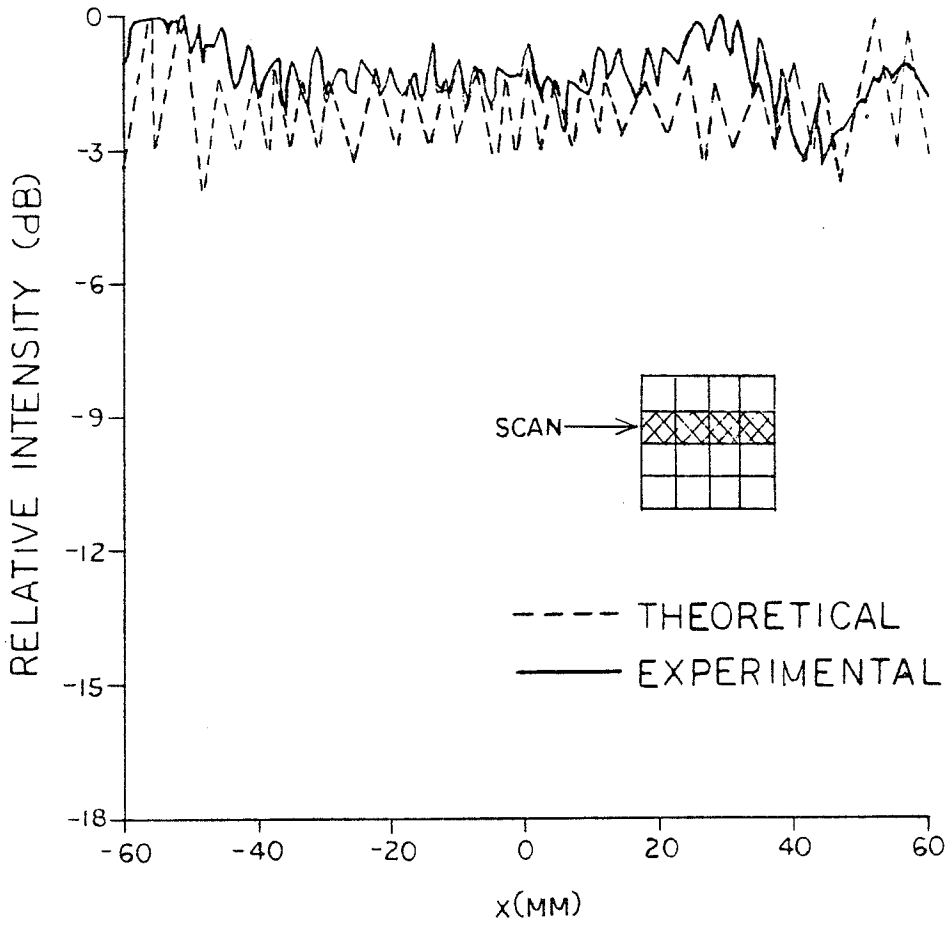

Figure 5.4. Comparison of the theoretical and experimental relative field intensity of MET3, with four adjacent elements excited, versus x position (z = 76 mm).

5.2 Acoustical Power Output

The acoustical power output of several of the elements of MET3 was measured using the reflecting radiation force target. Figure 5.5 shows a typical acoustical power output versus the input electrical power for one of these elements. The average efficiency of the elements was determined from this plot to be approximately 89%, and thus approximately 11% of the input power is lost in the ceramic. The temperature rise measured at the back surface of an element versus the power lost in that element is plotted in Fig. 5.6. The power lost in the element was calculated as 11% of the input electrical power. The measured temperature rise, T_R, was approximately linearly proportional to the power dissipated in the ceramic, P_d, and can be expressed as

$$T_R = 1.2P_d \quad (^oC) \tag{5.1}$$

Using Eq. (5.1), the heat transfer coefficient, h, in Eq. (2.7) can be determined. For a water temperature of 23.3°C and a ceramic thickness of 0.2 cm, h is approximately 0.0132 cal/cm^2/s. Using this value of h, the temperature at the center of the ceramic with an acoustical power output of 150 W can be determined from Eq. (2.7) to be 38.9°C. From Fig. 2.5, a temperature of 38.9°C would not significantly affect the Q_m of the ceramic.

5.3 Non-perfused Tissue Heating

Initial tests of tissue heating with MET3 were conducted with thermocouples embedded at depths of 3, 10, and 30 mm in a non-perfused, *in vitro* sample of pig heart muscle. The surface of the tissue was 7.6 cm from the face of the transducer, positioned

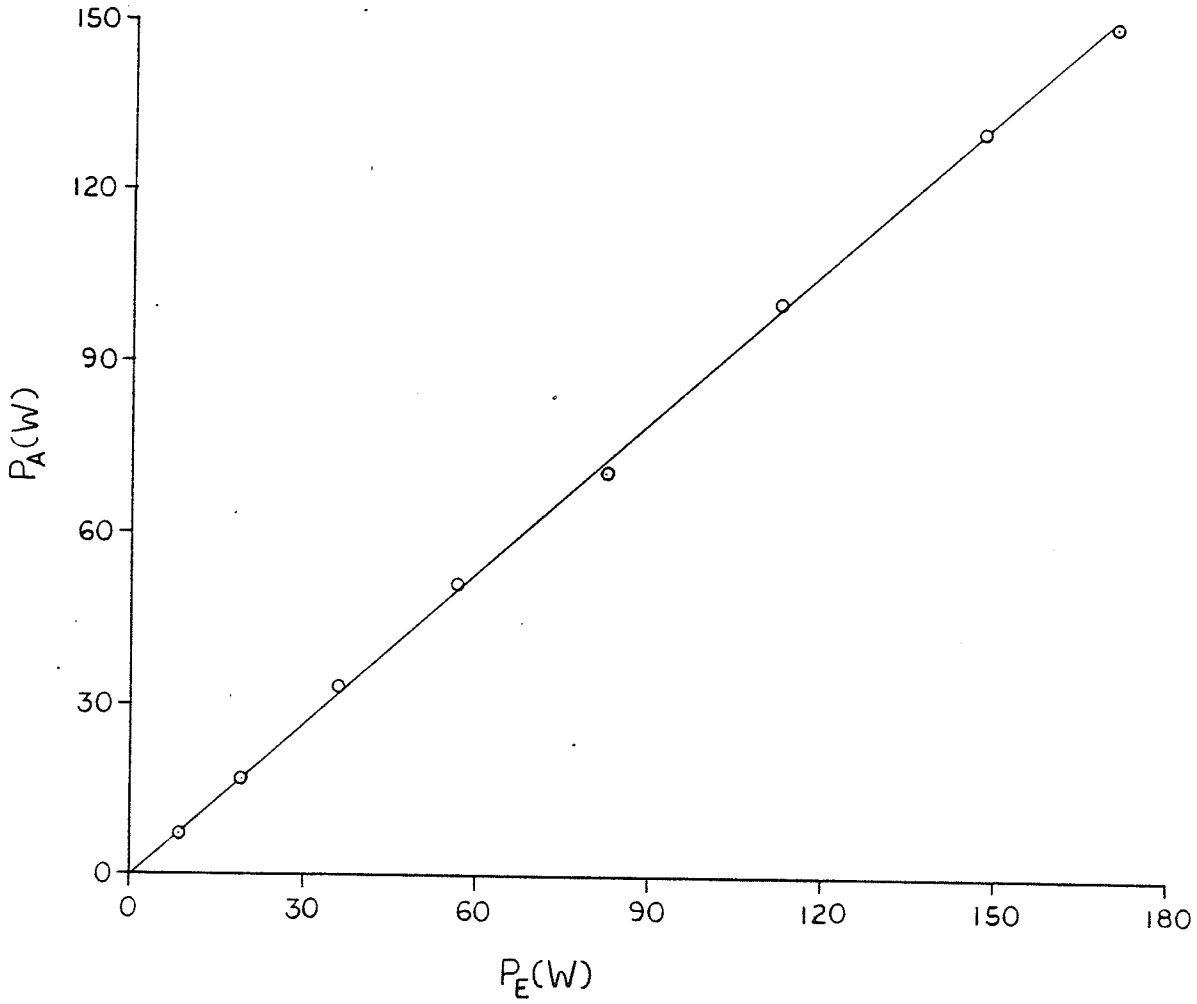

Figure 5.5. Acoustical power output, P_A, versus electrical power input, P_E, for an element of MET3.

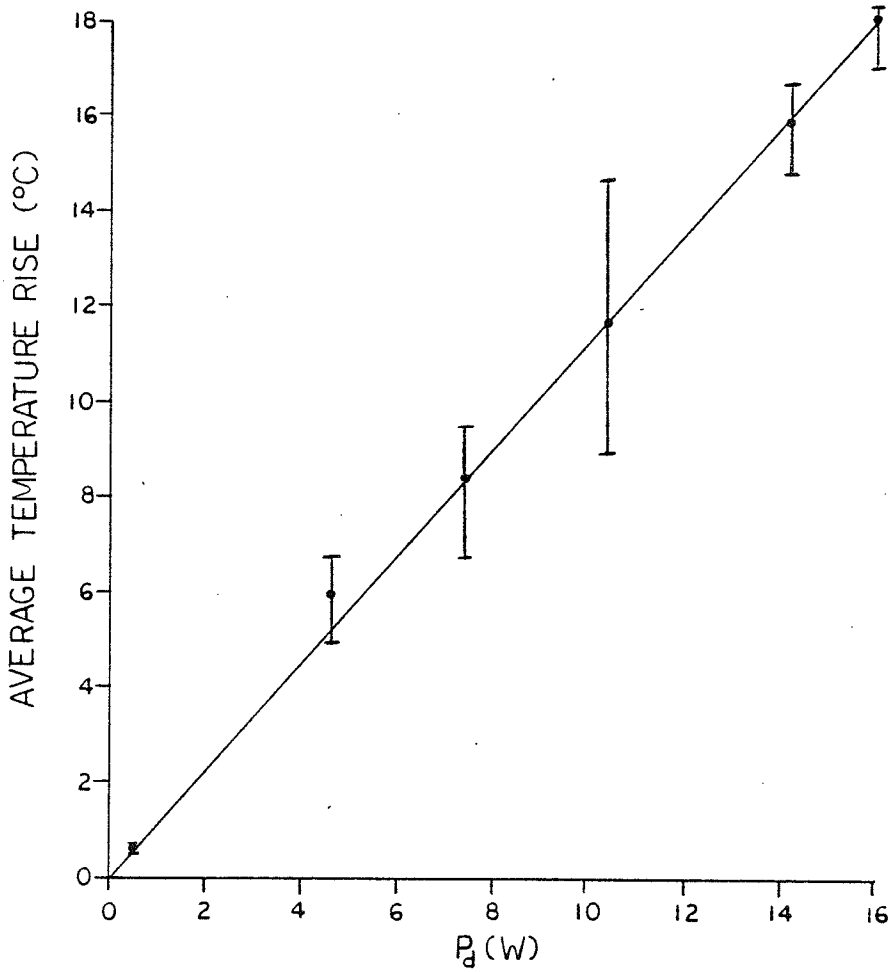

Figure 5.6. Average temperature rise versus the power dissipated, P_d, in an element of MET3.

such that the thermocouples were in the center of the transverse field of the active elements. The temperature rise was determined as a function of time with one element excited ($I = 2.9\ W/cm^2$), as shown in Fig. 5.7. The initial temperature rise at the 10 mm and 30 mm depths were $7.6^{o}C$/min and $4.1^{o}C$/min, respectively. Assuming an attenuation coefficient of 0.13 Np/cm, and that the heating rate is directly proportional to intensity, a 42% decrease in the heating rate can be expected at the 30 mm depth relative to the 10 mm depth. This agrees well with the measured 46% decrease in heating rate. These results showed that the transducer was capable of producing significant temperature rises in this tissue well beyond those necessary for hyperthermia. However, perfusion must be considered when assessing the heating capabilities of a hyperthermia transducer.

5.4 Perfused Phantom Heating

The effect of perfusion rate on the temperature rise versus time response of the perfused kidney is shown in Fig. 5.8. The perfusion rates were 0, 1.1 and 2.2 ml/min/g. As expected, an increase in perfusion resulted in a decrease in both the initial rate of temperature increase and the steady state temperature within the phantom. Figure 5.9 is a comparison of the temperature rise versus time response at three different depths. The temperature at the 3 mm depth was consistently lower than at the greater depths. This was likely due to a combination of two factors: (1) greater heat loss by conduction to the nearby surface; and (2) greater perfusion in the kidney cortex relative to the medulla [41]. With an estimated attenuation coefficient of

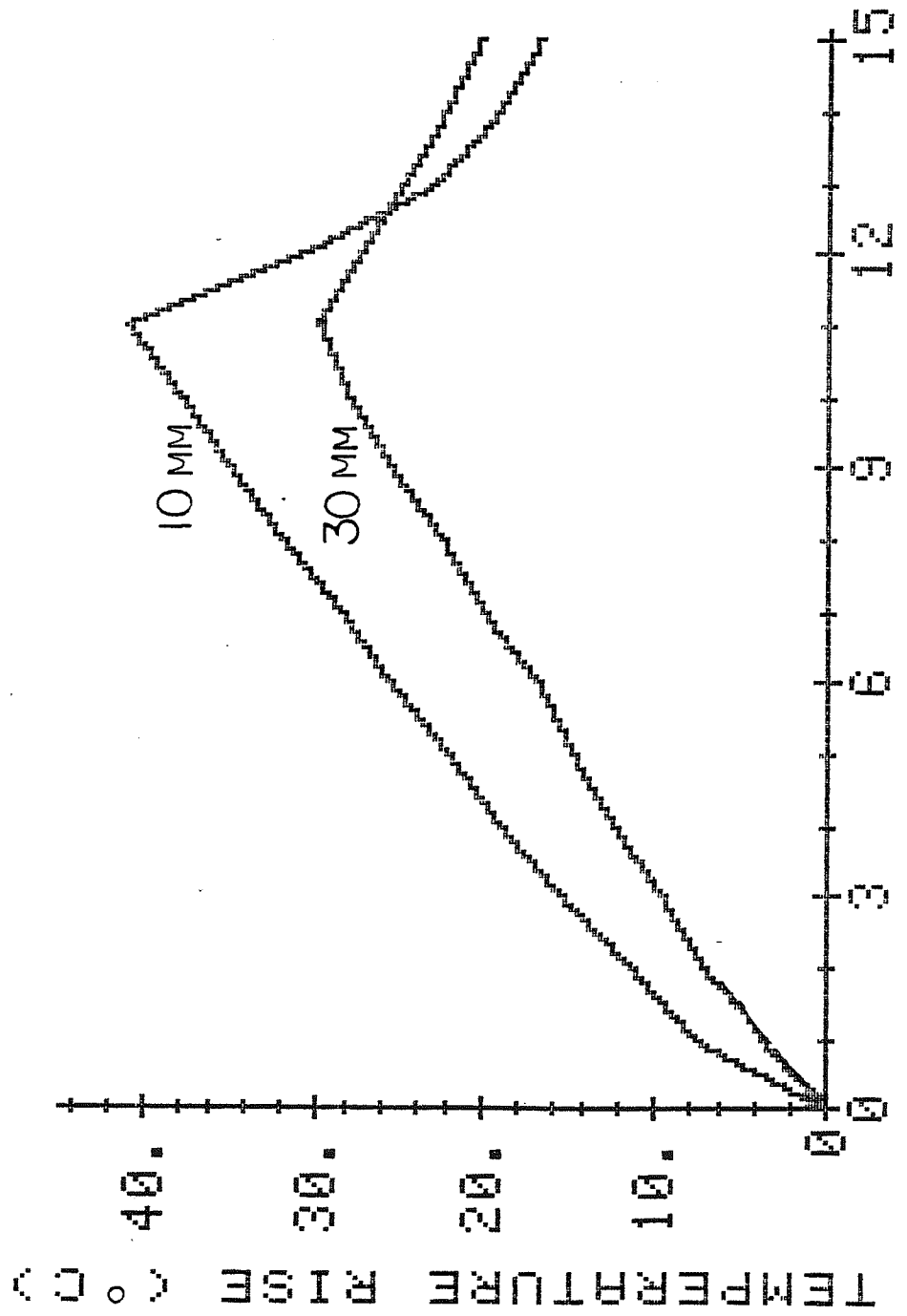

Figure 5.7. Temperature rise versus time in the pig heart at depths of 10 and 30 mm (I_o = 2.9 W/cm^2).

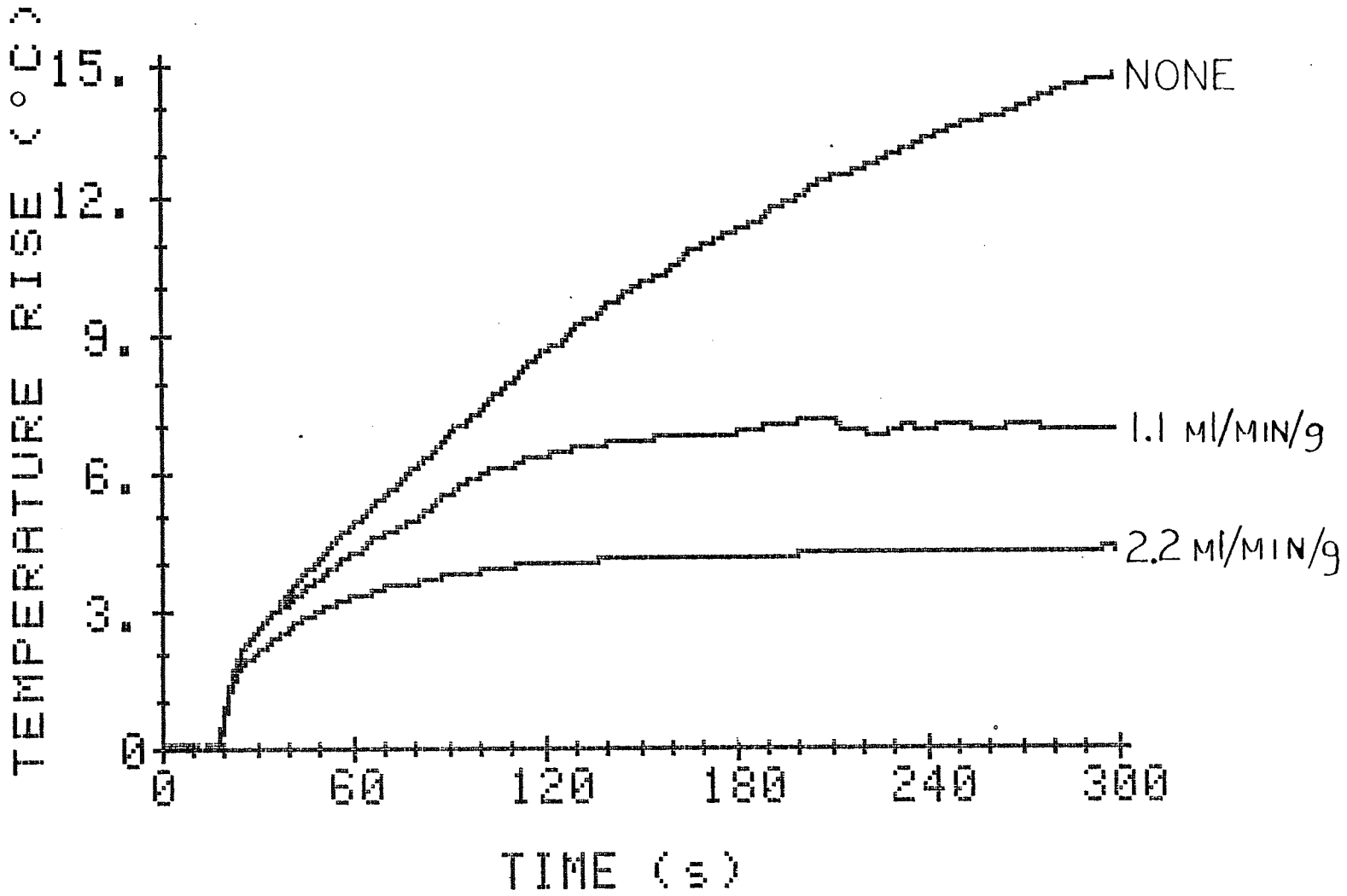

Figure 5.8. Temperature rise versus time in the pig kidney, at a depth of 11 mm, with perfusion rates of 0, 1.1, and 2.2 ml/min/g (I_o = 4.5 W/cm^2).

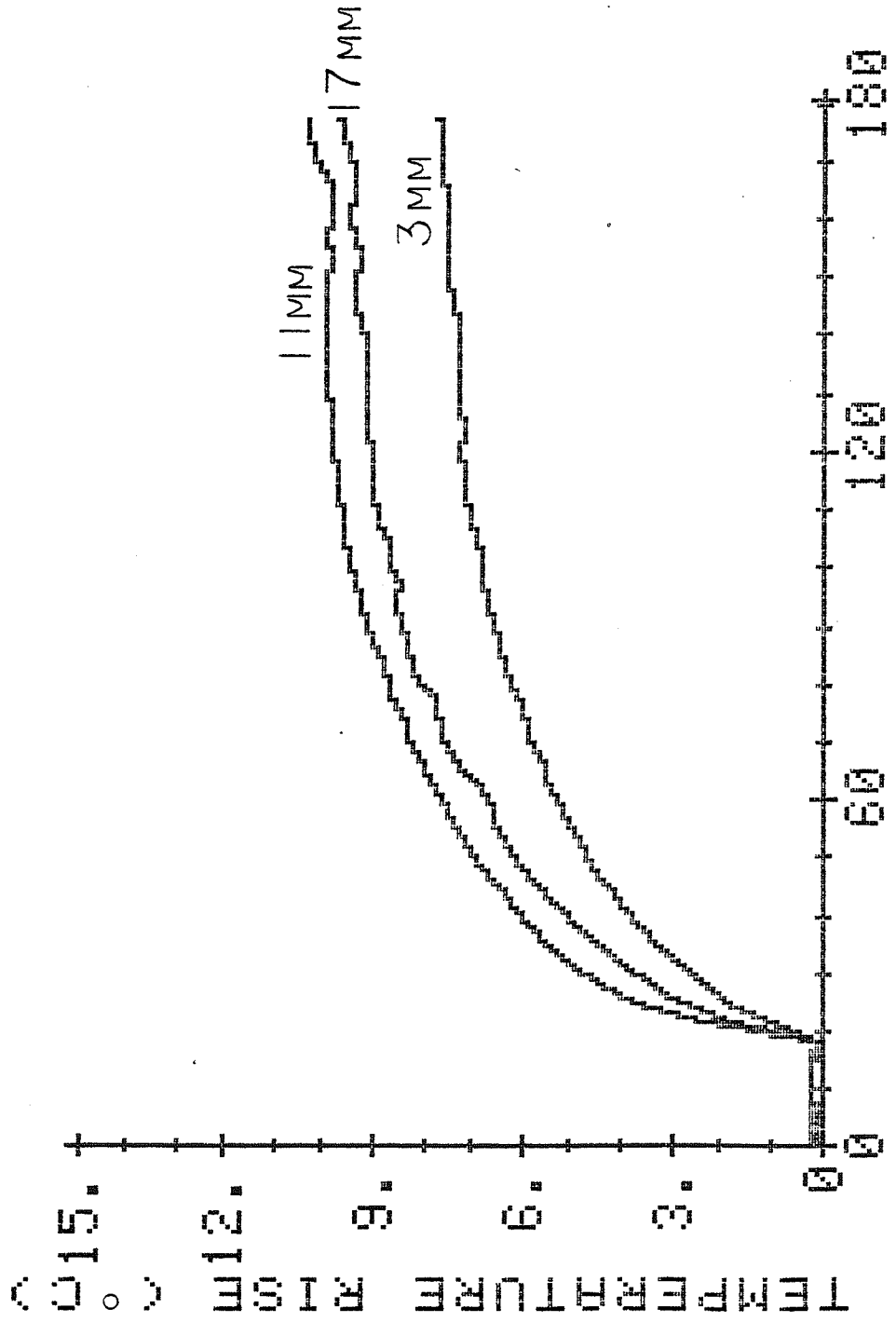

Figure 5.9. Temperature rise versus time in the pig kidney at depths of 3, 11, and 17 mm, with a perfusion rate of 1.1 ml/min/g (I_o = 9 W/cm^2).

0.07 Np/cm, approximately half that found in freshly excised tissue (see Section 4.6), an increase in depth from 11 to 17 mm would result in a decrease in intensity of 8%. This is consistent with the approximately 10% decrease in the initial rate of temperature rise at the 17 mm depth relative to the 11 mm depth.

Figure 5.10 shows the effect of perfusion rate on the temperature rise versus time response of the perfused liver. Once again, as for the kidney, an increase in the perfusion rate results in a decrease in both the rate of temperature increase, and the steady state temperature within the liver. Figure 5.11 is a comparison of the temperature rise versus time response at three different depths with no perfusion. The effects of surface conduction are highlighted by the more rapid decrease in temperature at the 5 mm depth, after the power was turned off, relative to the deeper thermocouples. Figure 5.12 shows the temperature rise versus time response for the same three thermocouple positions as in Fig. 5.11 except with a perfusion rate of 0.6 ml/min/g. The temperature at the 15 mm depth was consistently lower than the temperature at the 26 mm depth. This was most likely a result of the thermocouple at the 15 mm depth being in an area of greater perfusion than the 26 mm depth thermocouple. Therefore, even though the liver is more evenly perfused and homogeneous than the kidney, there appear to be locations within the liver with substantially higher perfusion than other locations.

5.5 Discussion

The field intensity measurements, with four adjacent

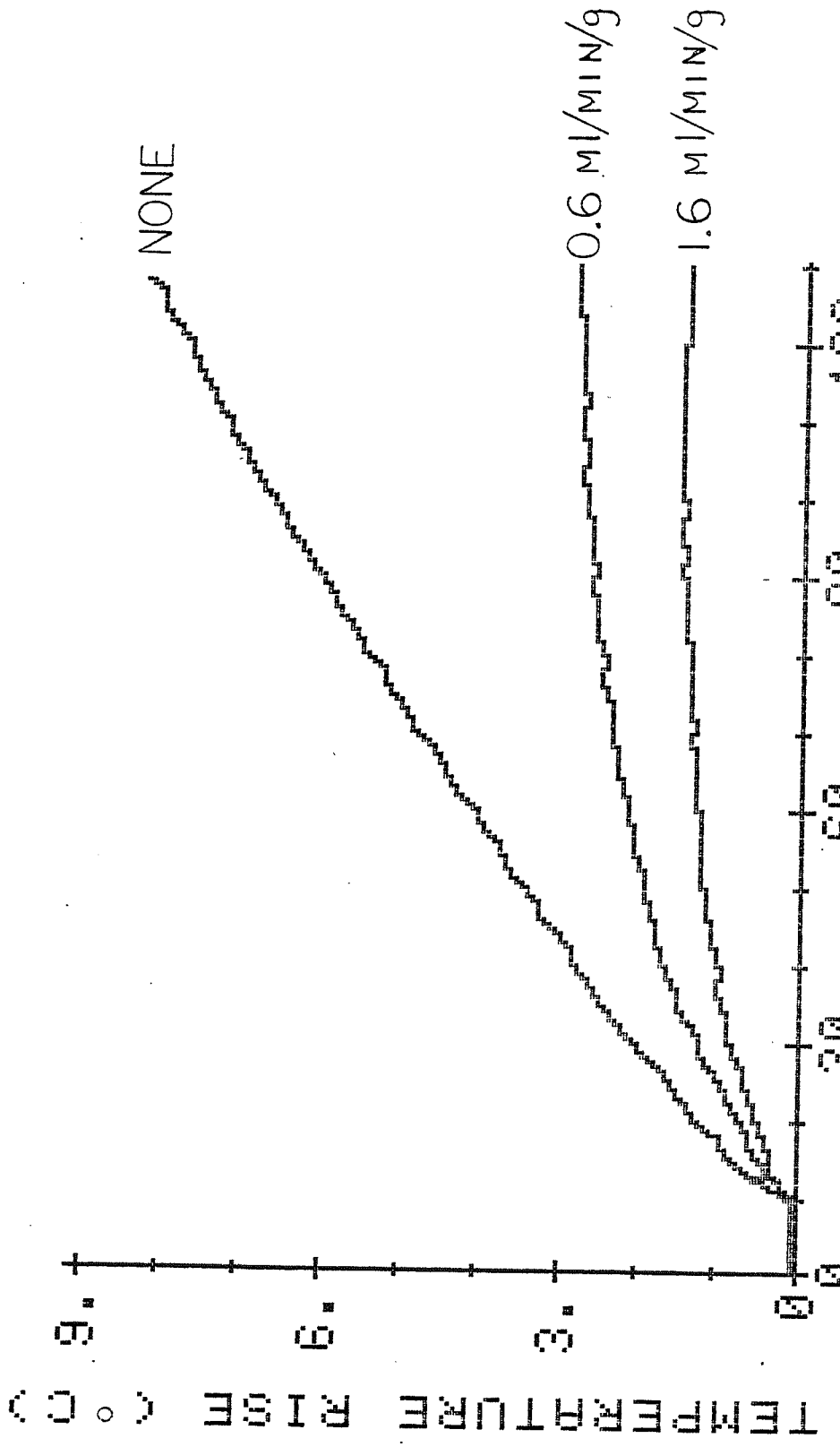

Figure 5.10. Temperature rise versus time in the pig liver, at a depth of 26 mm, with perfusion rates of 0, 0.6, and 1.6 ml/min/g (I_o = 9 W/cm^2).

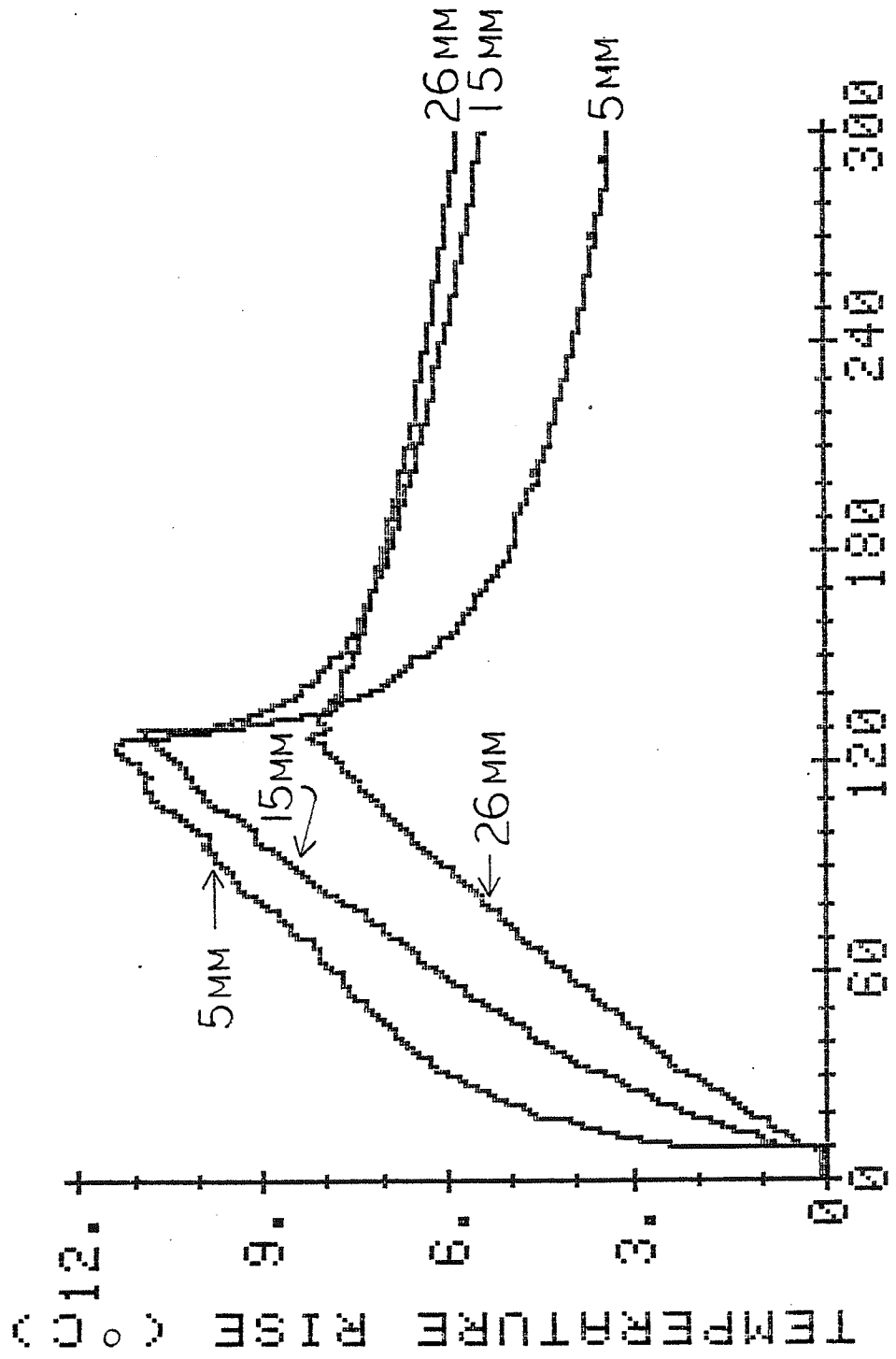

Figure 5.11. Temperature rise versus time in the pig liver, at depths of 5, 15, and 26 mm, with no perfusion (I_o = 9 W/cm^2).

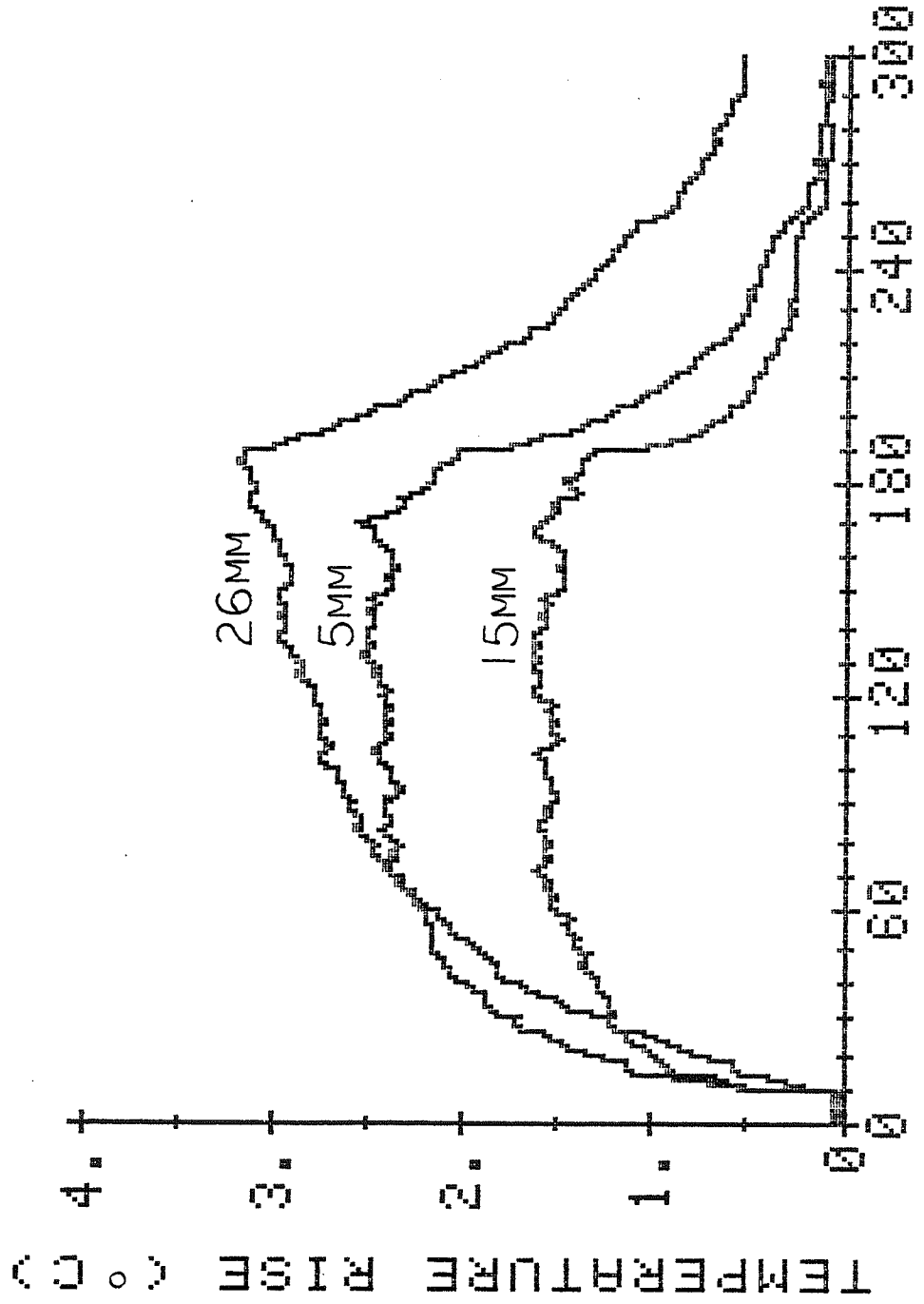

Figure 5.12. Temperature rise versus time in the pig liver, at depths of 5, 15, and 26 mm, with a perfusion rate of 0.6 ml/min/g (I_o = 4.8 W/cm^2).

transducer elements excited, show a relatively uniform intensity over a transverse plane. It has been shown that the variation in output among elements can be made very small, such that the transverse field is even more uniform than is shown here [42]. The transducer is capable of producing acoustical power as high as 150 W per element, although results from the tissue heating experiments suggest that perhaps only 40 W per element will be sufficient for hyperthermia applications. Data from the heating of an *in vitro* non-perfused pig heart muscle show that the transducer is capable of producing temperature rises in excised non-perfused tissue of up to 40°C. This is about five times the temperature rise that is typically required for hyperthermic treatment. However, since there was no perfusion present to provide convective cooling of the tissue, these temperature rises were not surprising.

The importance of considering perfusion when evaluating the performance of the transducer was demonstrated through the use of the perfused tissue phantoms. The transducer was shown to produce only modest temperature rises of 4 to 7°C in the presence of perfusion rates comparable to those that could be found in some tumors. However, the alcohol fixation procedure reduced the absorption coefficient of the kidney by approximately a factor of two. Therefore, greater temperature rises for the same incident intensity can be expected in tumor tissues which normally have attenuation coefficients larger than the fixed kidney.

The transducer has been packaged as a part of a commercial hyperthermia system which is undergoing clinical tests on animals. Results of studies on *in vivo* heating of thigh muscles of 12 dogs

indicate that time-averaged intensities of approximately 0.4 to 1.5 W/cm^2 were necessary to maintain temperatures between 43°C and 44°C at a depth of 1 cm [42]. The tests conducted as a part of this dissertation research indicate that the transducer is capable of producing intensities at least a factor of seven greater than these.

CHAPTER 6

EXPERIMENTAL TESTS OF THE TAPERED PHASED ARRAY TRANSDUCERS

6.1 Comparison of Experimental and Theoretical Field Intensity Distributions

Figure 6.1 shows the theoretical and experimental plots of the field intensity distributions of the 16-element untapered linear array with grooves between the elements cut to a depth of 75% of the total thickness of the ceramic. There are lobes present in the experimental plot that are not predicted by theory and, in one instance, only 6 dB below the focused main lobe. These additional lobes were due primarily to interelement coupling of -16.7 dB as measured by exciting one element of the array and recording the voltage appearing on an adjacent element. With coupling present, the radiation pattern of the array is a sum of two radiation patterns: the designed pattern and the pattern due to the interelement coupling [30]. The coupling effectively increases the width of the elements, thus, reducing the spacing between the main lobe and the first grating lobe [23]. One approach to reducing the coupling is to increase the depth of the cuts to greater than 75%. However, the resulting plate would be very fragile and would still exhibit some coupling.

The theoretical field intensity distributions for the tapered phased arrays were calculated using the computer model discussed in Section 3.4. Figures 6.2 through 6.4 show comparisons of the theoretical ($Q_m = 15$) and experimental field intensity distributions at 600 kHz in the x, y, and z directions, respectively, for TPA1 with 16 elements excited. The theoretical

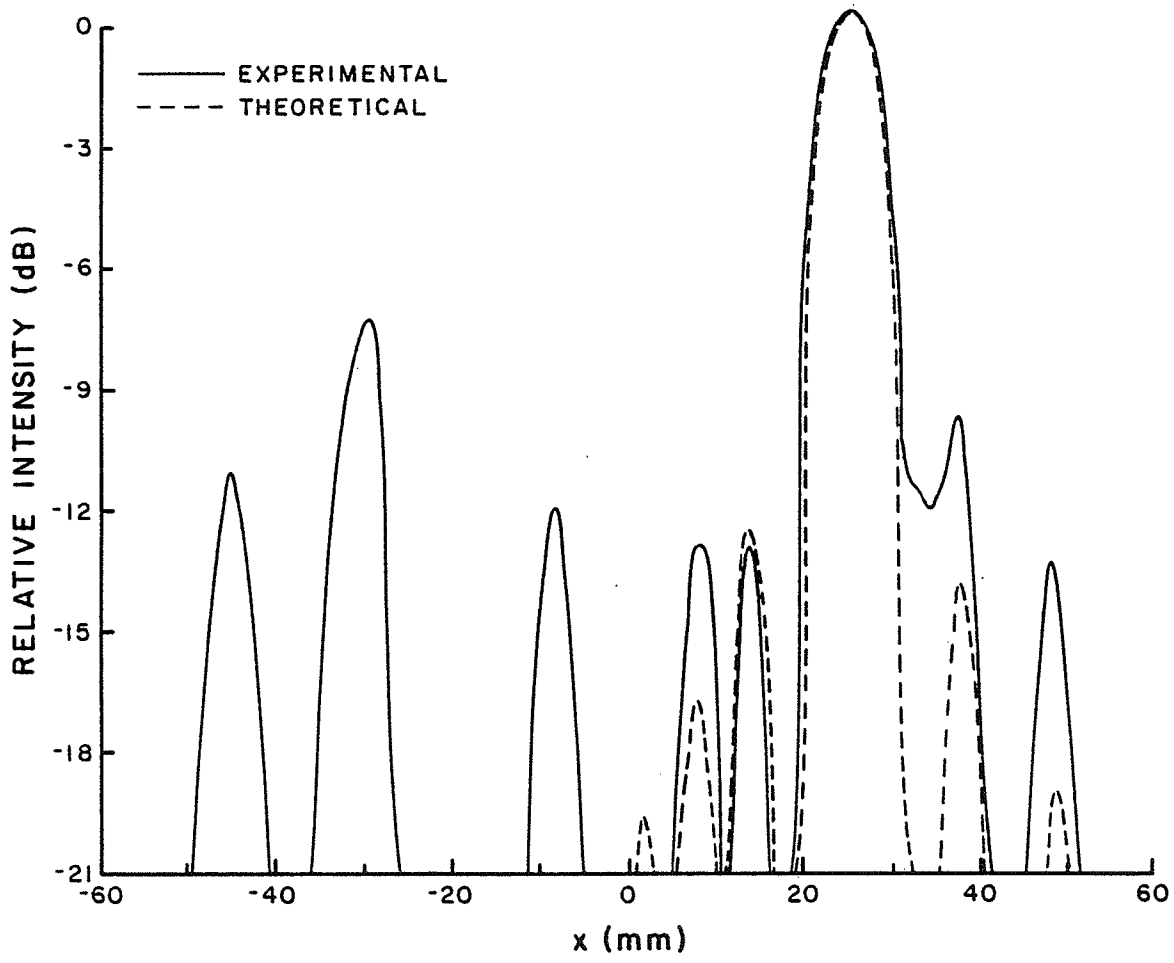

Figure 6.1. Comparison of the theoretical and experimental relative field intensity of the linear phased array, with a 75% cut depth, versus x position (Focus = (26,0,100 mm), y = 0, z = 100 mm, f = 473 kHz).

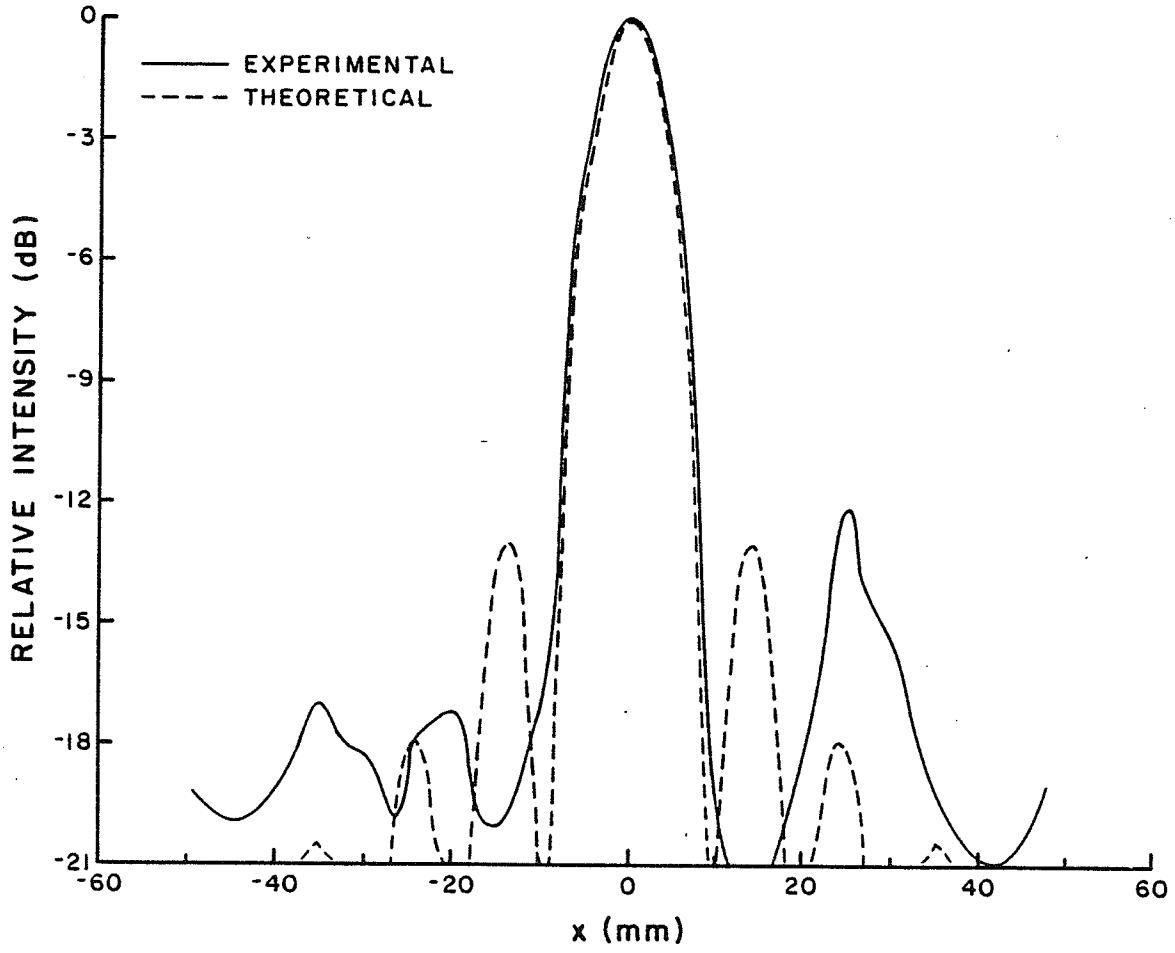

Figure 6.2. Comparison of the theoretical and experimental relative field intensity of TPAl versus x position (Focus = (0,0,100 mm), y = 0, z = 100 mm, f = 600 kHz).

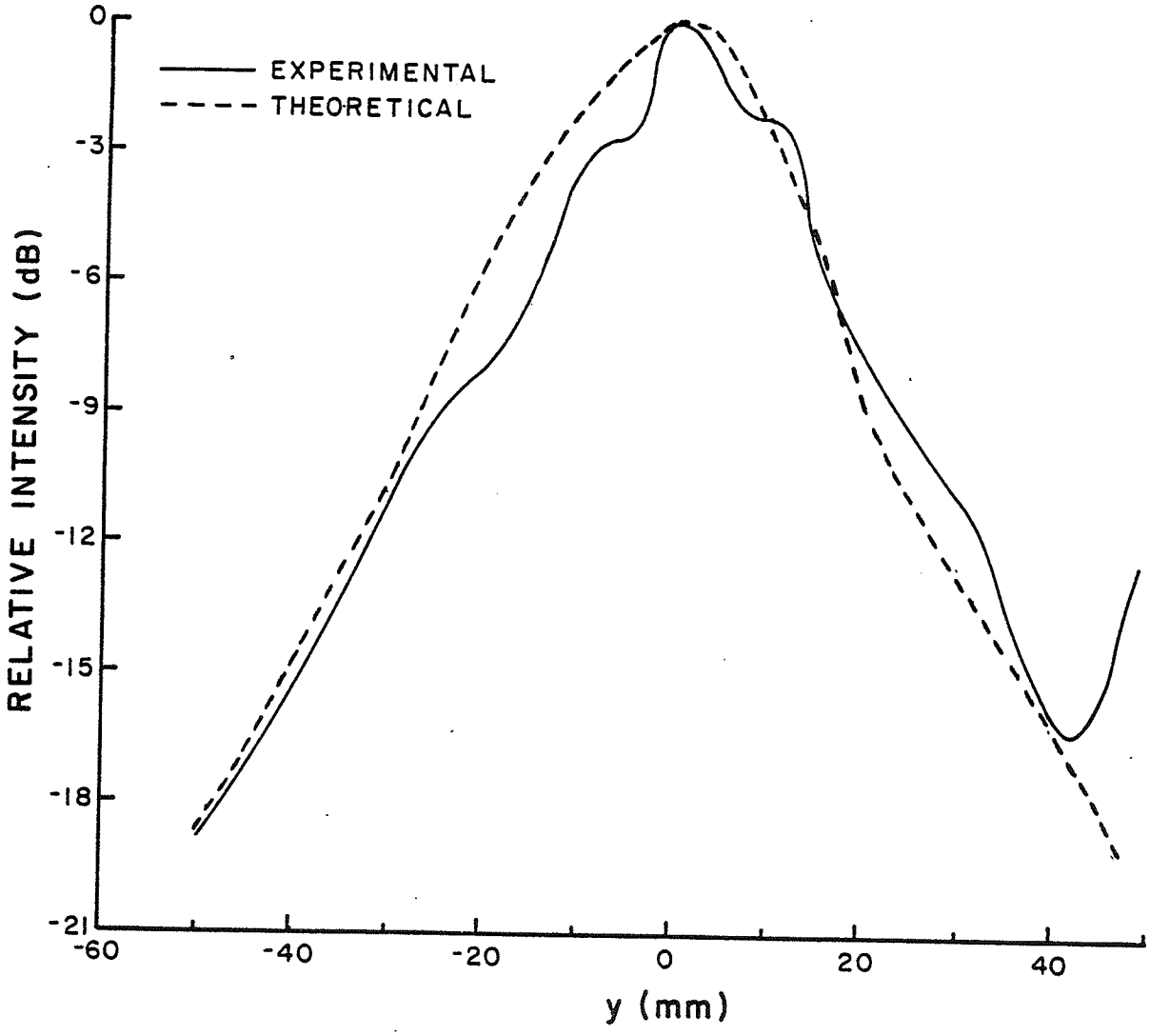

Figure 6.3. Comparison of the theoretical and experimental relative field intensity of TPA1 versus y position (Focus = (0,0,100 mm), x = 0, z = 100 mm, f = 600 kHz).

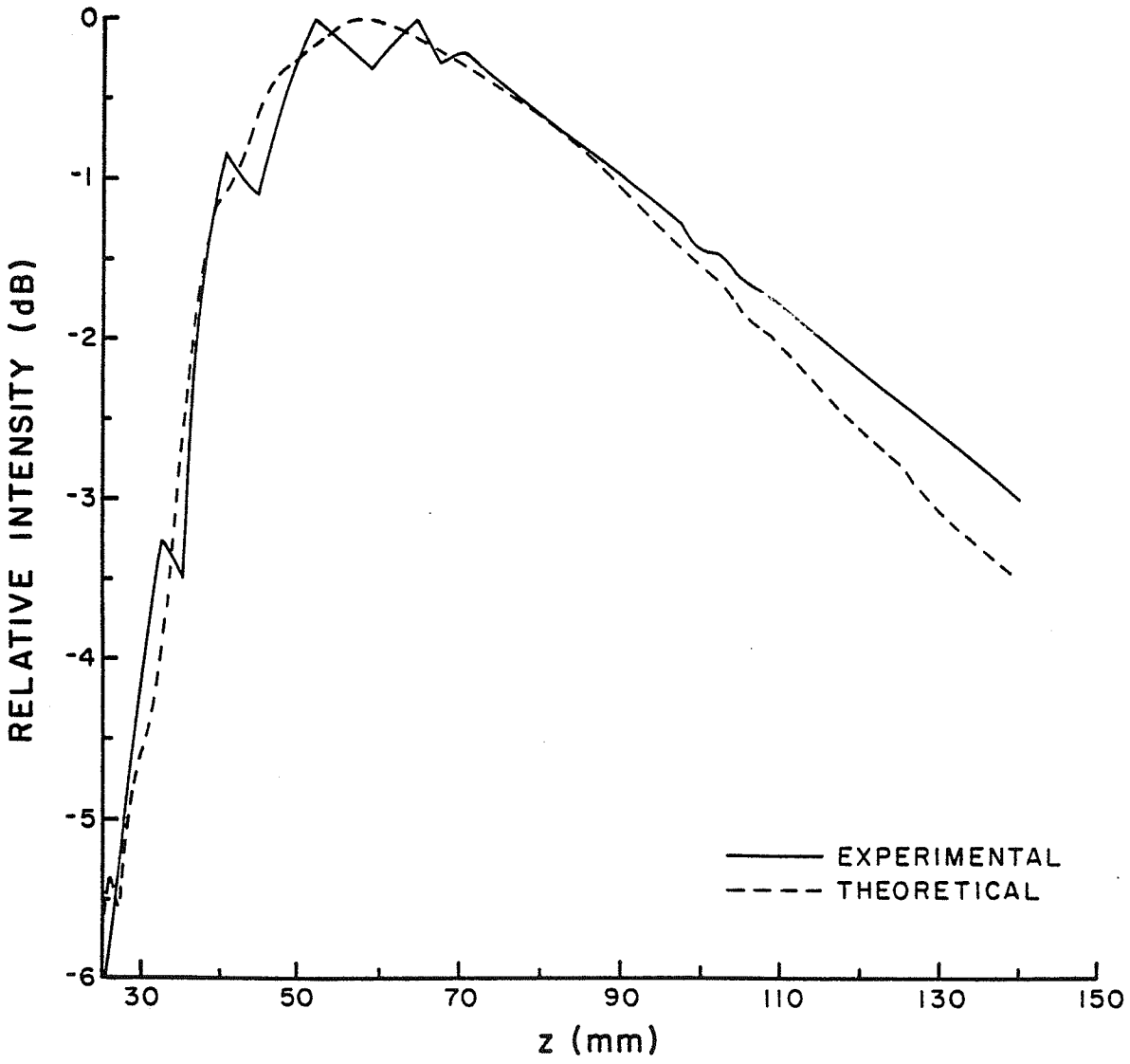

Figure 6.4. Comparison of the theoretical and experimental relative field intensity of TPA1 versus z position (Focus = (0,0,100 mm), x = y = 0, f = 600 kHz).

and experimental field profiles were plotted as relative intensity versus position. These figures show good agreement between the theoretical predictions and the experimental data for the focused lobe. The differences in the side lobe intensities are attributed to the variations in output of the elements due to their impedance variations. There was typically a 15% variation in the magnitudes and a $\pm$ 5 degree variation in the phases of the element impedances for both TPA1 and TPA2. Since the impedance of an element is proportional to its width [32], the measured 10% variation in width of the elements would seem to account for most of the impedance variation. Variations in properties of the ceramic material such as density, speed of sound, and polarization will also contribute to the impedance variations. The variation in the magnitudes of the impedances would result in an approximately 15% variation in the acoustical power outputs of the elements assuming each were driven by the same voltage. In linear arrays manufactured for imaging, such variations in sensitivity (power output) and delay errors (phase errors) cause the side lobes to increase in number and amplitude, and to be asymmetrical [43]. The main lobe, however, is not significantly influenced. The acoustical coupling between elements (completely separate) of the array was measured to be -32.6 dB, a 15.9 dB improvement over the coupling in the array with grooves cut to a depth of 75%. Only 16 of the elements in TPA1 could be used because several of the elements had been damaged by contact with the hydrophone probe. With only 16 usable elements, little additional useful data could be obtained from this array. Therefore, the rest of this chapter will be concerned with results from studies of TPA2.

Figures 6.5 and 6.6 show comparisons of experimental and theoretical field profiles of TPA2 in the x direction, at 650 kHz for the focus on axis (x = 0) and the focus steered off axis by 2.5 cm, respectively. Figure 6.7 is a comparison of the experimental and theoretical profiles in the z direction for TPA2 with the same focal location as in Fig. 6.5. These three figures show that there is good agreement between the theoretically predicted fields and the experimental data. As with the comparisons for TPA1, the differences between theoretical and experimental data for the side lobes are again attributed largely to impedance variations in the elements.

Figures 6.8 through 6.10 are comparisons of the intensity profiles in the y direction at 580, 620 and 650 kHz for TPA2. In comparing these three figures, it is clear that a frequency shift from 580 to 650 kHz moves the beam approximately 6 cm in the y direction. The theoretical predictions were based on a Q_m of 8 for the 580 and 620 kHz cases, and a Q_m of 11 for the 650 kHz case. The Q_m at 650 kHz was greater to simulate the damping from the clamped end of the element since its 3 dB region of excitation was at the very end of the elements. This clamping in effect caused a narrowing of the 3 dB beamwidth, which gave the appearance of an increase in Q_m of 3. The discrepancies between the theoretical and experimental profiles at 650 kHz (see Fig. 6.10) are attributed to this clamping effect.

A hydrophone probe was used to measure the phase shift in the acoustic wave produced along the height of an element. The probe was swept along the height of the element, 5 mm from its surface, and the resulting phase shift relative to the electrical signal

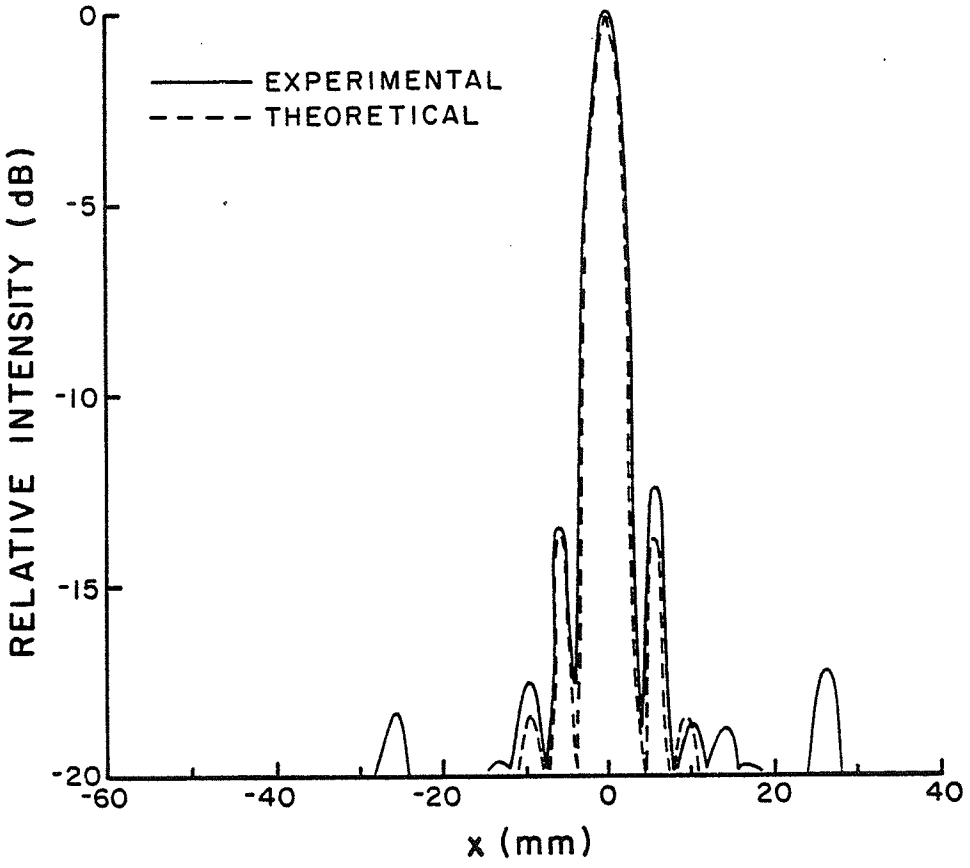

Figure 6.5. Comparison of the theoretical and experimental relative field intensity of TPA2 versus x position (Focus = (0,50,100 mm), y = 50 mm, z = 100 mm, f = 650 kHz).

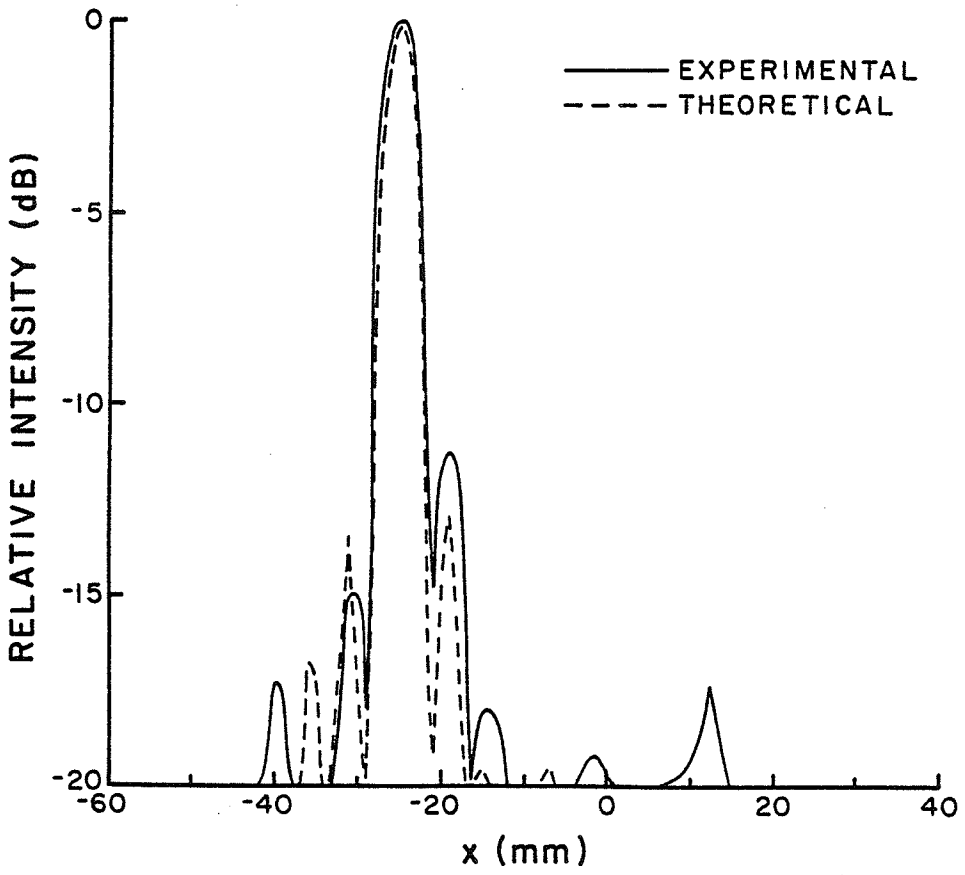

Figure 6.6. Comparison of the theoretical and experimental relative field intensity of TPA2 versus x position (Focus = (-25,50,100 mm), y = 50 mm, z = 100 mm, f = 650 kHz).

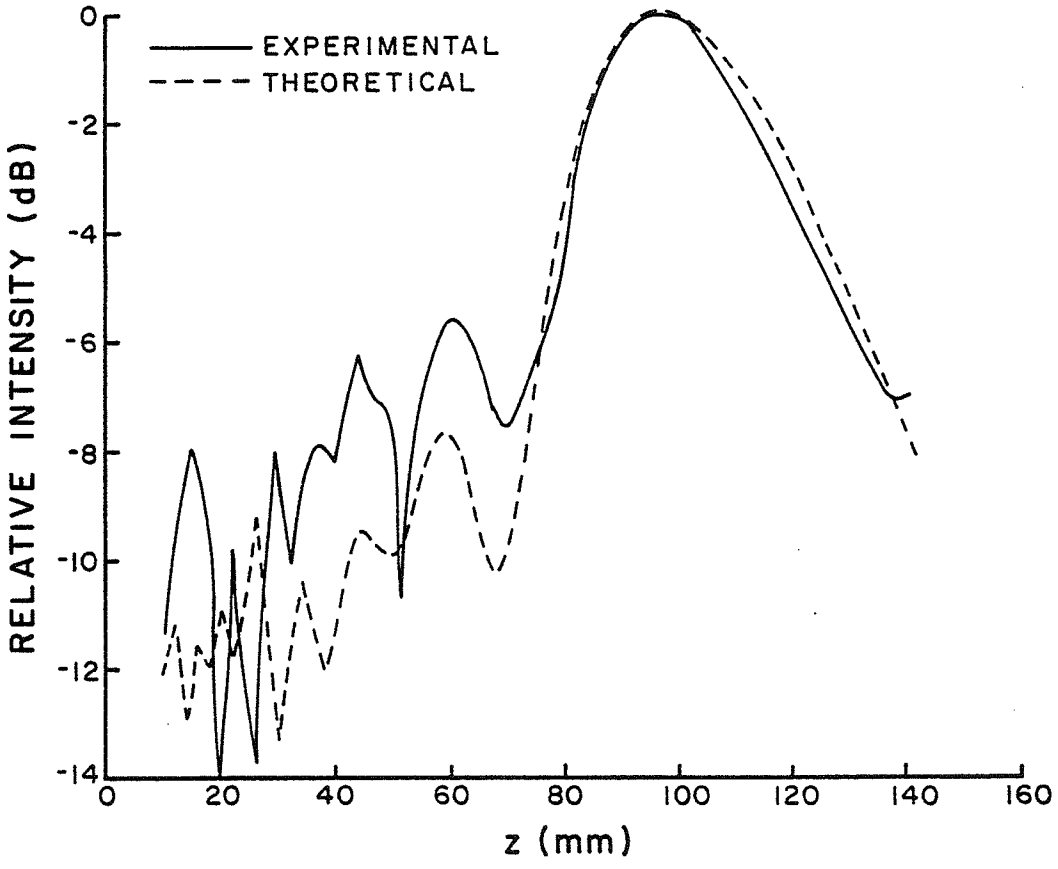

Figure 6.7. Comparison of the theoretical and experimental relative field intensity of TPA2 versus z position (Focus = (0,50,100 mm), x = 0, y = 50 mm, f = 650 kHz).

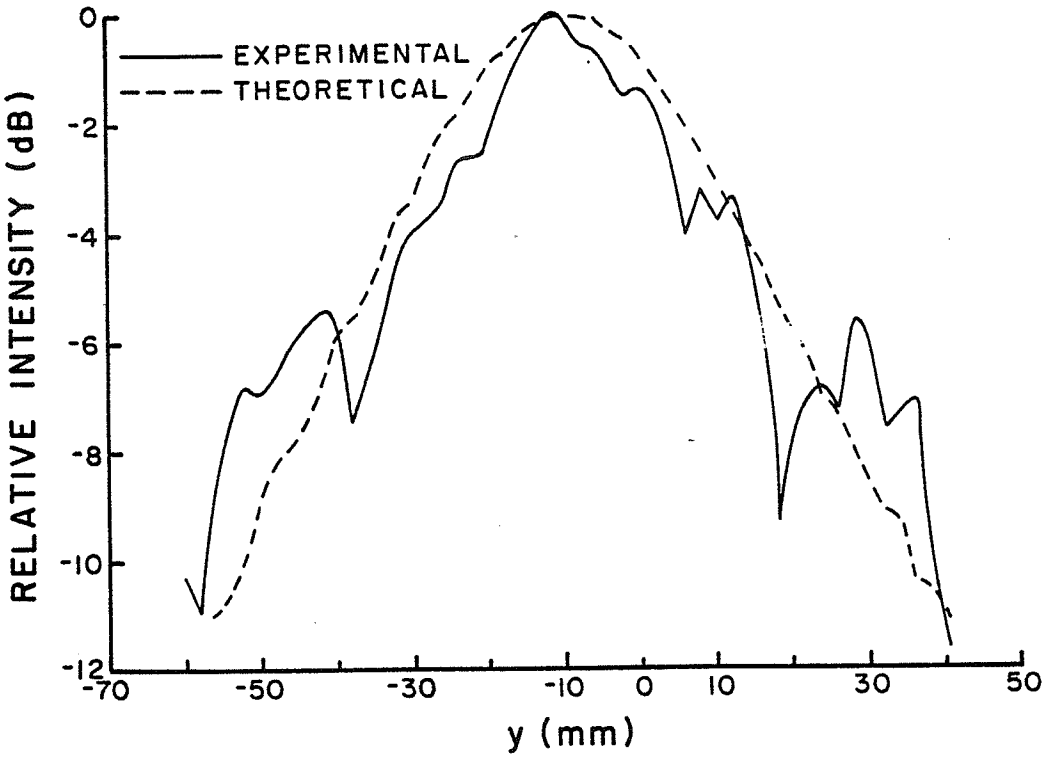

Figure 6.8. Comparison of the theoretical and experimental relative field intensity of TPA2 versus y position (Focus = (0,-10,100 mm), x = 0, z = 100 mm, f = 580 kHz).

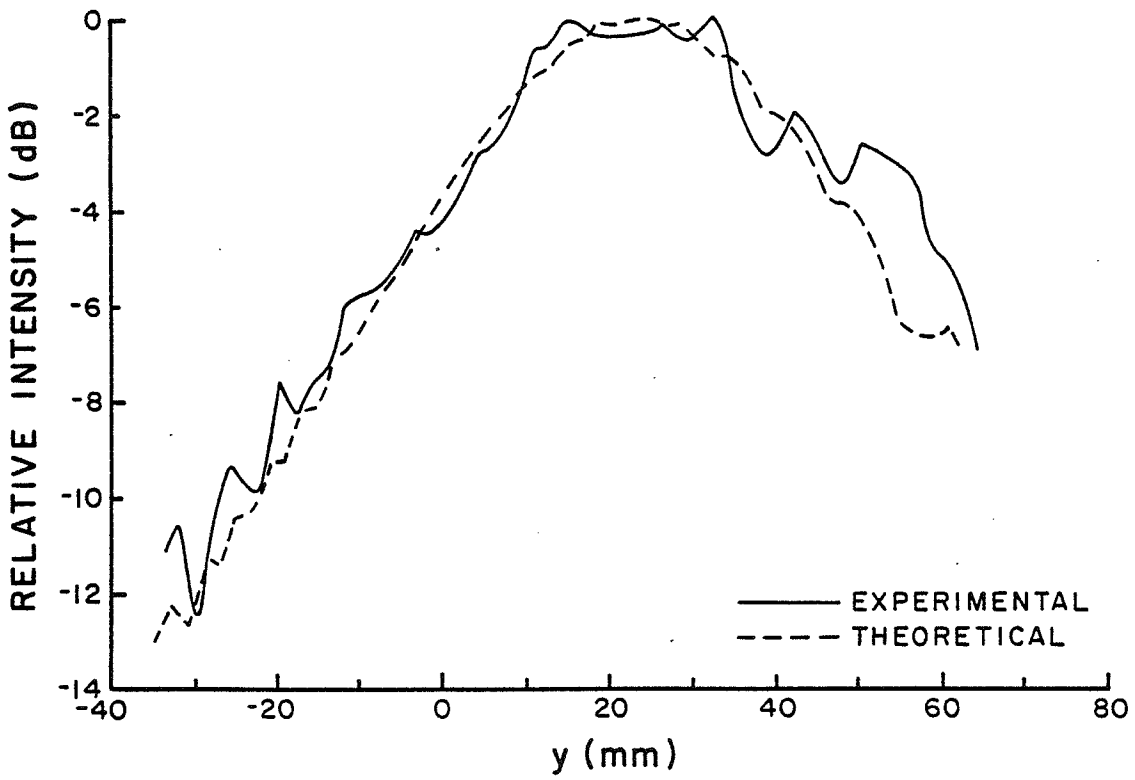

Figure 6.9. Comparison of the theoretical and experimental relative field intensity of TPA2 versus y position (Focus = (0,23,100 mm), x = 0, z = 100 mm, f = 620 kHz).

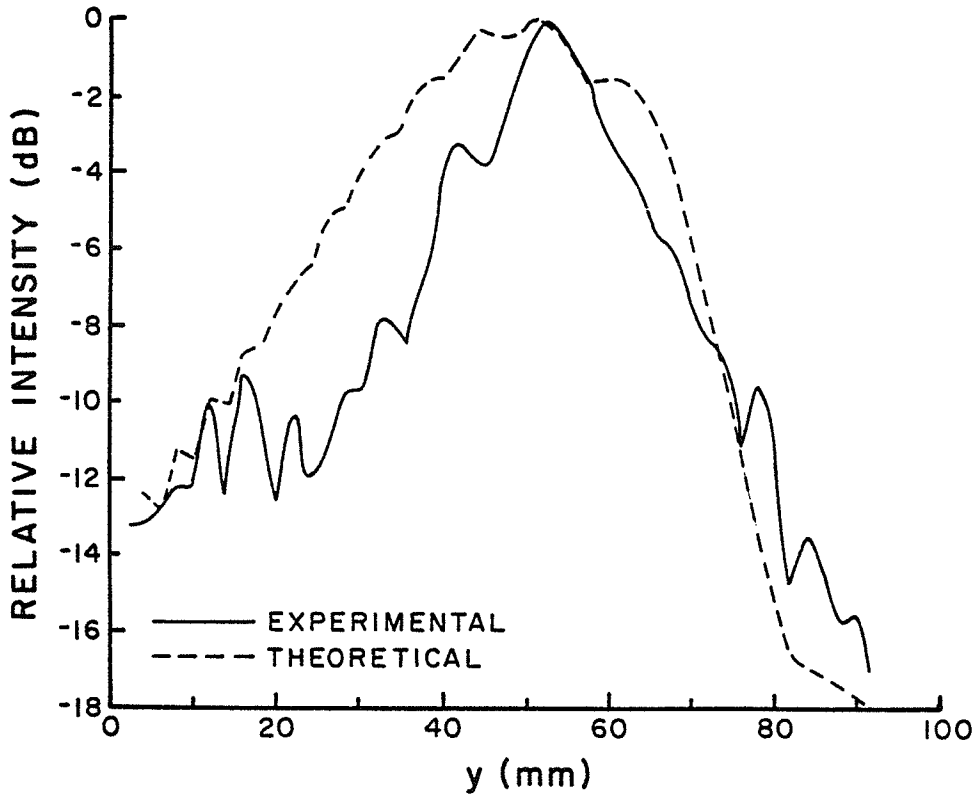

Figure 6.10. Comparison of the theoretical and experimental relative field intensity of TPA2 versus y position (Focus = (0,50,100 mm), x = 0, z = 100 mm, f = 650 kHz).

applied to that element was recorded. The experimental results are compared with the theoretical predictions in Fig 6.11 for a frequency of 630 kHz. This comparison shows that, within experimental error, there are some significant differences between the experimental data and the theoretical predictions. It appears that the simple model for the phase shift can be used for only rough approximations.

6.2 Acoustical Power Output

The acoustical power output of TPA2 was measured as a function of input electrical power using the radiation force target technique described in Section 4.1. Since the elements are narrow, their acoustical outputs are very nondirectional. Therefore, the radiation force target could not be used to measure the total acoustical power output from a single element. Instead, the efficiency of the array was determined by measuring the acoustical power in the focused main beam, with 32 elements excited, as a function of the input electrical power supplied to the amplifiers. Figure 6.12 shows the results for driving frequencies of 580, 620, and 650 kHz. The target was positioned at the focus of the array, set at (0, y, 100 mm), where the y position was determined by the driving frequency. The overall efficiency of the array and amplifiers was calculated from Fig. 6.12 to be approximately 28%. The small variations in efficiency (4%) with frequency can be attributed to the quality of the match between the electrical impedances of the elements and the amplifiers. These plots indicate that the acoustic output at the focus started to saturate at approximately 60 W at 650 kHz, 70 W

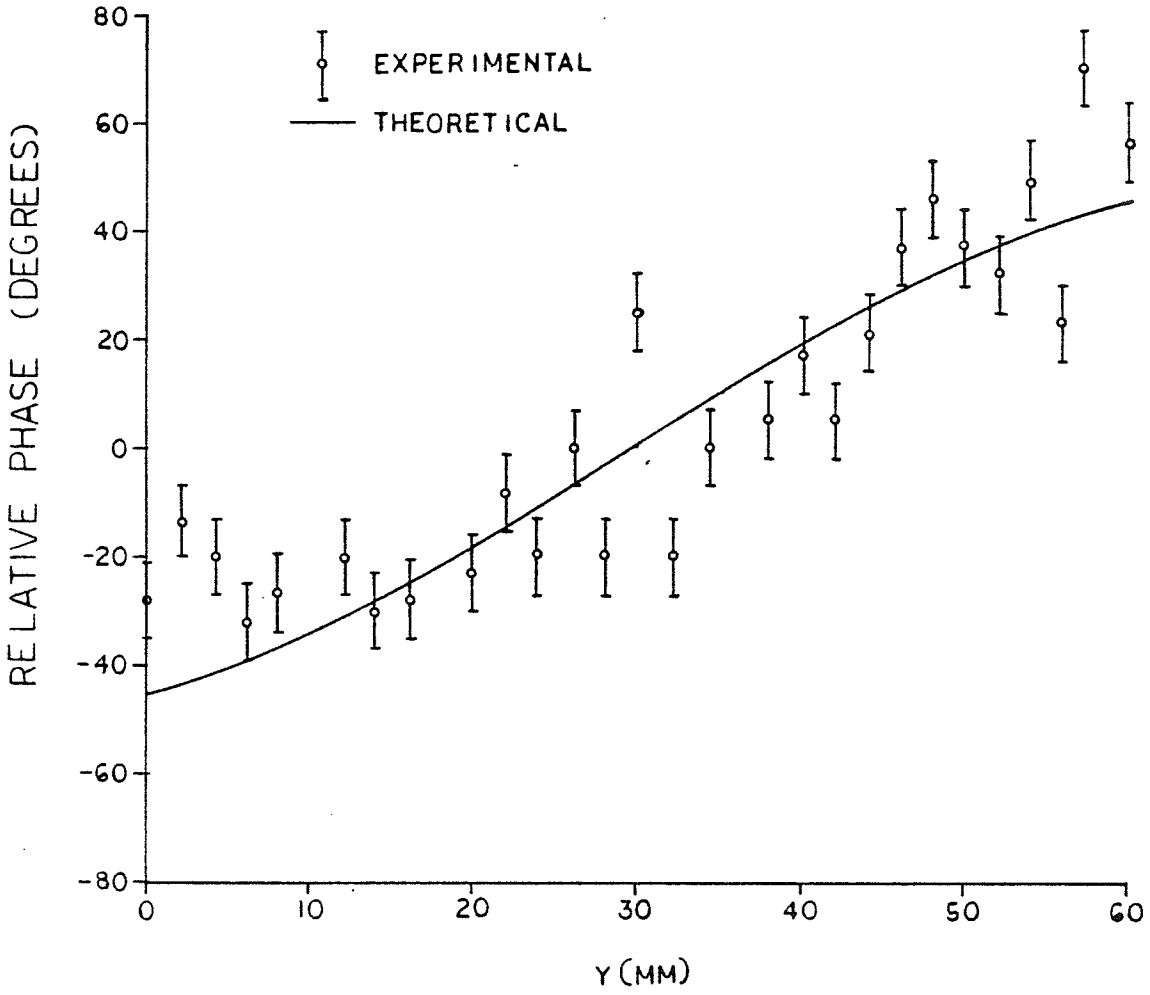

Figure 6.11. Comparison of the theoretical and experimental relative phase shifts in the acoustic wave, of an element of TPA2, versus y position.

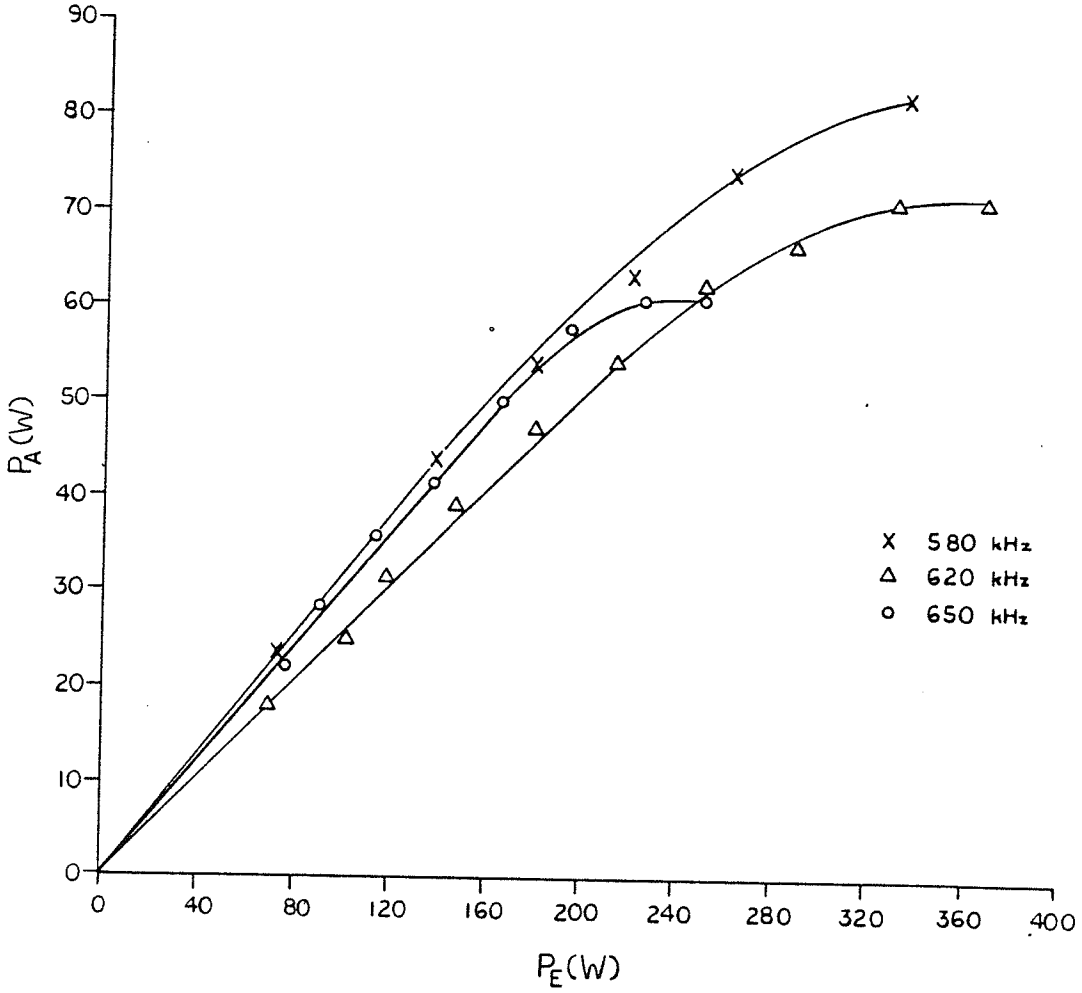

Figure 6.12. Acoustical power output of TPA2, P_A, versus electrical power input to the amplifiers, P_E.

at 620 kHz, and 80 W at 580 kHz. The observed increase in acoustical power output, at the start of the nonlinearity, with decreased frequency agrees with the theoretical analysis discussed in Section 2.4.

It was observed that when the nonlinearities began to occur, the current from the power supply (voltage regulated) and the corresponding acoustical power output decreased with time. This suggested that excessive heating in the elements due to internal losses was occurring and raising the temperature to a level where it had an effect on the output. Figure 6.13 shows the temperature rise recorded from three locations on the back of an element operating at 650 kHz versus input electrical power from the power supply. The thermocouples were located at y = 6 cm, the approximate location of the 650 kHz resonance, y = 0 and -6 cm. This indicates that the maximum temperature rise occurs along the resonant portion of the element as expected. At approximately 180 W input power, the temperature rise recorded by the thermocouple at y = 6 cm began to level off. This was attributed to a change in element impedance causing a greater impedance mismatch between the amplifier and the element. This impedance mismatch reduces the efficiency of the amplifier and results in delivery of less power to the element. The impedance, particularly the parallel capacitance C_o, of a piezoelectric ceramic is dependent on temperature [44]. When the nonlinearities at 650 kHz began to occur at approximately 200 W input power, Fig. 6.13 shows that the corresponding temperature along the resonant portion of the ceramic was at least 52°C. For a ceramic temperature of 52°C, Fig. 2.5 suggests that an approximately 10% decrease in Q_m, and

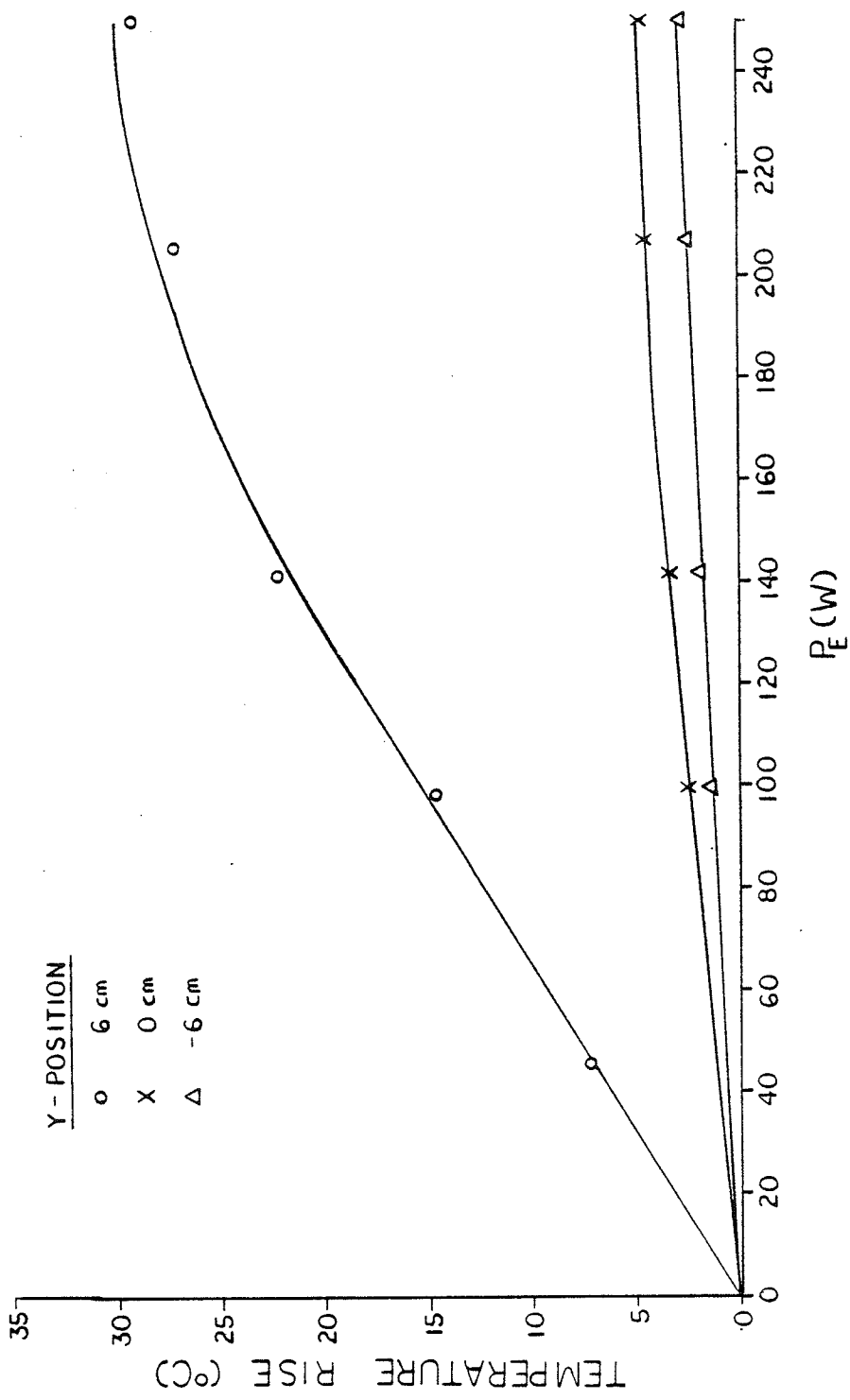

Figure 6.13. Temperature rise on the back of an element of TPA2, measured at three y positions, versus input electrical power to the amplifiers (f = 650 kHz).

therefore a 10% decrease in the acoustical power output can be expected. It is seen in Fig. 6.12 that the acoustic output at 200 W input is approximately 7% below that expected from a linear extrapolation of the output at lower powers. However, the temperature on the back of the ceramic would be higher than the average temperature in the ceramic since the water side will be cooler. Thus, based on the temperature data and the effect of temperature on the power output and impedance of the elements, it appears that the nonlinear response was due to decreased amplifier and element efficiencies.

The acoustical power output measurements were retaken with forced air cooling on the back of the elements. The cooling did not have a measurable effect on the acoustical power output of the array, which is consistent with the fact that most of the heat removal will be to the water, with or without cooling of the back surface.

6.3 Tissue Phantom Heating

The URI Therm-X tissue phantom was used to study the heating produced by the scanned focus of TPA2. The array controller was programmed to scan the focus in the x direction through 11 locations, spaced 5 mm apart, from x = -25 mm to x = 25 mm, every 1.4 ms. The focus in the z direction was positioned at a 5 cm depth in the phantom and aligned in the y direction with the four thermocouples used for temperature measurements (see Fig. 3.2 for coordinate orientations). The intensity at the focus was set at approximately 28 W/cm^2 yielding a time-averaged intensity of 2.5 W/cm^2. In order to prevent damage to the phantom, the maximum

time-averaged intensity was limited to 2.5 W/cm^2.

Figure 6.14 is a plot of temperature rise versus time for the four thermocouples during a two-minute heating period. Since there was no convenient method for cooling the phantom after heating, the exposures were limited to two minutes. Even with the limited intensity and time of exposure, 30 minutes were required for the phantom to cool to room temperature. The four thermocouples experienced temperature rises within 0.2^oC of each other. The fact that the 2 and 5 cm depth thermocouples showed almost identical temperature rises was due to the large focal dimension in the z direction (see Fig. 6.7). In this case, the size and positioning of the focus helped to overcome the decreased heating rate with depth.

6.4 Perfused Tissue Phantom Heating

The perfused kidney phantom was also used to measure the heating produced by TPA2 with the focus scanned. The array controller scanned the focus in the x direction through five locations, spaced 5 mm apart from x = -10 mm to x = 10 mm, every 640 μs. The focus was positioned at a depth of 1 cm into the kidney, and in the y direction the beam was aligned with the five thermocouples at that depth. The thermocouples were spaced 10 mm apart in the x direction, and thus, only the center three thermocouples (x = 0, 10, -10 mm) were located within the scanned region. Figures 6.15 and 6.16 show the temperature rise versus time in the phantom with no perfusion, and at a perfusion rate of 0.5 ml/min/g, respectively. These figures show that the thermocouples in the scanned region had an approximately 35%

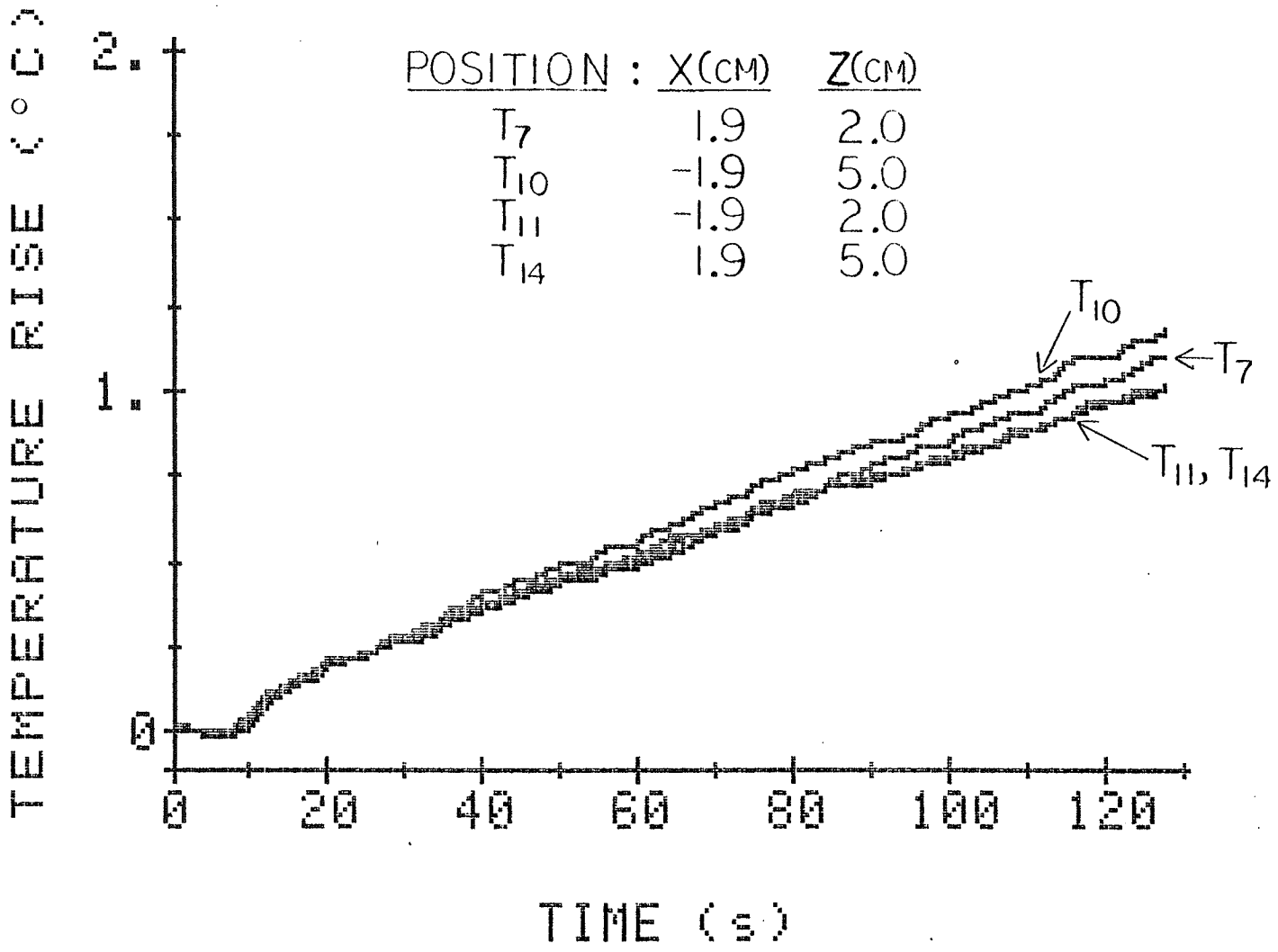

Figure 6.14. Temperature rise versus time recorded at four positions within the tissue phantom ($\langle I_o \rangle$ = 2.5 W/cm^2).

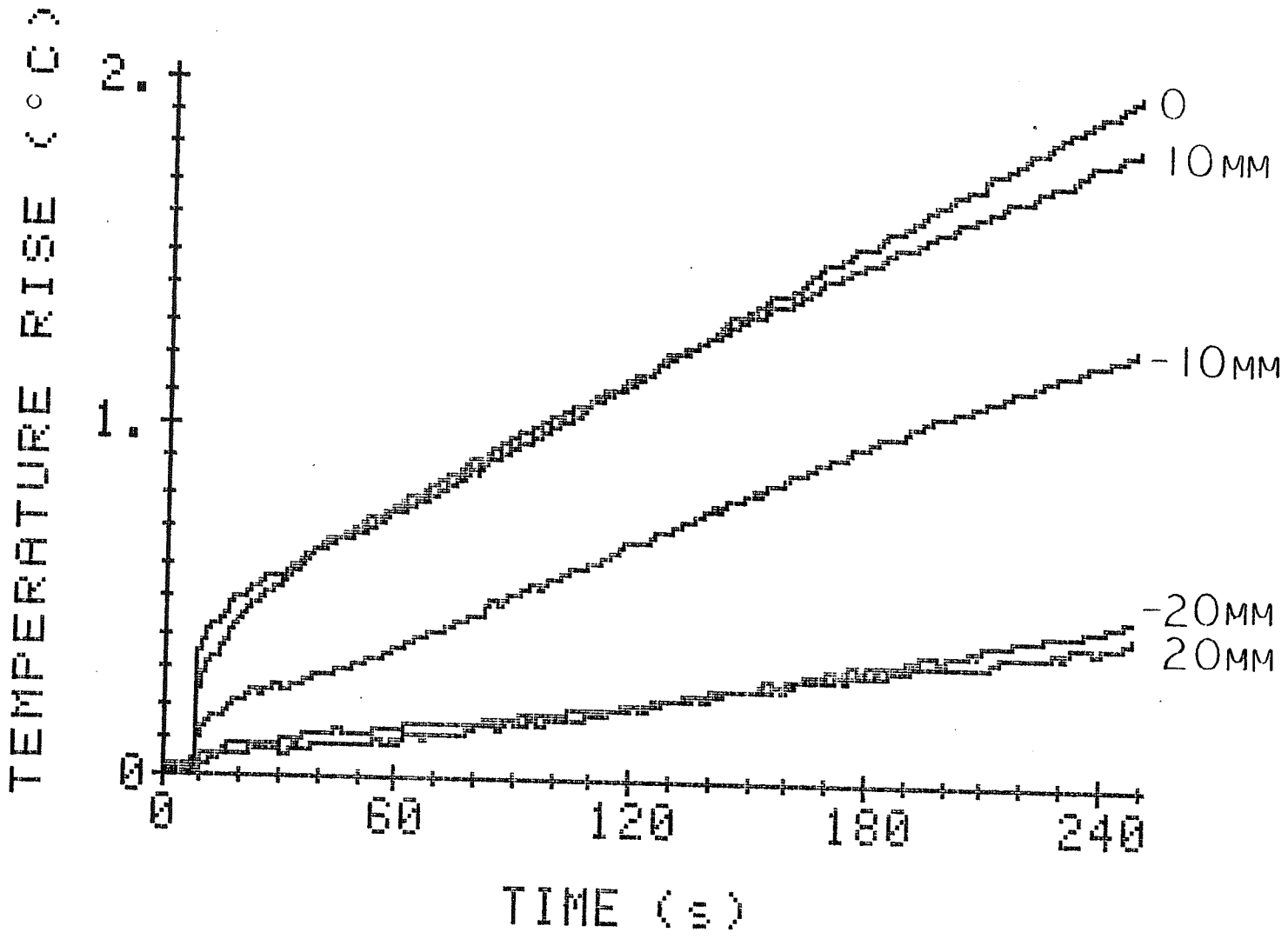

Figure 6.15. Temperature rise versus time recorded at four x positions, at a depth of 10 mm, in the pig kidney with no perfusion ($\langle I_o \rangle$ = 2.5 W/cm^2).

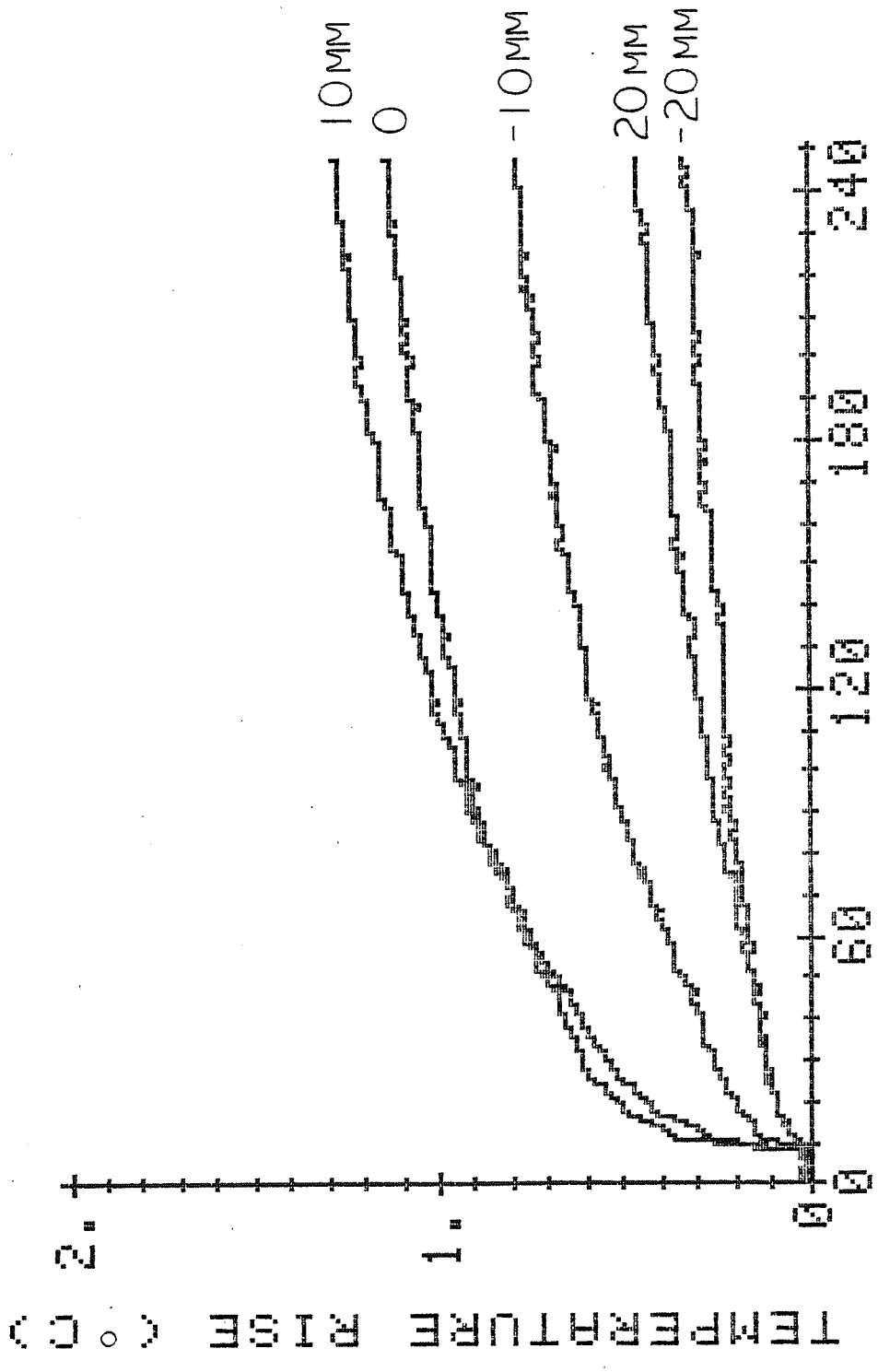

Figure 6.16. Temperature rise versus time recorded at four x positions, at a depth of 10 mm, in the pig kidney with a perfusion rate of 0.5 ml/min/g ($\langle I_o \rangle$ = 2.5 W/cm^2).

variation in their peak temperatures. The lesser temperature rise of the thermocouple located at approximately x = -10 mm can be explained if the thermocouple was just outside of the scanned region. The thermocouples 10 mm from the scanned region (x = 20, -20 mm) experienced a small increase in temperature. Since their temperature rises are similar in both figures, it can be assumed that the heating in these locations was due to heat conduction.

6.5 Discussion

The theoretical model of the acoustical output of a tapered element has been shown to describe well with the experimental data. With this model, it is possible to design other tapered phased arrays with *a priori* knowledge of the array's acoustical output in the y direction.

The results of the acoustical power output measurements suggest that 64 elements, with a 1.79 mm element width, and 580 to 650 kHz frequency range would produce a maximum acoustical power output ranging from approximately 120 to 160 W. For an attenuation coefficient of 0.1 Np/cm/MHz, the total acoustic power available at an 8 cm focal depth for a frequency of 650 kHz can be determined from Eq. (2.1) to be approximately 42 W. Therefore, the maximum time-averaged intensity available to heat the 2.1 cm diameter tumor (see Section 3.3), at a depth of 8 cm, is approximately 13 W/cm^2. If the tumor has an absorption coefficient of 0.08 Np/cm/MHz, an absorbed power density of approximately 1.3 W/cm^3 could be produced at the 8 cm depth. Several theoretical studies suggest that absorbed power densities of 150 to 200 mW/cm^3 in the tumor are necessary to produce tumor

temperatures of at least 43°C [18,33]. Therefore, based on these studies, a 64 element version of TPA2 would be able to treat a 2.1 cm tumor up to 8 cm in depth with an intensity gain of 3 dB.

Based on the intensity gain calculations in Section 3.3, and the acoustical power output measurements, the frequency range of the tapered phased array should be decreased in future designs. A transducer operating at a decreased frequency will be able to treat larger tumors with the same intensity gain and will have a greater maximum acoustical power output. The greater acoustical power outputs with lower frequencies are not only due to decreased internal losses, but also to the larger element widths allowable with the lower frequencies (see Section 3.1). On the other hand, a decrease in frequency will decrease the absorbed power density. For example, at 500 kHz, a time-averaged intensity of 12 W/cm^2 at the tumor will produce an absorbed power density of only 960 mW/cm^3, compared to 1.3 W/cm^3 calculated for the same tumor size and location in the 650 kHz case. However, even an absorbed power density of 960 mW/cm^3 would be sufficient for heating the tumor.

The heating studies using the URI Therm-X tissue phantom and the perfused kidney phantom were of limited usefulness. The spacing of the thermocouples in the URI Therm-X phantom was too large to obtain enough temperature information in the phantom. Both the URI Therm-X phantom and the kidney were too small to obtain useful information on the heating versus depth.

CHAPTER 7

RECOMMENDATIONS FOR FUTURE STUDIES

The results of the initial testing of the multielement transducer showed differences between the theoretical and experimental field intensity distributions. Additional research is needed to determine the reason for the differences and to specify the required modifications to the theoretical model. If the power deposition pattern of the transducer can be modeled with reasonable accuracy, it can be combined with the bio-heat equation to predict the temperature distribution in a given tumor and surrounding normal tissues. The predicted temperature distributions might be used by the hyperthermia system's control algorithm [45] to provide more uniform and constant temperatures in the tumor while minimizing excess heating in normal tissue.

Modeling of the field intensity patterns of the tapered phased array needs to be incorporated with the bio-heat equation to model the temperature distributions in the irradiated tissue. With such a model, the intensity gain and power deposition necessary to heat selectively a given tumor can be determined. Once this is accomplished, the required acoustical power output and frequency range of the array can be better estimated. Based on measurements discussed in Section 6.2, the maximum acoustical power output of the array would appear to be a limiting factor. Thus, commercial development of such a transducer would likely involve measures to increase the maximum output. These measures could include cooling the front face of the array with chilled degassed water and/or cold air flow on the back of the elements.

The evaluation of more complex electrical impedance matching networks is necessary to increase the efficiency of the amplifiers and reduce the effects of variations in the impedances of the elements.

The high intensity ultrasound produced by the tapered phased array may produce nonlinear effects in the tissue. One study showed that for focused beams, the harmonic distortion at the focus appeared to be large enough to be useful in selectively increasing the temperature at depth in tissues [46]. These nonlinear effects should be included in a model for predicting temperature distributions produced by the tapered phased array.

The possibility of cavitation occurring in tissues irradiated with the tapered phased array should be researched. Studies of ultrasonically induced cavitation indicate that transient cavitation occurs with intensities approximately 1500 W/cm^2 in adult organs for frequencies in the 1 to 10 MHz range [47,48,49]. These intensities are perhaps five to seven times greater than those expected to be produced by the tapered phased array. However, another study suggested that cavitation was involved in hind limb paralysis of neonatal mice exposed to 1 MHz ultrasound at an intensity of only 289 W/cm^2 [50]. This intensity is approaching that which is expected to be produced by the tapered phased array. Since the cavitation threshold decreases with frequency, the possibility that cavitation could occur for the frequency range and intensities of the tapered phased array needs to be investigated.

APPENDIX

COMPUTER PROGRAMS

MULTIELEMENT TRANSDUCER FIELD DISTRIBUTION PROGRAM

```
C     THIS PROGRAM CALCULATES THE FIELD INTENSITY DISTRIBUTION
C  OF THE MULTIELEMENT TRANDUCER USING THE RECTANGULAR RADIATOR
C  METHOD.  THE PROGRAM DIVIDES THE ELEMENTS OF THE TRANSDUCER
C  INTO SUBELEMENTS THAT ARE SMALL ENOUGH SO THAT THEIR
C  FIELDS CAN BE REPRESENTED, IN THE REGION OF INTEREST,
C  BY THE FAR-FIELD APPROXIMATION.
C
C  WRITTEN 5/16/85 BY KENNETH OCHELTREE
C  LAST MODIFIED 6/10/85 BY PAUL BENKESER
C
      DIMENSION Z(75),X(75)
      COMPLEX AC(75)
C
C SET TRANSDUCER PARAMETERS
C
C FR IS FREQUENCY IN KHZ
C AT IS ATTENUATION AT 1 MHZ IN NEPERS/CM
C HT IS HEIGHT OF TRANSDUCER ELEMENTS IN MM
C WI IS WIDTH OF TRANSDUCER ELEMENTS IN MM
      DATA FR,AT,HT,WI/1000.,0.,37.,149./
C
C SET FIELD POINT LOCATION PARAMETERS
C
C XS IS X STARTING LOCATION
C YS IS Y STARTING LOCATION
C ZS IS Z STARTING LOCATION
C NX IS NUMBER OF X FIELD POINTS
C NY IS NUMBER OF Y FIELD POINTS
C ST IS THE STEP SIZE BETWEEN POINTS
C
      DATA XS,YS,ZS,NX,NY,ST/-75,0.,76.,75,1,2./
C
      ZMAX=0.0
      DO 5 IX=1,NX
      Z(IX)=0.0
  5   CONTINUE
      CALL FXY
     &(FR,AT,HT,WI,XS,YS,ZS,NX,NY,ST,AC)
         DO 15 IX=1,NX
         Z(IX)=Z(IX)+CABS(AC(IX))**2
         ZMAX=AMAX1(ZMAX,Z(IX))
 15      CONTINUE
      DO 60 I=1,NX
      X(I)=XS+FLOAT(I-1)*ST
      Z(I)=10.*ALOG(Z(I)/ZMAX+1E-20)
 60   CONTINUE
      CALL EZPLOT(X,Z,1,75.0,'MULTX','X(MM)','REL. POWER (dB)'
     $,5.,5.)
      STOP
      END
C
```

```
C SUBROUTINE TO CALCULATE FIELD PRODUCED BY ONE FOCAL POINT
C
      SUBROUTINE FXY(FR,AT,HT,WI,XS,YS,ZS,NX,NY,ST,PC)
      COMPLEX PC(NX,NY),WT,EXPARG,TEMP
      DATA PI/3.1415926536/
      FAR=5.
      WAVE=1500./FR
      PIDW=PI/WAVE
      CAK=2.*PIDW
      ATT=AT*(FR/1000.)**1.1
C
C CONVERT ATTEN TO NP/MM
C
      ATT=ATT/10.
      IQQ=2**IQ
      DO 760 J=1,NY
      DO 760 I=1,NX
 760  PC(I,J)=CMPLX(0.,0.)
C
C  CALCULATE FIELD
C
      ZD=ZS
        NH=1+INT(HT/SQRT(WAVE*ZD/FAR))
        YINC=HT/FLOAT(NH)
        CNSTY=PIDW*YINC
        NW=1+INT(WI/SQRT(WAVE*ZD/FAR))
        XINC=WI/FLOAT(NW)
        CNSTX=PIDW*XINC
        AREA=XINC*YINC
        XP=XS
        DO 980 IX=1,NX
          YP=YS
          DO 960 IY=1,NY
              WT=CMPLX(AREA,0.)
              XE=(XINC-WI)/2.
              DO 920 IW=1,NW
                YE=(YINC-HT)/2.
                XD=XP-XE
                DO 900 IH=1,NH
                  YD=YP-YE
                  ARG=SQRT(XD**2+YD**2+ZD**2)
                  XARG=CNSTX*XD/ARG
                  SINCX=1.
                  IF(ABS(XARG) .GT. .0001)SINCX=SIN(XARG)/XARG
                  YARG=CNSTY*YD/ARG
                  SINCY=1.
                  IF(ABS(YARG) .GT. .0001)SINCY=SIN(YARG)/YARG
                  EXPARG=CEXP(CMPLX(-ARG*ATT,-ARG*CAK))
                  TEMP=EXPARG*WT*CMPLX(SINCX*SINCY/ARG,0.)
                  PC(IX,IY)=PC(IX,IY)+TEMP
                  YE=YE+YINC
 900              CONTINUE
                  XE=XE+XINC
 920            CONTINUE
              YP=YP+ST
```

```
960       CONTINUE
          XP=XP+ST
980     CONTINUE
      RETURN
      END
```

TAPERED PHASED ARRAY FIELD DISTRIBUTION PROGRAM (X DIRECTION)

```
C    THIS PROGRAM CALCULATES THE FIELD INTENSITY DISTRIBUTION
C PRODUCED BY A TAPERED PHASED ARRAY IN THE X-Z PLANE
C USING THE RECTANGULAR RADIATOR METHOD.  THE PROGRAM
C HANDLES MULTIPLE FOCAL LOCATIONS PRODUCED BY THE
C PHASED ARRAY.  THE ACOUSTIC OUTPUT ALONG THE HEIGHT OF
C THE ELEMENT IS WEIGHTED TO SIMULATE A TAPERED ELEMENT.
C THE DATA IS IN LINE PLOT FORM AND CAN BE PLOTTED USING
C EZPLOT.
C
C WRITTEN 6/24/84 BY KENNETH OCHELTREE
C LAST MODIFIED 5/15/85 BY PAUL BENKESER
C
C DIMENSIONS ARE Z(NX),AC(NX),XF(NF),X(NX),YF(NF),ZF(NF)
C
      DIMENSION XF(20),YF(20),ZF(20),Z(100),WGHT(100),X(100)
      COMPLEX AC(100)
C
C SET ARRAY PARAMETERS
C
C FR IS FREQUENCY IN KHZ
C AT IS ATTENUATION AT 1 MHZ IN NEPERS/CM
C NE IS NUMBER OF ELEMENTS IN ARRAY
C HT IS HEIGHT OF ARRAY ELEMENTS IN MM
C WI IS WIDTH OF ARRAY ELEMENTS IN MM
C SP IS CENTER TO CENTER SPACING OF ELEMENTS IN MM
C IQ IS NUMBER OF BITS QUANTIZATION (IQ=0 MEANS NO QUANTIZATION)
      DATA FR,AT,NE,HT,WI,SP,IQ/650.,0.08,64,152.4,1.78,1.97,4/
C
C SET TAPERED CERAMIC PARAMETERS
C
C QM IS THE MECHANICAL Q
C DT IS THE DEGREE OF TAPER IN KHZ/MM
C FRL IS THE LOW FREQUENCY OF THE TAPER
C
      DATA QM,DT,FRL/8.,1.2,500./
C
C SET FOCUS LOCATION PARAMETERS
C
C NF IS NUMBER OF POINTS IN SCAN PATH
C TI IS ARRAY OF TIMES AT EACH SCAN POINT
C XF IS VECTOR OF X FOCUS LOCATIONS
C ZF IS VECTOR OF Z FOCUS LOCATIONS
C
      DATA NF,XF(1),ZF(1)/1,0.,80./
C
C SET FIELD POINT LOCATION PARAMETERS
C
C XS IS X STARTING LOCATION
C ZS IS Z STARTING LOCATION
C YS IS Y STARTING LOCATION
C NX IS NUMBER OF X FIELD POINTS
C NZ IS NUMBER OF Z FIELD POINTS
```

```
C ST IS THE STEP SIZE BETWEEN POINTS
C
      DATA XS,YS,ZS,NX,ST/-5.,50.,80.,20,.5/
C
      DO 5 IX=1,NX
      Z(IX)=0.0
  5   CONTINUE
C
C LOOP ON NUMBER OF FOCUS LOCATIONS
C
      DO 20 I=1,NF
      CALL FCA(FR,AT,NE,HT,WI,SP,IQ,XF(I),ZF(I),XS,ZS,
     $YS,NX,ST,AC,QM,DT,FRL)
         DO 15 IX=1,NX
         Z(IX)=Z(IX)+CABS(AC(IX))**2
 15      CONTINUE
 20   CONTINUE
      WRITE(8)(Z(IX),IX=1,NX)
C
C SET UP ARRAY OF X POSITIONS FOR EZPLOT
C
      DO 34 I=1,NX
      X(I)=XS+(I-1)*ST
  34  CONTINUE
      WRITE(8)(X(I),I=1,NX)
C
      STOP
      END
C
C SUBROUTINE TO CALCULATE FIELD PRODUCED BY ONE FOCAL POINT
C
      SUBROUTINE FCA(FR,AT,NE,H,WI,SP,IQ,XF,ZF,XS,ZS,YS,NX,
     $ST,AC,QM,DT,FRL)
      COMPLEX RAI(128),AC(NX),WT,EXPARG,TEMP
      COMPLEX WGHT(100)
      DATA PI/3.1415926536/
      FAR=5.
      HT=H
      WAVE=1500./FR
      PIDW=PI/WAVE
      CAK=2.*PIDW
      SPACT=FLOAT(NE-1)*SP
      ATT=AT*(FR/1000.)**1.1
C
C CONVERT ATTEN TO NP/MM
C
      ATT=ATT/10.
      IQQ=2**IQ
C
C  CALCULATE PHASES FOR ELEMENTS TO ACHIEVE A FOCUS
C
      XVAL=-SPACT/2.
      DO 680 I=1,NE
         RDIST=SQRT((XF-XVAL)**2+ZF**2)
         CAR=CAK*RDIST
```

```
          XVAL=XVAL+SP
          IF(IQQ .EQ. 1)GO TO 660
          CAR=2.*PI*AINT(.5+FLOAT(IQQ)*CAR/(2.*PI))/FLOAT(IQQ)
 660      CONTINUE
          RAI(I)=CMPLX(COS(CAR),SIN(CAR))
 680   CONTINUE
C
       DO 760 I=1,NX
 760   AC(I)=CMPLX(0.)
C
C   CALCULATE FIELD
C
       XD=(SPACT+WI)/2.+XS
       YST=-HT/2.-YS
       NHL=9999
       ZD=ZS
       SNE=XD
C
C      COMPUTE NUMBER OF SUBELEMENTS IN Y DIMENSION
C
         NH=1+INT(HT/SQRT(WAVE*ZD/FAR))
C
C      TO INSURE THAT THE WEIGHTING FUNCTION HAS ITS
C    DESIRED EFFECT, A MINIMUM VALUE FOR NH IS SET.
C
         IF(NH.LT.40) NH=40
C
         IF(NH.EQ.NHL) GOTO 780
         YINC=HT/FLOAT(NH)
         CALL WEIGHT(WGHT,YINC,NH,FR,QM,DT,FRL)
         CNSTY=PIDW*YINC
 780     SNH=YST+YINC/2.
C
C      COMPUTE THE NUMBER OF SUBELEMENTS IN THE X DIMENSION
C
         IF(NW.EQ.1) GOTO 785
         NW=1+INT(WI/SQRT(WAVE*ZD/FAR))
         XINC=WI/FLOAT(NW)
         CNSTX=PIDW*XINC
 785     WRITE(6,790)ZS,NH,NW
 790     FORMAT(' Z=',F5.1,' NH=',I3,' NW=',I3)
C
C      SUM THE CONTRIBUTIONS FROM EACH ARRAY ELEMENT
C
         DO 940 K=1,NE
            IF(K .EQ. 1)XD=XD-XINC/2.
            WT=RAI(K)*CMPLX(XINC*YINC,0.)
            SNW=XD
            DO 920 L=1,NW
               SNX=XD
               YD=SNH
               DO 900 M=1,NH
                  DO 880 IX=1,NX
                     ARG=SQRT(XD**2+YD**2+ZD**2)
                     XARG=CNSTX*XD/ARG
```

```
                    SINCX=1.
                    IF(ABS(XARG) .GT. .0001)SINCX=SIN(XARG)/XARG
                    YARG=CNSTY*YD/ARG
                    SINCY=1.
                    IF(ABS(YARG) .GT. .0001)SINCY=SIN(YARG)/YARG
                    EXPARG=CEXP(CMPLX(-ARG*ATT,-ARG*CAK))
                    TEMP=EXPARG*WT*WGHT(M)*CMPLX(SINCX*SINCY/ARG,0.)
                    AC(IX)=AC(IX)+TEMP
                    XD=XD+ST
 880             CONTINUE
                 XD=SNX
                 YD=YD+YINC
 900           CONTINUE
               XD=XD-XINC
 920        CONTINUE
            XD=SNW-SP
 940     CONTINUE
         XD=SNE
         NHL=NH
       RETURN
       END
C
C THIS SUBROUTINE WEIGHTS THE ACOUSTICAL OUTPUT ALONG
C THE HEIGHT OF THE ELEMENT.
C
       SUBROUTINE WEIGHT(WGHT,YINC,NH,FR,QM,DT,FRL)
       COMPLEX WGHT(100),ZSS,WR
       REAL IM
       DO 1000 I=1,NH
       FY=YINC*FLOAT(I)*DT+FRL
       A=QM*(FY/FR-FR/FY)
       ZSS=CMPLX(1.,A)
       PHAS=ATAND(AIMAG(ZSS)/REAL(ZSS))
       D=1./(2.*FR)
       WR=1./(D**2*(CMPLX(1.,A)**2))
       MAGN=SQRT((REAL(WR))**2+(AIMAG(WR))**2)
       IM=MAGN*SIND(PHAS)
       RE=MAGN*COSD(PHAS)
       WGHT(I)=CMPLX(RE,IM)
 1000  CONTINUE
       RETURN
       END
```

TAPERED PHASED ARRAY FIELD DISTRIBUTION PROGRAM (Y DIRECTION)

```
C     THIS PROGRAM CALCULATES THE FIELD INTENSITY
C  DISTRIBUTION PRODUCED BY A TAPERED PHASED ARRAY IN
C  THE Y-Z PLANE USING THE RECTANGULAR RADIATOR METHOD.
C  THE PROGRAM CAN HANDLE MULTIPLE
C  LOCATIONS PRODUCED BY THE PHASED ARRAY.  THE
C  OUTPUT ALONG THE HEIGHT OF THE ARRAY IS WEIGHTED
C  TO SIMULATE THE RESPONSE OF A TAPERED ELEMENT.
C  THE RESULTING DATA IS IN LINE PLOT FORM AND CAN BE
C  PLOTTED USING EZPLOT.
C
C  WRITTEN 6/24/84 BY KENNETH OCHELTREE
C  LAST MODIFIED 5/15/85 BY PAUL BENKESER
C
C DIMENSIONS ARE Z(NY),AC(NY),XF(NF),ZF(NF)
C
      DIMENSION XF(20),ZF(20),Z(100),Y(100)
      COMPLEX AC(100)
C
C SET ARRAY PARAMETERS
C
C FR IS FREQUENCY IN KHZ
C AT IS ATTENUATION AT 1 MHZ IN NEPERS/CM
C NE IS NUMBER OF ELEMENTS IN ARRAY
C HT IS HEIGHT OF ARRAY ELEMENTS IN MM
C WI IS WIDTH OF ARRAY ELEMENTS IN MM
C SP IS CENTER TO CENTER SPACING OF ELEMENTS IN MM
C IQ IS NUMBER OF BITS QUANTIZATION (IQ=0 MEANS NO QUANTIZATION)
C
      DATA FR,AT,NE,HT,WI,SP,IQ/600.,0.,16,152.4,1.4,1.65,4/
C
C SET TAPERED CERAMIC PARAMETERS
C
C QM IS THE MECHANICAL Q
C DT IS THE DEGREE OF TAPER IN KHZ/MM
C FRL IS THE LOW FREQUENCY OF THE TAPER
C
      DATA QM,DT,FRL/15.,1.20,500./
C
C SET FOCUS LOCATION PARAMETERS
C
C NF IS NUMBER OF POINTS IN SCAN PATH
C TI IS ARRAY OF TIMES AT EACH SCAN POINT
C XF IS VECTOR OF X FOCUS LOCATIONS
C ZF IS VECTOR OF Z FOCUS LOCATIONS
C
      DATA NF,XF(1),ZF(1)/1,0.,100./
C
C SET FIELD POINT LOCATION PARAMETERS
C
C YS IS Y STARTING LOCATION
C XS IS X STARTING LOCATION
C ZS IS Z STARTING LOCATION
```

```
C NY IS NUMBER OF Y FIELD POINTS
C NZ IS NUMBER OF Z FIELD POINTS
C ST IS THE STEP SIZE BETWEEN POINTS
C
      DATA XS,YS,ZS,NY,ST/0.,-42.,100.,51,2./
C
C LOOP ON NUMBER OF FOCUS LOCATIONS
C
      DO 5 IY=1,NY
      Z(IY)=0.0
  5   CONTINUE
      DO 20 I=1,NF
      CALL FCA(FR,AT,NE,HT,WI,SP,IQ,XF(I),ZF(I),XS,ZS,YS
     $,NY,ST,AC,QM,DT,FRL)
         DO 15 IY=1,NY
         Z(IY)=Z(IY)+CABS(AC(IY))**2
 15      CONTINUE
 20   CONTINUE
      WRITE(8)(Z(IY),IY=1,NY)
C
C SET UP ARRAY OF Y POSITIONS FOR EZPLOT
C
      DO 34 I=1,NY
      Y(I)=YS+(I-1)*ST
 34   CONTINUE
      WRITE(8)(Y(I),I=1,NY)
      STOP
      END
C
C SUBROUTINE TO CALCULATE FIELD PRODUCED BY ONE FOCAL POINT
C
      SUBROUTINE FCA(FR,AT,NE,HT,WI,SP,IQ,XF,ZF,XS,ZS,YS,
     $NY,ST,AC,QM,DT,FRL)
      COMPLEX RAI(128),AC(NY),WT,EXPARG,TEMP
      COMPLEX WGHT(100)
      DATA PI/3.1415926536/
      FAR=5.
      WAVE=1500./FR
      PIDW=PI/WAVE
      CAK=2.*PIDW
      SPACT=FLOAT(NE-1)*SP
      ATT=AT*(FR/1000.)**1.1
C
C CONVERT ATTEN TO NP/MM
C
      ATT=ATT/10.
      IQQ=2**IQ
C
C  CALCULATE PHASES FOR ELEMENTS TO ACHIEVE A FOCUS
C
      XVAL=-SPACT/2.
      DO 680 I=1,NE
         RDIST=SQRT((XF-XVAL)**2+ZF**2)
         CAR=CAK*RDIST
         XVAL=XVAL+SP
```

```
          IF(IQQ .EQ. 1)GO TO 660
          CAR=2.*PI*AINT(.5+FLOAT(IQQ)*CAR/(2.*PI))/FLOAT(IQQ)
 660      CONTINUE
          RAI(I)=CMPLX(COS(CAR),SIN(CAR))
 680   CONTINUE
C
       DO 760 I=1,NY
 760   AC(I)=CMPLX(0.)
C
C   CALCULATE FIELD
C
       XD=(SPACT+WI)/2.+XS
       YST=-HT/2.-YS
       ZD=ZS
       SNE=XD
       NHL=999
C
C      COMPUTE NUMBER OF SUBELEMENTS IN Y DIMENSION
C
         NH=1+INT(HT/SQRT(WAVE*ZD/FAR))
C
C      TO INSURE THAT THE WEIGHTING FUNCTION HAS ITS
C     DESIRED EFFECT, A MINIMUM NH IS SET.
C
         IF(NH.LT.40) NH=40
C
         IF(NH.EQ.NHL) GOTO 780
         YINC=HT/FLOAT(NH)
         CALL WEIGHT(WGHT,YINC,NH,FR,QM,DT,FRL)
         CNSTY=PIDW*YINC
 780     SNH=YST+YINC/2.
C
C      COMPUTE THE NUMBER OF SUBELEMENTS IN THE X DIMENSION
C
         IF(NW.EQ.1) GOTO 785
         NW=1+INT(WI/SQRT(WAVE*ZD/FAR))
         XINC=WI/FLOAT(NW)
         CNSTX=PIDW*XINC
 785     WRITE(6,790)ZS,NH,NW
 790     FORMAT(' Z=',F5.1,' NH=',I3,' NW=',I3)
C
C       SUM THE CONTRIBUTIONS FROM EACH ARRAY ELEMENT
C
         DO 940 K=1,NE
            IF(K .EQ. 1)XD=XD-XINC/2.
            WT=RAI(K)*CMPLX(XINC*YINC,0.)
            SNW=XD
            DO 920 L=1,NW
               YD=SNH
               DO 900 M=1,NH
                  SNY=YD
                  DO 880 IY=1,NY
                     ARG=SQRT(XD**2+YD**2+ZD**2)
                     XARG=CNSTX*XD/ARG
                     SINCX=1.
```

```
                    IF(ABS(XARG) .GT. .0001)SINCX=SIN(XARG)/XARG
                    YARG=CNSTY*YD/ARG
                    SINCY=1.
                    IF(ABS(YARG) .GT. .0001)SINCY=SIN(YARG)/YARG
                    EXPARG=CEXP(CMPLX(-ARG*ATT,-ARG*CAK))
                    TEMP=EXPARG*WT*WGHT(M)*CMPLX(SINCX*SINCY/ARG,0.)
                    AC(IY)=AC(IY)+TEMP
                    YD=YD-ST
 880             CONTINUE
                 YD=SNY
                 YD=YD+YINC
 900           CONTINUE
               XD=XD-XINC
 920        CONTINUE
            XD=SNW-SP
 940     CONTINUE
         XD=SNE
         NHL=NH
       RETURN
       END
C
C   THIS SUBROUTINE WEIGHTS THE ACOUSTICAL OUTPUT ALONG
C THE HEIGHT OF THE ELEMENT TO SIMULATE A TAPERED ELEMENT.
C
       SUBROUTINE WEIGHT(WGHT,YINC,NH,FR,QM,DT,FRL)
       COMPLEX WGHT(100),ZSS,WR
       REAL IM
       DO 1000 I=1,NH
       FY=YINC*FLOAT(I)*DT+FRL
       A=QM*(FY/FR-FR/FY)
       ZSS=CMPLX(1.,A)
       PHAS=ATAND(AIMAG(ZSS)/REAL(ZSS))
       D=1./(2.*FR)
       WR=1./(D**2*(CMPLX(1.,A)**2))
       MAGN=SQRT((REAL(WR))**2+(AIMAG(WR))**2)
       IM=MAGN*SIND(PHAS)
       RE=MAGN*COSD(PHAS)
       WGHT(I)=CMPLX(RE,IM)
 1000 CONTINUE
       RETURN
       END
```

TAPERED PHASED ARRAY FIELD DISTRIBUTION PROGRAM (Z DIRECTION)

```
C    THIS PROGRAM CALCULATES THE FIELD INTENSITY DISTRIBUTION
C PRODUCED BY A TAPERED PHASED ARRAY USING THE
C HANDLES MULTIPLE FOCAL LOCATIONS PRODUCED BY THE
C PHASED ARRAY.  THE ACOUSTIC OUTPUT ALONG THE HEIGHT OF
C THE ELEMENT IS WEIGHTED TO SIMULATE A TAPERED ELEMENT.
C
C WRITTEN 6/24/84 BY KENNETH OCHELTREE
C LAST MODIFIED 5/15/85 BY PAUL BENKESER
C
C DIMENSIONS ARE Z(NZ),AC(NZ),ZP(NZ),XF(NF),YF(NF),ZF(NF)
C
      DIMENSION XF(20),ZF(20),Z(125),ZP(125)
      COMPLEX AC(125)
C
C SET ARRAY PARAMETERS
C
C FR IS FREQUENCY IN KHZ
C AT IS ATTENUATION AT 1 MHZ IN NEPERS/CM
C NE IS NUMBER OF ELEMENTS IN ARRAY
C HT IS HEIGHT OF ARRAY ELEMENTS IN MM
C WI IS WIDTH OF ARRAY ELEMENTS IN MM
C SP IS CENTER TO CENTER SPACING OF ELEMENTS IN MM
C IQ IS NUMBER OF BITS QUANTIZATION (IQ=0 MEANS NO QUANTIZATION)
      DATA FR,AT,NE,HT,WI,SP,IQ/500.,.08,64,152.4,1.78,1.97,4/
C
C SET FOCUS LOCATION PARAMETERS
C
C NF IS NUMBER OF POINTS IN SCAN PATH
C TI IS ARRAY OF TIMES AT EACH SCAN POINT
C XF IS VECTOR OF X FOCUS LOCATIONS
C ZF IS VECTOR OF Z FOCUS LOCATIONS
C
      DATA NF,XF(1),ZF(1)/1,0.,80./
C
C SET TAPERED CERAMIC PARAMETERS
C
C QM IS THE MECHANICAL Q
C DT IS THE DEGREE OF TAPER IN MM/KHZ
C FRL IS THE LOW FREQUENCY OF THE TAPER
C
      DATA QM,DT,FRL/8.,1.2,450./
C
C SET FIELD POINT LOCATION PARAMETERS
C
C XS IS X STARTING LOCATION
C ZS IS Z STARTING LOCATION
C YS IS Y STARTING LOCATION
C NX IS NUMBER OF X FIELD POINTS
C NZ IS NUMBER OF Z FIELD POINTS
C ST IS THE STEP SIZE BETWEEN POINTS
C
      DATA XS,YS,ZS,NX,NZ,ST/0.,-34.,4.,1,35,3./
```

```
C
      DO 5 IZ=1,NZ
      Z(IZ)=0.0
  5   CONTINUE
C
C LOOP ON NUMBER OF FOCUS LOCATIONS
C
      DO 20 I=1,NF
      CALL FCA(FR,AT,NE,HT,WI,SP,IQ,XF(I),ZF(I),XS,ZS,
     $YS,NX,NZ,ST,AC,QM,DT,FRL)
         DO 10 IZ=1,NZ
         Z(IZ)=Z(IZ)+CABS(AC(IZ))**2
 10      CONTINUE
 20   CONTINUE
         WRITE(8)(Z(L),L=1,NZ)
C
C SET UP ARRAY OF Z POSITIONS FOR EZPLOT
C
      DO 34 I=1,NZ
      ZP(I)=ZS+(I-1)*ST
  34  CONTINUE
      WRITE(8)(ZP(I),I=1,NZ)
C
      STOP
      END
C
C SUBROUTINE TO CALCULATE FIELD PRODUCED BY ONE FOCAL POINT
C
      SUBROUTINE FCA(FR,AT,NE,HT,WI,SP,IQ,XF,ZF,XS,ZS,YS,NX,
     $NZ,ST,AC,QM,DT,FRL)
      COMPLEX RAI(128),AC(NZ),WT,EXPARG,TEMP
      COMPLEX WGHT(100)
      DATA PI/3.1415926536/
      FAR=5.
      WAVE=1500./FR
      PIDW=PI/WAVE
      CAK=2.*PIDW
      SPACT=FLOAT(NE-1)*SP
      ATT=AT*(FR/1000.)**1.1
C
C CONVERT ATTEN TO NP/MM
C
      ATT=ATT/10.
      IQQ=2**IQ
C
C  CALCULATE PHASES FOR ELEMENTS TO ACHIEVE A FOCUS
C
      XVAL=-SPACT/2.
      DO 680 I=1,NE
         RDIST=SQRT((XF-XVAL)**2+ZF**2)
         CAR=CAK*RDIST
         XVAL=XVAL+SP
         IF(IQQ .EQ. 1)GO TO 660
         CAR=2.*PI*AINT(.5+FLOAT(IQQ)*CAR/(2.*PI))/FLOAT(IQQ)
 660     CONTINUE
```

```
         RAI(I)=CMPLX(COS(CAR),SIN(CAR))
 680  CONTINUE
C
      DO 760 J=1,NZ
 760  AC(J)=CMPLX(0.)
C
C  CALCULATE FIELD
C
      XD=(SPACT+WI)/2.+XS
      YST=-HT/2.-YS
      NHL=9999
      ZD=ZS
      SNE=XD
      DO 960 IZ=1,NZ
C
C     COMPUTE NUMBER OF SUBELEMENTS IN Y DIMENSION
C
        NH=1+INT(HT/SQRT(WAVE*ZD/FAR))
C
C     TO INSURE THAT THE WEIGHTING FUNCTION HAS ITS
C   DESIRED EFFECT, A MINIMUM VALUE FOR NH IS SET.
C
        IF(NH.LT.40) NH=40
C
        IF(NH.EQ.NHL) GOTO 780
        YINC=HT/FLOAT(NH)
        CALL WEIGHT(WGHT,YINC,NH,FR,QM,DT,FRL)
        CNSTY=PIDW*YINC
 780    SNH=YST+YINC/2.
C
C     COMPUTE THE NUMBER OF SUBELEMENTS IN THE X DIMENSION
C
        IF(NW.EQ.1) GOTO 785
        NW=1+INT(WI/SQRT(WAVE*ZD/FAR))
        XINC=WI/FLOAT(NW)
        CNSTX=PIDW*XINC
 785    WRITE(6,790)ZD,NH,NW
 790    FORMAT(' Z= ',F5.1,' NH=',I5,' NW=',I5)
C
C     SUM THE CONTRIBUTIONS FROM EACH ARRAY ELEMENT
C
        DO 940 K=1,NE
           IF(K .EQ. 1)XD=XD-XINC/2.
           WT=RAI(K)*CMPLX(XINC*YINC,0.)
           SNW=XD
           DO 920 L=1,NW
              SNX=XD
              YD=SNH
              DO 900 M=1,NH
                 DO 880 IX=1,NX
                    ARG=SQRT(XD**2+YD**2+ZD**2)
                    XARG=CNSTX*XD/ARG
                    SINCX=1.
                    IF(ABS(XARG) .GT. .0001)SINCX=SIN(XARG)/XARG
                    YARG=CNSTY*YD/ARG
```

```
                    SINCY=1.
                    IF(ABS(YARG) .GT. .0001)SINCY=SIN(YARG)/YARG
                    EXPARG=CEXP(CMPLX(-ARG*ATT,-ARG*CAK))
                    TEMP=EXPARG*WT*WGHT(M)*CMPLX(SINCX*SINCY/ARG,0.)
                    AC(IZ)=AC(IZ)+TEMP
                    XD=XD+ST
  880             CONTINUE
                  XD=SNX
                  YD=YD+YINC
  900           CONTINUE
                XD=XD-XINC
  920         CONTINUE
              XD=SNW-SP
  940       CONTINUE
            XD=SNE
            ZD=ZD+ST
            NHL=NH
  960   CONTINUE
        RETURN
        END
C
C THIS SUBROUTINE WEIGHTS THE ACOUSTICAL OUTPUT ALONG
C THE HEIGHT OF THE ELEMENT.
C
        SUBROUTINE WEIGHT(WGHT,YINC,NH,FR,QM,DT,FRL)
        COMPLEX WGHT(100),ZSS,WR
        REAL IM
        DO 1000 I=1,NH
        FY=YINC*FLOAT(I)*DT+FRL
        A=QM*(FY/FR-FR/FY)
        ZSS=CMPLX(1.,A)
        PHAS=ATAND(AIMAG(ZSS)/REAL(ZSS))
        D=1./(2.*FR)
        WR=1./(D**2*(CMPLX(1.,A)**2))
        MAGN=SQRT((REAL(WR))**2+(AIMAG(WR))**2)
        IM=MAGN*SIND(PHAS)
        RE=MAGN*COSD(PHAS)
        WGHT(I)=CMPLX(RE,IM)
 1000   CONTINUE
        RETURN
        END
```

REFERENCES

[1] P. M. Corry, K. Jabboury, E. P. Armour, and J. S. Kong, "Human cancer treatment with ultrasound," IEEE Trans. Sonics Ultrason., vol. SU-31, no. 5, pp. 444-456, 1984.

[2] C. W. Song, "Physiological factors in hyperthermia," NCI Monograph, vol. 61, pp. 169-176, 1982.

[3] G. M. Hahn, "Hyperthermia for the engineer : a short biological primer," IEEE Trans. Biomed. Eng., vol. BME-31, no. 1, 1984.

[4] F. W. Kremkau, "Cancer therapy with ultrasound: A historical review," J. Clin. Ultrasound, vol. 7, pp. 287-300, 1979.

[5] B. Barlogie, P. M. Corry, E. Yip, L. Lippman, D. A. Johnston, K. Khalil, T. F. Tencezynski, E. Reilly, R. Lawson, G. Dosik, B. Rigor, R. Hankenson, and E. J. Freireich, "Total-body hyperthermia with and without chemotherapy for advanced human neoplasms," Cancer Res., vol. 39, pp. 1481-1489, 1979.

[6] R. T. Pettigrew, J. M. Galt, C. M. Ludgatem, and A. N. Smith, "Clinical effects of whole-body hyperthermia in advanced malignancy," Br. Med. J., vol. 4, pp. 679-682, 1974.

[7] J. M. Bull, D. E. Lees, W. H. Schuette, J. Whang-Peng, E. R. Atkinson, G. Bynum, R. Smith, J. S. Gottdiener, H. Gralnick, and V. T. DeVita, "Whole-body hyperthermia - now a feasible addition to cancer treatment," Proc. Am. Assoc. Cancer Res., vol. 19, p. 405, 1978.

[8] G. M. Hahn, P. Kernahan, A. Martinez, D. Pounds, and S. Prionas, "Some heat transfer problems associated with heating by ultrasound, microwaves, or radiofrequency," Annals of N.Y. Acad. Sci., vol. 335, pp. 327-346, 1980.

[9] D. A. Christiansen and C. H. Durney, "Hyperthermia production for cancer therapy: A review of fundamentals and methods," J. Microwave Power, vol. 16, pp. 89-105, 1981.

[10] P. P. Lele, "Hyperthermia by ultrasound," Proc. Int. Symp. on Cancer Therapy by Hyperthermia and Radiation, pp. 108-178, 1975.

[11] J. W. Hunt, "Applications of microwave, ultrasound, and radiofrequency heating," Proc. Third Int. Symp.: Cancer Therapy by Hyperthermia, Drugs, and Radiation, NCI Monograph, vol. 61, pp. 447-456, 1982.

[12] A. K. Chan, R. A. Sigelmann, and A. W. Guy, "Calculations of therapeutic heat generated in fat-muscle-bone layers," IEEE Trans. Biomed. Eng., vol. BME-21, pp. 280-294, 1974.

[13] J. B. Marmor, D. P. Pounds, T. Postic, and G. M. Hahn, "Treatment of superficial human neoplasms by local hyperthermia induced by ultrasound," Cancer, vol. 43, pp. 188-192, 1979.

[14] C. Marchal, P. Bey, R. Metz, M. L. Gaulard, and J. Robert, "Treatment of superficial human cancerous nodules by local ultrasound hyperthermia," Br. J. Cancer, vol. 45, Suppl. V, pp. 243-245, 1982.

[15] P. M. Corry, B. Barlogie, E. J. Tilchen, and E. P. Armour, "Ultrasound-induced hyperthermia for treatment of human superficial tumors," Int. J. Radiat. Oncol. Biol. Phys., vol. 8, pp. 1225-1229, 1982.

[16] E. J. Seppi, E. G. Shapiro, and L. T. Zitelli, "Ultrasonic system for hyperthermia," Abstract Ad-22, Rad. Res. Soc. Meeting, 1985.

[17] P. Fessenden, E. R. Lee, T. L. Anderson, J. W. Strohbehn, J. L. Meyer, T. V. Samulski, and J. B. Marmor, "Experience with a multitransducer ultrasound system for localized hyperthermia of deep tissues," IEEE Trans. Biomed. Eng., vol. BME-31, no. 1, 1984.

[18] P. Fessenden, J. L. Meyer, R. Valdagni, E. R. Lee, T. V. Samulski, D. S. Kapp, and M. A. Bagshaw, "Analysis of deep hyperthermia treatments using six ultrasound transducers in a fixed frequency/geometry configuration," Abstract Ad-27, Rad. Res. Soc. Meeting, 1985.

[19] P. P. Lele and K. J. Parker, "Temperature distributions in tissues during local hyperthermia by stationary or steered beams of unfocused or focused ultrasound," Br. J. Cancer, vol. 45, Suppl. V, pp. 108-121, 1982.

[20] R. J. Dickinson, "An ultrasound system for local hyperthermia using scanned focused transducers," IEEE Trans. Biomed. Eng., vol. BME-31, pp. 120-125, 1984.

[21] S. A. Goss, R. L. Johnston, and F. Dunn, "Comprehensive compilation of empirical ultrasonic properties of mammalian tissues," J. Acoust. Soc. Am., vol. 64, no. 2, pp. 423-457, 1978.

[22] D. A. Berlincourt, "Piezoelectric crystals and ceramics," Ultrasound Transducer Materials, O. E. Mattiat Ed., New York: Plenum Press, pp. 63-124, 1971.

[23] C. Bruneel, B. Delannay, R. Torguet, E. Bridoux, and H. Lasota, "Electrical coupling effects in an ultrasonic transducer array," Ultrasonics, vol. 17, no. 6, pp. 255-260, 1979.

[24] D. A. Berlincourt, D. R. Curran and H. Jaffe, "Piezoelectric and piezomagnetic materials and their function in transducers," Physical Acoustics, W. P. Mason Ed., New York: Academic Press, pp. 170-267, 1964.

[25] W. M. Rohsenow, H. V. Choi, Heat, Mass and Momentum Transfer, Englewood Cliffs, NJ: Prentice Hall, pp. 104-105, 1961.

[26] H. S. Carslaw and J. C. Jaeger, Conduction of Heat in Solids, Oxford, England: Claredon, p. 21, 1959.

[27] K. B. Ocheltree, P. J. Benkeser, L. A. Frizzell, and C. A. Cain, "An ultrasonic phased array applicator for hyperthermia," IEEE Trans. Sonics Ultrason., vol. SU-31, no. 5, pp. 526-531, 1984.

[28] D. G. Tucker, "Some aspects of the design of strip arrays," Acoustica, vol. 6, pp. 403-411, 1956.

[29] A. Macovski, "Ultrasonic imaging using arrays," Proc. of the IEEE, vol. 67, no. 4, pp. 484-495, 1979.

[30] B. D. Steinberg, Principles of Aperature and Array System Design. New York: Wiley, pp. 305-309, 1976.

[31] T. F. Heuter and R. H. Bolt, Sonics. New York: Wiley, pp. 106-107, 1966.

[32] R. T. Beyer, and S. V. Letcher, Physical Ultrasonics, New York: Academic Press, p.52, 1969.

[33] R. B. Roemer, W. Swindell, S. T. Clegg, and R. L. Kress, "Simulation of focused, scanned ultrasonic heating of deep-seated tumors: The effect of blood perfusion," IEEE Trans. Sonics Ultrason., vol. SU-31, no. 5, pp. 457-466, 1984.

[34] K. B. Ocheltree, "Theoretical analysis of ultrasonic linear phased arrays for hyperthermic treatment," M. S. Thesis, Univ. of Illinois at Urbana-Champaign, Urbana, IL, 1984.

[35] M. Pappalardo, "Hybrid linear and matrix acoustic arrays," Ultrasonics, vol. 19, no. 2, pp. 81-86, 1981.

[36] D. C. Grethen, "The design of an ultrasound fixed array controller for use in hyperthermia," M.S. Thesis, Univ. of Illinois at Urbana-Champaign, Urbana, IL, 1984.

[37] S. G. Silverman, "The design of an ultrasound phased array controller for use in hyperthermia," M.S. Thesis, Univ. of Illinois at Urbana-Champaign, Urbana, IL, 1984.

[38] K. R. Holmes, W. Ryan, P. Weinstein, and M. M. Chen, "Development of fixed perfused organs for studies of tissue heat transfer (HT)," Physiologist, vol. 26, no. 4, A-77, 1983.

[39] K. R. Holmes, W. Ryan, and M. M. Chen, "Thermal conductivity and H_2O content in rabbit kidney cortex and medulla," J. Therm. Biol., vol. 8, no. 4, pp. 311-313, 1983.

[40] R. K. Jain and K. Ward-Hartley, "Tumor blood flow - characterization, modifications, and role in hyperthermia," IEEE Trans. Sonics Ultrason., vol. SU-31, no. 5, pp. 504-526, 1984.

[41] J. B. Thompson, "Thermal modelling of biological tissues during microwave hyperthermia," M.S. Thesis, Univ. of Illinois at Urbana-Champaign, Urbana, IL, 1983.

[42] URI Therm-X, Inc., private communication, 1985.

[43] P. J. 't Hoen, "Influence of component errors on the directivity function of pulsed ultrasonographic linear arrays," Ultrasonics, vol. 21, no. 6, pp. 275-279, 1983.

[44] B. Butler, S. B. Palmer, and G. J. Primavesi, "Techniques for the generation of ultrasound for extended periods at high temperatures," Ultrasonics, vol. 17, no. 6, pp. 249-254, 1979.

[45] C. W. Badger, E. C. Burdette, S. P. Leech, and J. F. McCarthy, "Adaptive and interactive control system for hyperthermia treatment," Abstract Fb-11, Rad. Res. Soc. Meeting, 1985.

[46] W. Swindell, "A theoretical study of nonlinear effects with focused ultrasound in tissues: An 'Acoustic Bragg Peak'," Ultr. in Med. and Biol., vol. 11, no. 1, pp. 121-130, 1985.

[47] P. P. Lele, "Cavitation and its effects on organized mammalian tissues," Ultrasound: Its Application in Medicine and Biology, F. J. Fry ed., New York: Elsevier Scientific, 1978.

[48] F. J. Fry, G. Kossoff, R. C. Eggleton, and F. Dunn, "Threshold ultrasonic dosages for structural changes in the mammalian brain," J. Acoust. Soc. Am., vol. 48, pp. 1413-1317, 1970.

[49] S. K. Chan, and L. A. Frizzell, "Ultrasonic thresholds for structural changes in the mammalian liver," Proc. of IEEE Ultrason. Symp., pp. 153-156, 1977.

[50] L. A. Frizzell, C. S. Lee, P. D. Aschenbach, M. J. Borrelli, R. S. Morimoto, and F. Dunn, "Involvement of ultrasonically induced cavitation in the production of hind limb paralysis of the mouse neonate," J. Acoust. Soc. Am., vol. 74, no. 3, pp. 1062-1065, 1983.

VITA

Paul Joseph Benkeser was born in Lafayette, IN, on December 29, 1958. He graduated from Central Catholic High School, Lafayette, IN, in 1977 and then attended Purdue University, West Lafayette, IN. While attending Purdue, he was an undergraduate teaching and research assistant. After graduating from Purdue in 1981 with a B.S. degree in Electrical Engineering, he attended graduate school at the University of Illinois at Urbana-Champaign, Urbana, IL. Under the supervision of Professors Leon A. Frizzell and Charles A. Cain, he obtained his M.S. degree in Electrical Engineering in 1983. Appointments at the University of Illinois included a research assistantship in the Bioacoustics Research Laboratory and a Radiation Oncology Traineeship from the National Institute of Health. Mr. Benkeser is a member of Eta Kappa Nu.